ABSTRACT

Title of Dissertation: CORROSION STUDY IN CRUDE OIL PIPELINES

Najlaa Hassan, Doctor of Philosophy, 2019

Dissertation directed by: Professor Mohamad Al-Sheikhly
Department of Chemical and Biomolecular Engineering

Chemical corrosion contamination of pipelines and other infrastructure are significant and persistent problems in the oil and gas industry. During the crude oil extraction process, which uses water injection to force the oil out of reservoirs, as much as 30% of the liquid content is believed to be water inside the pipeline. This high water content is the principal driving factor in the corrosion of the carbon steel pipelines carrying the oil.

The objective of this work is to identify the corrosion products of the carbon steel pipelines and elucidate the mechanisms and rates of their formation at various temperatures. The observed corrosion rates increase in three distinct modes dominated by the formation of different corrosion products: lepidocrocite below 35 °C, corrosion-inhibiting goethite and hematite between 35 °C and 45 °C, and magnetite at temperatures greater than 45 °C. XPS data show that at 25 °C the concentration of OH^- species appears to be higher than the concentration of O^{2-} species in the corrosion products formed. However, all temperatures above 25 °C showed higher concentrations of O^{2-} species with the highest ratio values at 65 °C ($O^{-2}/OH^- = 1.17$) and 75 °C ($O^{-2}/OH^- = 1.03$). Based on

the electrochemical results, this work demonstrates that the corrosion is anodically controlled (charge-transfer controlled) at 25 ^{o}C-45 ^{o}C, while the cathodic reaction is diffusion controlled. Since both the anodic and cathodic reactions are activation and diffusion controlled, it is concluded that the corrosion process of this system is mixed controlled. This work also shows that as the flow rate of the electrolyte increases, the observed measured activation energy for the overall corrosion processes increases. Finally, while the corrosion rate of carbon steel in a mixture of (70% vol. crude oil /30% vol. seawater) decreases with increasing the temperature, the pitting corrosion increases due to the adsorption of nitrogen and oxygen-containing compounds on the metal surface, and the establishing of localized concentrated Cl^{-} ions, respectively.

CORROSION STUDY IN CRUDE OIL PIPELINES

by

Najlaa Hassan

Dissertation submitted to the Faculty of the Graduate School of the
University of Maryland, College Park, in partial fulfillment
of the requirements for the degree of
Doctor of Philosophy
2019

Advisory Committee:
Professor Mohamad AL-Sheikhly, Chair
Professor Mikhail A. Anisimov
Professor Chunsheng Wang
Associate Professor Jeffery Klauda
Associate Professor Gary Pertmer

Dedication

This thesis is dedicated to my wonderful husband **Hassan Al Shaarawi** for his endless encouragement and love.

And to my lovely daughters **Sarah,** and **Emma** for their love and patience.

Acknowledgements

I would like to express my profound gratitude to my advisor **Professor Mohamad Al- Sheikhly** for his endless supervision, guidance, support, and encouragement. His unique leadership, motivation, insights, and passion for science and engineering were the driving force behind the success of this research work. His guidance and belief in my abilities as a student and researcher illuminated me and allowed me to complete this body of work. I have learned a lot.

Besides my advisor, I would like to thank the rest of my dissertation committee: **Professor Mikhail Anisimov,** for his great encouragement and support. **Professor Chunsheng Wang,** for accepting to serve in my committee with a short time. **Professor Jeffery Klauda,** for all his assistance and guidance during my Ph.D. time. **Professor Gary Pertmer** for his insightful comments and assistance.

I greatly thank **Dr. Paul Rostron** for all his instructions, and constant assistance in the corrosion analysis and electrochemical measurements.

Special thanks to **Dr. Zois Tsinas** for his training and guidance with the use of scanning electron microscopy, Fourier transform infrared spectroscopy, and Raman Spectroscopy. Also, for all long hours providing me with assistance during the work of thesis.

The work performed for this dissertation would not have been financially possible without the assistance of the Petroleum Institute –Abu Dhabi/ UAE with sponsor award ID of 13092531.

I greatly appreciate the support received through the collaborative work undertaken with **Professor Mohammad Modarres**, **Professor Bala Balachandran.**

I would like to thank my dear friend **Dr. Travis Dietz** for all his encouragement, friendship and support during the time of this work. I need to thank all my lab group members: **Matt LeBlanc** for his construction of the flow loop system used for testing the corrosion of carbon steel in seawater with a flow rate similar to the field flow rate. **Azadeh Farzaneh, Kevin Mecadon** for their friendship and stimulating discussions.

Special thanks goes to **Dr. Peter Zavalij**, for his training on the used of X-ray Diffraction, and for his fruitful discussion on the XRD data analysis.

I would to thank **Dr. Karen Gaskell** for preforming the X-ray Photon Spectroscopy measurements and her valuable contribution with data analysis.

I must also thank **Kathleen Gardinier,** Assistant Director in Chemical and Biomolecular Engineering department for her guidance in navigating my way towards my degree.

Big thanks go to **Chuck Marks** and **Aaron Pellman** for allowing me to use their Gamry Potentiostat at Dominion Engineering in order to conduct my electrochemical measurements and for their valued discussion.

I would like to thank my family **Hassan Al Shaarawi**, **Sarah Al Shaarawi** and **Emma Al Shaarawi** for all their tremendous love and support, and for their endless patience during the time of this work.

Table of Contents

List of Tables

List of Figures

List of Abbreviation

NACE	National Association of Corrosion Engineering
MPY	Mils Per Year
i_{corr}	Corrosion Current Density
MIC	Microbial Induced Corrosion
SRB	Sulfur Reducing Bacteria
LPR	Linear Polarization Resistance
OCP	Open Circuit Potential
SEM-EDS	Scanning Electron Microscopy and Energy Dispersive Spectroscopy
XRD	X-Ray Diffraction
FTIR	Fourier Transform Infrared Spectroscopy
XPS	X-Ray Photon Spectroscopy
ASTM	American Society for Testing and Materials
Rpm	Rotation Per Minute
β_a	Anodic Tafel Constant
β_c	Cathodic Tafel Constant

1 Introduction

1.1 Theory of Corrosion

Corrosion is defined as the deterioration of a material because of a reaction with its environment[1]. Corrosion in general can be classified into two types[1]:

Dry corrosion (hot corrosion): The type of corrosion occurs in the absence of liquid or with dry gas. This type is associated with high temperatures (higher than200˚C). Hot corrosion causes damage to the protective oxide on the surface through molten salt contamination such as sodium sulfate (Na_2SO_4), sodium chloride (NaCl), and vanadium oxide (V_2O_5)[2]. This type of corrosion usually occurs in gas turbines, boilers, power generation equipment, internal combustion engines, and industrial waste incinerators[3]. Hot corrosion is initiated when the protective oxide layer on the surface is broken down by erosion corrosion, chemical reactions, and thermal stress[2]. At high temperatures (above 800 ˚C), sodium chloride (an impurity in the air) will react with SO_3 (in the coal and oil fuel) and water vapor to form Na_2SO_4. The high temperature will allow Na_2SO_4 to penetrate through the defects on the protective layer as a corrosive liquid[3].

Wet corrosion: This type of corrosion occurs in the presence of a liquid such as aqueous solution or electrolyte.

The wet corrosion process can be described as a physical analogue of an electrochemical cell. The cell must consist of four major elements:

- The anode electrode: the metal electrode where the anodic reaction takes place.
- The cathode electrode: the metal electrode where the cathodic reaction takes place.
- Electrolyte: the ionic conductor solution in which the anode and cathode are

immersed.

- The power supply: provides the electric potential or current to the cell by creating a conductive path between the anode and cathode.

Wet corrosion consists of two major reactions; anodic (oxidation) reaction and cathodic (reduction) reaction. In the anodic reaction, the metal is dissolved and transferred to the solution as metal ions[4]. The electron that released from the anodic reaction is conducted through the metal to the cathodic site where it will be consumed by the cathodic reaction as illustrated in Figure 1-1. The two reactions occur simultaneously. The metal ions (M^{2+}) will meet with OH^- ions and form metal hydroxides that will deposit on the surface[4].

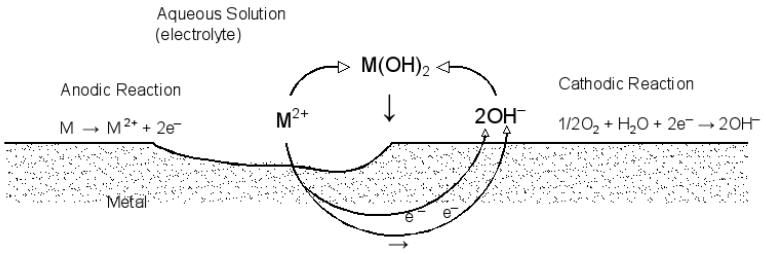

Figure 1-1 Illustration of the wet corrosion of metal (M) in the presence of oxygen[4] (This Figure was taken from "Corrosion and protection" book)

In the case of iron corrosion, the product Fe $(OH)_2$ is not stable. In case of excess oxygen and water, Fe $(OH)_2$ oxidized to trivalent hydrate iron oxide ($Fe_2O_3.nH_2O$)or ferric hydroxide $Fe(OH)_3$, as shown in equations (1-4) below[4]. However, when the oxygen concentration is low, Fe_3O_4 is formed.

$$2Fe \rightarrow 2Fe^{2+} + 4e^{-}$$ (Anodic reaction) **Equation 1-1**

$$O_2 + 2H_2O + 4e^{-} \rightarrow 4OH^{-}$$ (Cathodic reaction) **Equation 1-2**

$$2Fe^{2+} + 4OH^{-} \rightarrow 2Fe(OH)_2 \downarrow$$ **Equation 1-3**

$$2Fe(OH)_2 + H_2O + \frac{1}{2}O_2 \rightarrow 2Fe(OH)_3$$ **Equation 1-4**

This dissertation will focus on the mechanisms of wet corrosion, which is the type of corrosion that occurs in crude oil pipelines.

1.2 Corrosion rate under various conditions

Corrosion rate can be defined as the speed at which any given metal deteriorates in a specific environment[5]. Most of the models that are designed to predict failure of metals are based on the corrosion rate[6,7,8]. Corrosion rate is also used as a scale to compare the resistance of various metal alloys to corrosion [9,10]. The corrosion rate is usually expressed as mils per year (mpy), where a mil is equivalent to one thousandth of an inch. However, many studies report the corrosion rate in terms of milligrams lost per year or millimeters per year[11,12].Other literatures express the corrosion rate in terms of corrosion current ($i_{corr.}$)[13,14].

The corrosion rate is commonly determined under various conditions to evaluate the optimal conditions for creating aggressive corrosive environment. Measuring the corrosion rate at various temperatures, for instance, is used to evaluate the inhibitor efficiency for carbon steel in acidic media, where the corrosion rates were measured in terms of corrosion current at various temperatures and different inhibitor concentrations[15,16,17].Then, the results were compared to calculate the inhibitor efficiency.

1.3 Thermodynamics of Corrosion

Thermodynamics can give better understanding of stability of the chemical species and reactions involved in the corrosion process.

1.3.1 Gibbs free energy

All processes in nature that occur spontaneously must have a negative Gibbs free energy (ΔG) value[18]. The Gibbs free energy is the energy that drives the corrosion process. The free energy in an electrochemical reaction is the maximum of electrical energy that can be achieved I of can be calculated following the Faraday equation as shown below[4,19]:

$$\Delta G = -nFE \qquad \textbf{Equation 1-5}$$

Where n: number of electrons transferred (equiv/mol.); F: Faraday constant (C/equiv); E: the cell potential energy (J/mol.).

Equation 1-5 indicates that the free energy of corrosion depends on the electrochemical cell potential energy.

If (ΔG) < 0 the reaction is spontaneous

If (ΔG) = 0: the reaction is in equilibrium.

If (ΔG) > 0 the reaction is not spontaneous and requires energy added to the system for the reaction to occur.

The Nernst equation can be employed to determine the potential of the system[1].

The cell potential becomes positive when the concentration of oxide species is higher than the reduced species. Under these conditions, corrosion is a spontaneous reaction[1].

$$E = E_{\circ} + 2.3\ \frac{RT}{nF}\ log\ \frac{a_{oxid}}{a_{red}} \qquad \textbf{Equation 1-6}$$

Where E is the cell potential in (V); E_o is the standard potential of the half-cell in (V); R is the ideal gas constant (8.314 J/mol. K); T is temperature in (K); n is the number of moles of electrons transferred; F is the Faraday constant (C/mol.); a_{oxid}, a_{red} are the activities (concentration) of oxidized and reduced species.

1.4 Passivity

Passivity can be defined as the formation of a protective film on a metal surface due to the reaction of the metal with its environment[20]. Under passivity, the metal loses its reaction activity and acts as a noble metal[1]. Some metal alloys can transform from the passive state to active states including some alloys of iron, chromium, nickel, and titanium[1]. To demonstrate the principle of the passivity, the Faraday experiment can be a great example[4]. Faraday put three identical small pieces of iron in three beakers, one is filled with concentrated nitric acid, the second is filled with diluted nitric acid, and the third is the same as the second but with a small amount of physical agitation. The oxidized iron pieces in the first and second beakers act as inert metal and the corrosion rate in both beakers is almost zero. However, in the third beaker, the iron piece is corroded orders of magnitude faster. This experiment indicated that protection of the passivity of a metal is fundamental to the inhibition of corrosion. Temperature, chloride ion concentration and acid concentration affect the metal behavior, where an increase in

one of these factors, could increase the active state of the metal. The mechanisms of growth and break down of the passivity are not fully understood, despite great efforts to elucidate it. However, the mechanism of passivity breakdown has been clarified through many theories. One theory proposed that the breakdown of the passivity is a chemical or electrochemical reaction between the passive film and the aggressive anion absorbed through pores in that film[21]. Another theory explained the break down as a mechanical mechanism, whereas the high electrostriction pressure in oxide film induces stress, which leads to a breakdown of the oxide film[22].

Inside crude oil pipelines, the high flow rate of the crude oil removes the corrosion layers form the carbon steel surface. Some studies have proposed the mechanism of removing the protective layers inside the crude oil pipelines [23]. Nešić claimed that when the shear stress is greater than the bonding force between the protective layers and the metal surface, the protective layers will be removed easily[13].

1.5 Electrochemical Nature of the corrosion

Corrosion is an electrochemical process where the ionic interactions lead to metal dissolution[24]. The oxidation reaction occurs at the anode electrode, while the reduction reaction occurs at the cathode electrode. In general case:

$$O + ne \underset{k_b}{\overset{k_f}{\rightleftarrows}} R \qquad \textbf{Equation 1-7}$$

The forward reaction (reduction) rate is[19]:

$$r_f = k_f C_o(0,t) = i_c/nF \qquad \textbf{Equation 1-8}$$

The backward reaction (oxidation) rate is [19]:

$$r_b = k_b C_R(0,t) = i_a/nF \qquad \textbf{Equation 1-9}$$

Where k_f is the forward rate constant, k_b is the backward rate constant, i_c cathodic current, i_a, i_c are the anodic current and the cathodic current respectively, C_o,C_R are the concentration of O and R respectively. The net corrosion rate is[19]:

$$r_{net} = r_f - r_b = \frac{i}{nF} = k_f C_o(0,t) - k_b C_R(0,t) = \frac{i_a}{nF} - i_c/nF \qquad \textbf{Equation 1-10}$$

Re-arrange Equation 1-10

$$i = i_c - i_a = nF[k_f C_o(0,t) - k_b C_R(0,t)] \qquad \textbf{Equation 1-11}$$

The current density is exchange current (i) over the area. The exchange current is the rate of oxidation or reduction on the equilibrium (i_o)[25]. It should be mentioned that k_f and k_b depend on the electrode's potential. For example, the copper dissolved in the range of (-1.3 V and -1.5 V) but it is stable at outside this range[19,26].

In the case of iron corrosion, the anodic current reaction (i_a) is:

$$Fe \rightarrow Fe^{+2} + 2e \qquad \textbf{Equation 1-12}$$

While the current of the reversible reaction is the cathodic current (i_c):

$$Fe^{+2} + 2e \rightarrow Fe \qquad \textbf{Equation 1-13}$$

At equilibrium, no net current, which means the sum of the two currents is zero:

$$I_a + I_c = 0 \qquad \textbf{Equation 1-14}$$

$$I_a = -I_c = I_o \qquad \textbf{Equation 1-15}$$

The exchange current can be measured experimentally. The exchange current is a function of electrode composition, surface roughness, and soluble species concentration and surface impurities[25].

1.5.1 The effect of the potential on the activation energy

Sodium dissolution in acetonitrile or dimethyIformamide will be used to illustrate the effect of the potential on the activation energy[19].

$$Na^{+} + e \overset{Hg}{\Leftrightarrow} Na(Hg) \qquad \textbf{Equation 1-16}$$

The activation energy profile verses the distance of the sodium nucleus form the interface (reaction coordinate) at equilibrium is shown in Figure 1-2. The activation energy has a certain value at potential corresponding to the equilibrium[19].

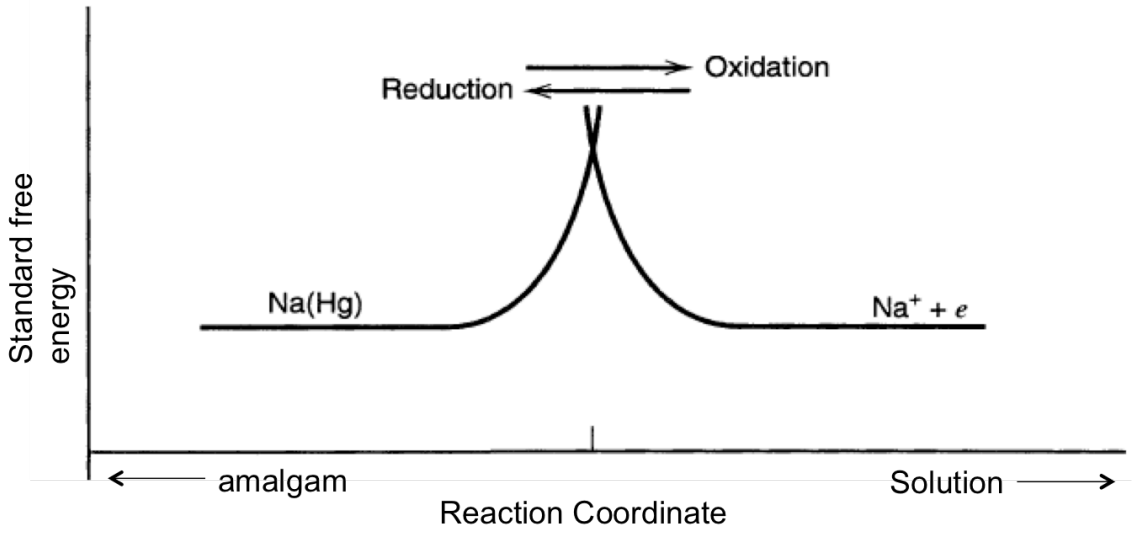

Figure 1-2 The activation energy at a potential corresponding to the equilibrium [19] (The Figure was copied from the "Electrochemical methods: fundamentals and applications" book)

If the potential shifts to a more positive potential, the potential of the produced ions is lowered and the activation energy will decrease in magnitude as shown in

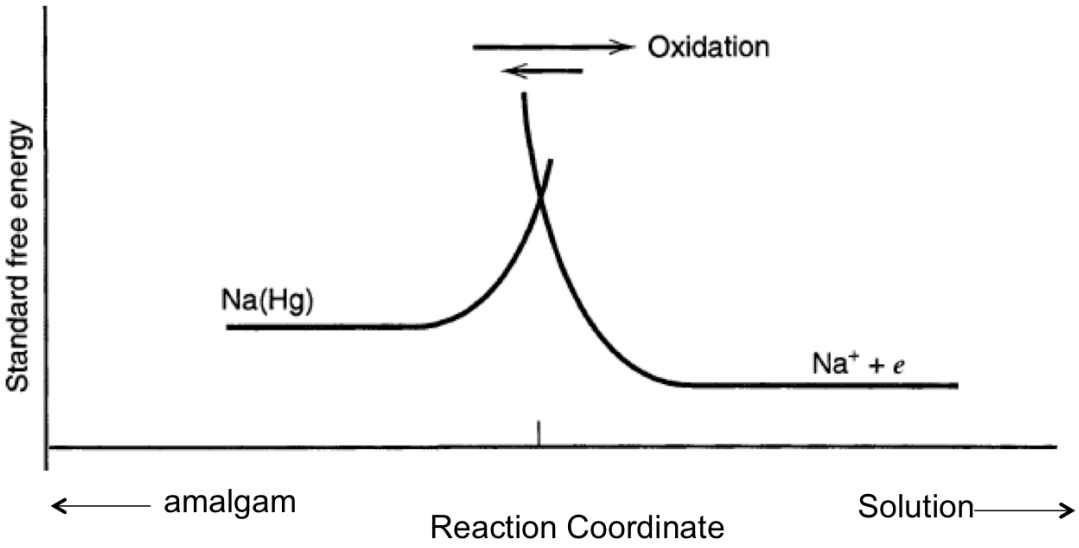

Figure 1-3. Consequently, the reaction will move to the right.

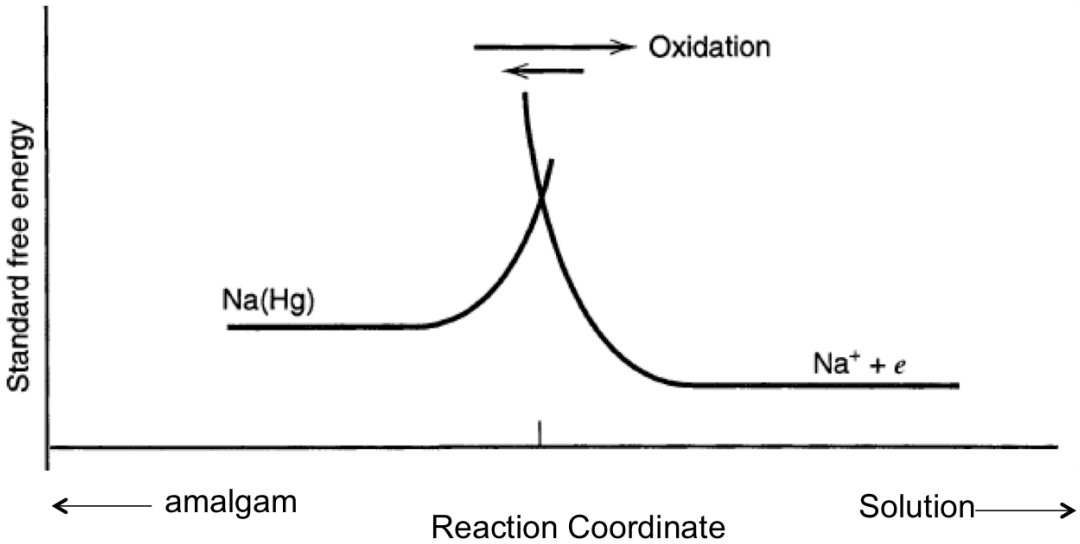

Figure 1-3 The activation energy at a more positive potential than equilibrium (The Figure was copied from the "Electrochemical methods: fundamentals and applications" book)

However, when the potential is shifted more negatively than the equilibrium potential, then the activation energy increases and the reaction is driven to the left as shown in Figure 1-4[19]

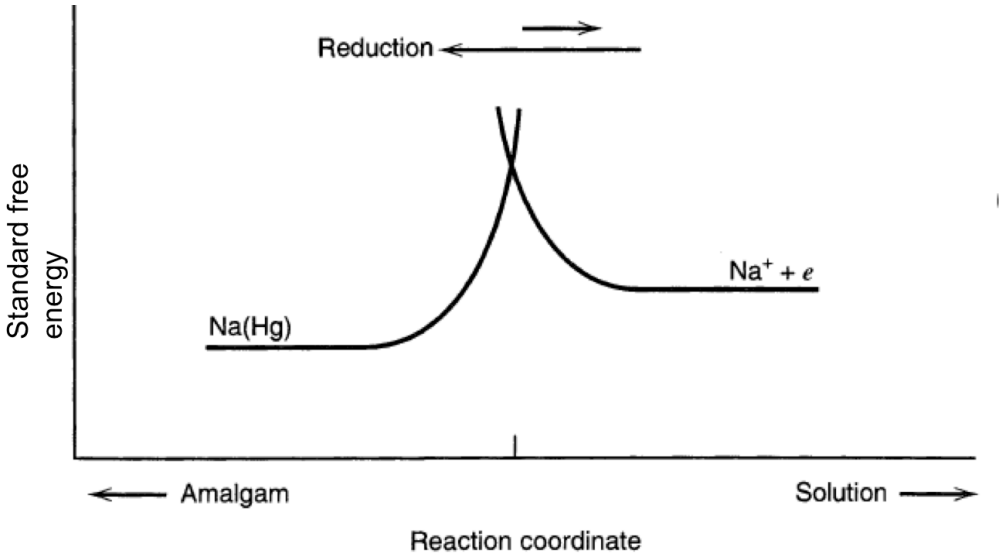

Figure 1-4 The activation energy at a more negative potential than equilibrium

1.6 Polarization in corrosion process

As was mentioned above, at equilibrium, the potentials for the anodic and the cathodic reactions are equal in what is called the equilibrium potential. However, when this potential is shifted from equilibrium, this shift is called polarization. The polarization is measured in terms of overpotential (η), which is a measurement of polarization with respect to the equilibrium potential according to Equation 1-17:

$$\eta = E - E_{eq.}$$ **Equation 1-17**

There are various types of polarizations occurring independently or simultaneously when the metal interact with its environments[1,4]:

1.6.1 Activation polarization

The activation polarization refers to the situation in which the reaction is controlled by the electron-transfer step (the slowest step in the reaction sequence)[1]. At the anode, the metal has to go through a sequence of reaction steps at the metal-solution interface before dissolving in the electrolyte[24].These reaction steps are[24]:

$$M_{lattice} \rightarrow M^{n+}_{surface} \rightarrow M^{n+}_{solution}$$

One of these reaction steps controls the charge transfer for activation polarization[24]. In the case of iron, the reaction steps are[24]:

$$Fe \rightarrow Fe^{+} \rightarrow Fe^{2+} \rightarrow Fe^{3+}$$

The overpotential of the activation polarization and current density relationship follows the Tafel equation as shown below[1]:

$$\eta_a = \pm \beta \, log \frac{i}{i_o}$$ **Equation 1-18**

Where β is the Tafel constant, i is the current density of the oxidation or reduction, and i_o is the exchange current density[1].

1.6.2 Concentration polarization

Concentration polarization occurs when the concentration of the reactants at the surface is low, or an accumulation of the products occurs in the electrolyte [24]. In the concentration polarization, the mass transport is the limiting step in the electrochemical reaction and the reaction under diffusion control[4]. In the case of the oxygen reduction, the concentration of O_2 will be partially constant at a certain distance from the electrode due to the convention[4] as shown in Figure 1-5[4]. Nevertheless, the transport of O_2 will be controlled by diffusion with short distance from the electrode, where the high reduction rate occurs[4]. The diffusion of O_2 follows Fick's law:

$$\frac{dn}{dt} = -D\frac{dc}{dx} \qquad \textbf{Equation 1-19}$$

Where dn/dt is mass transport in the x-direction in mol cm^{-2} s^{-1}, c is the concentration in mol cm^{-3}, D is the diffusion coefficient in cm^2 s^{-1}.

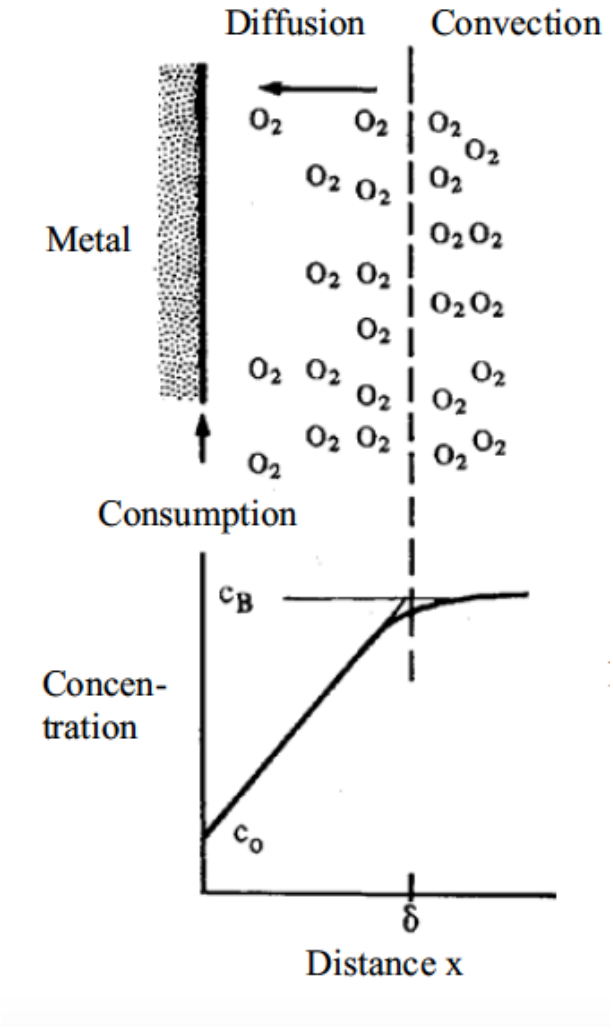

Figure 1-5 Oxygen concentration as function of distance from the surface[4] (copied from the "Corrosion and protection " book)

If the reduction rate increases further, the limiting diffusion rate is reached. The current density of the limiting diffusion (i_L) can be expressed in the equation below:

$$\dot{i}_L = \frac{DnFC_B}{x} \qquad \textbf{Equation 1-20}$$

Where C_B is the bulk concentration, n is the number of electrons F is the Faraday constant; x is the diffusion layer thickness.

The overvoltage due to the concentration polarization can be expressed by the Nernst equation as shown below[4]:

$$\eta_{conc} = \frac{2.3\,RT}{nF}\log\left[1 - \frac{i}{i_L}\right] \qquad \text{Equation 1-21}$$

1.6.3 Combined activation and concentration polarization (mixed)

Activation polarization commonly occurs at the anode electrode[4]. Inversely, the combined activation and the concentration polarization can both occur at the cathode electrode[4]. In this case the overpotential at the electrode will be the summation of two polarizations as follow[1,4]:

$$\eta_c = -b_c \log\frac{i}{i_*} + 2.3\frac{RT}{nF}\log\left[1 - \frac{i}{i_L}\right] \qquad \text{Equation 1-22}$$

Where b_c is the Tafel constant for the cathodic reaction.

At high reaction rates, the concentration polarization controls, while at low reaction rates the activation polarization controls[1].

1.6.4 Polarization resistance

The other form of polarization in the electrochemical cell is the polarization resistance or also is known as ohmic resistance. This polarization is a result of ionic resistance in the solution (electrolyte)[4]. The overpotential can be expressed as below:

$$\eta = IR \qquad \text{Equation 1-23}$$

Where R is the resistance in (Ω), I is the current.

1.7 Fundamental of corrosion kinetics

As mentioned above, corrosion consists form two reaction, anodic (oxidation) and cathodic (reduction). The difference in the surface potential helps the current to pass easily form the cathode to anode. Since, these reactions occur on two close-separated areas on the metal, the potential will be very small[27]. The kinetics of an electrochemical reaction depends upon the potential on the metal surface[19]. For example, hydrogen evolution can occur rapidly at some potential but not at others. Also, copper will dissolve in a clearly defined potential rage, but at other potentials it is stable[19]. All electrochemical phenomena exhibit this effect.

It is therefore fundamental to understanding the corrosion behavior of an oil pipeline system that the effects of potential are correlated to the kinetics of the reactions associated with this system.

1.7.1 Effect of potential on activation energy

For any electrochemical reaction at equilibrium, there will be a k_f, the forward reaction constant, and k_b, the backward reaction constant. At equilibrium, $k_f = k_b$

$$Ox + ne^- \rightleftharpoons_{kb}^{kf} R \qquad \textbf{Equation 1-24}$$

The rate constant can be deduced from statistical mechanics, the Arrhenius equation:

$$k = A\, e^{\frac{-\Delta E}{RT}} \qquad \textbf{Equation 1-25}$$

Thus, the rate constant is dependent upon many factors. The one we shall discuss here is ΔE, the Activation energy.

As the potential changes, the size of the energy barrier will also change. When the system is at equilibrium there will be specific activation energy. If we consider the reaction below as an example:

$$Na^+ + e^- \overset{Hg}{\longleftrightarrow} Na(Hg) \qquad \textbf{Equation 1-26}$$

If the potential shifts to a more positive potential, the potential of the produced ions is lowered and ΔE will decrease in magnitude (reaction is driven to the right) as per le Chatelier's principle.

If the potential is shifted more negatively than the equilibrium potential, then ΔE increases and the reaction is driven to the right.

Additionally, the position of ΔG^* maximum along the reaction coordinate will change as the applied voltage changes. This positional change also affects the magnitude of ΔG^*

1.8 Corrosion types based on the appearance

There are many types of corrosion depending on the appearance of the corrosion:

1.8.1 Pitting corrosion:

Figure 1-6 Pitting corrosion in pipelines [A]

Pitting corrosion is defined as a localized form of corrosion that looks like cavities or holes on the material surface[1]. These pits usually form close to each other creating an uneven surface. It should be mentioned that pitting corrosion is highly destructive since it is very difficult to detect these pits at the beginning of their formation. Since pits are small and mostly covered with corrosion products, it is difficult to predict[1]. Pitting corrosion could be very dangerous. As an example of the devastating effects of the pitting corrosion, in 1992, a single site of pitting corrosion in a pipeline carrying gasoline over a sewer line led to the death of 215 people in Guadalajara Mexcio[28].

Pitting corrosion progresses through three stages; initiation of the pit, prorogation of a pit (autocatalytic nature) and pitting termination (where the leakage happens)[4]. The initiation stage may proceed over the course of months or years before a visible pit appears on the surface. If we consider a piece of metal exposed to seawater with

dissolved oxygen, the metal will have a uniform attack and the cathodic and anodic reactions will occur as soon as the exposure to the seawater occurs[1].

$O_2 + 2H_2O + 4e^- \Rightarrow 4OH^-$ (cathodic reaction)
$M \Rightarrow M^{2+} + 2e^-$ (anodic reaction)

Since the metal has a different energy distribution on its surface, the corrosion rate will be higher in one area than another area, and there will be a region with extra dissolution that leads to the initiation of a pit in the direction of gravity. The second stage is an autocatalytic process, which means the corrosion process within a pit creates conditions to promote the continued dissolution of metal within the pit. Figure 1-7 formation of metal ions is shown, the electrons are shown conducting along the surface of the metal, and the reduction of oxygen occurs at the adjacent surface of the pit[1]. Inside the pit, a rapid metal dissolution is occurred. Thus, the area with high oxygen concentration (the outer surface of the pit) will act as a cathode and the area with low oxygen concentration (the pit) will act as an anode. Inside the pit, the concentration of positive metal ion is high because of the rapid dissolution. In order to maintain electroneutrality inside the pit, the chloride ions will migrate to the pit. Consequently, a high concentration of MCl will form inside the pit as a product of hydrolysis. MCl will hydrolyze and will produce hydrogen and chloride ions that decrease the pH inside the pit. The whole process continues to accelerate over time, resulting in an increase in the rate of metal dissolution. Eventually, the pit will penetrate the metal and the system will fail[1].

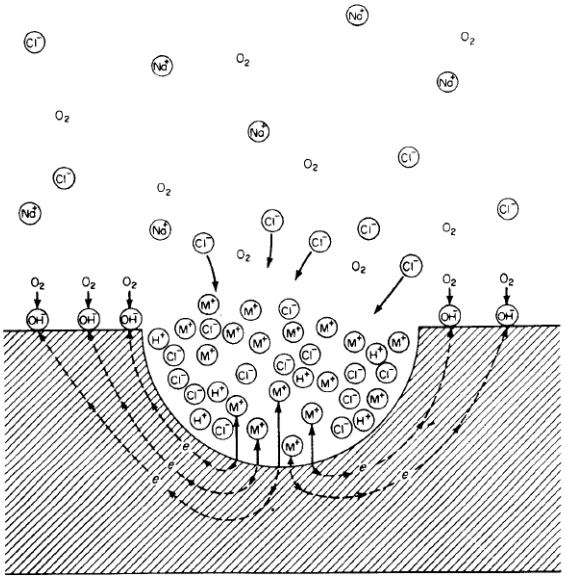

Figure 1-7 The second stage of pit formation autocatalytic nature[1] (Figure was copied from "Corrosion Engineering- Fontana, Mars" book)

Cracks and pits occur on the surface of the metal, which is exposed to an environment with high concentration of aggressive ions such as chloride[4]. Pitting is a serious problem since the pits are difficult to predict. Pit formation consists of two stages; initiation and propagation[1]. Several theories about the initiation of the corrosion pits have been proposed. One theory stated that the local acidity from the metal ion hydrolysis can break the passivity and initiate pits on the metal surface[29]. Another theory suggests that large amounts of chloride ions are adsorbed on the iron oxide film around the lattice, and form a high-energy transitional complex. This complex immediately separates from the oxide ion and dissolved into the solution. The stronger anodic field on the thin film will transfer another cation to the surface, where it will meet the chloride ion and complex with them, then enter the solution. This can lead to "auto-accelerated " breakdown[21]. Macdonald and his team proposed a point defect model to explain the pits initiation. In their model, they assumed that the build-up of the metal holes at the film/metal interface

caused by the high diffusion of metal cation from the metal/film to film/solution interface[30]. In addition, many studies endorse the theories above[21,22,30,31]. Pits, voids, and cracks present on the surface exposed to seawater with high chloride concentration [32,33]. W. Liu observed cracks in carbon steel surface that were immersed for 960 hours in seawater[34]. Also, cracks were observed on the surface of carbon steel in atmospheric corrosion with high chloride ion environment.

1.8.2 Crevice corrosion

When a metal with crevices and holes on its surface is exposed to a corrosive solution or environment, crevice corrosion will occur[1]. This type of corrosion usually happens beneath nail or screw heads, flange gaskets, surface deposits or under bolts.

Figure 1-8 Crevice corrosion in the pipelines[B]

To explain the crevice corrosion mechanism, we will consider metal exposed to a corrosive solution, such natural water with NaCl as an example. There are four stages of mechanism for the crevice corrosion:

1. Depletion of oxygen in crevice due to consumption in the crevice region:

The cathodic and anodic reaction will take place at this stage in crevice region and the rest of the metal as in the reactions below[1]:

$$\mathbf{M \rightarrow M^{+} + e^{-}} \qquad \textbf{Equation 1-27} \qquad \text{Anodic reaction}$$

$$\mathbf{O_2 + 2H_2O + e^{-} \rightarrow 4OH^{-}} \qquad \textbf{Equation 1-28} \qquad \text{Cathodic reaction}$$

The oxygen in the crevice region decreases because the stagnant nature of the area around the region and the excess of metal ion concentration [M^{+}]. Consequently, the crevice area acts as anode and the rest of the metal acts as cathode as shown in Figure 1-9, top[4].

2. Increase of the acidity in the crevice because of the hydrolysis:

When the oxygen has been depleted, there will be no OH^{-} formation in the crevice. In stage one, the small anode area and large cathode area have been formed, which consequently leads to an increase in the size of the crevice and the corroded areas. Cl^{-} migration will maintain the charge equilibrium, which will lead to an increase in the production of metal chloride $M^{+}Cl^{-}$which undergoes hydrolysis. Metal hydroxide will decrease the pH level of the neutral water from 7 to 2 or 3, and hydrochloric acid will form in the crevice. The corrosion will be aggressive at this stage.

3. Increase of acidity in the crevice due to hydrolysis

When the oxygen has been depleted, there will be no OH^{-} formation in the crevice. In stage one, small anode area and large cathode area has been formed, which made the increase the production of metal ion and the crevice area will be more corroded. Thus, the crevice will be electropositive energy. Cl^{-} migration will maintain the charge equilibrium, and that will lead to increase production of metal chloride $M^{+}Cl^{-}$which hydrolysis. Metal hydroxide will decrease the pH level of the neutral water from 7 to 2 or 3, and

hydrochloric acid will form in the crevice. The corrosion will be aggressive at this stage as shown in Figure 1-9, the bottom[4].

$$M^+ + H_2O \rightarrow MOH \downarrow + H^+ \quad \text{Equation 1-29}$$

$$Cl^- + M^+ \rightarrow M^+Cl^- \quad \text{Equation 1-30}$$

$$M^+Cl^- + H_2O \rightarrow MOH + H^+Cl^- \quad \text{Equation 1-31}$$

4. Passive layer breakdown

When pH is low, the corrosion rate will increase because the crevice is transferred to the active zone[1].

5. Perforation-leakage

The propagation phase and the acidity will lead to a large corrosion current that will concentrate in a small area on the surface. Eventually, the system will leak or fail[4].

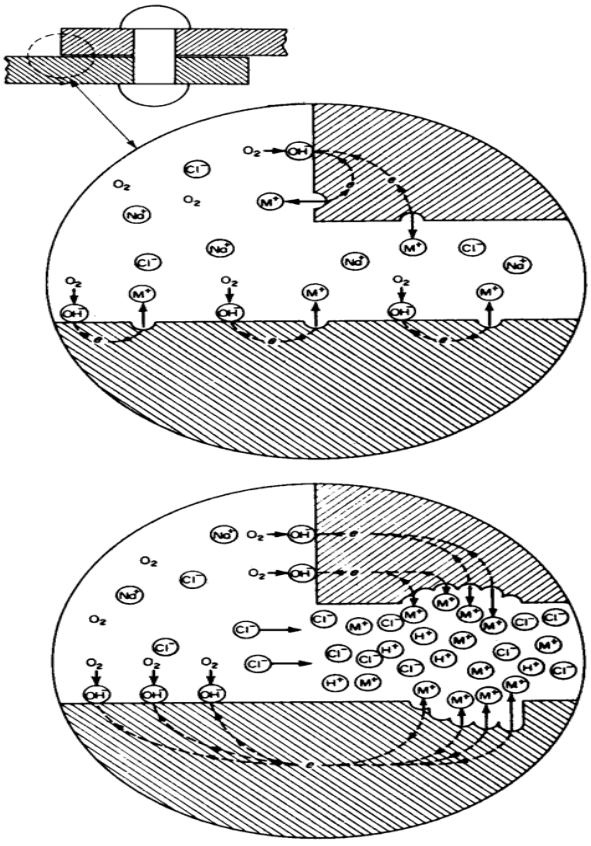

Figure 1-9 Crevice corrosion: the above (initial), the bottom (later stage)[4] Figure was copied from "Corrosion and protection" book)

1.8.3 Uniform corrosion

Figure 1-10 Uniform corrosion inside water pipelines failed after 20 years

Uniform corrosion is normally defined as the electrochemical reaction that proceeds uniformly over an entire exposed surface. The metal will become thinner, and eventually will fail[1]. Uniform corrosion is always occurring in aqueous solutions or on wet surfaces. The mechanism of uniform corrosion is shown in Figure 1-11. As the piece of iron exposed to a droplet of seawater, there will be two areas, one is poorly oxygenated that will act as an anode and the well-oxygenated area that will act as a cathode. At the anode, the iron will oxidize to Fe^{2+} and release two electrons. These electrons will go through the metal and be in contact with water and oxygen forming hydroxide ion through a cathodic reaction. These reactions will occur simultaneously to form corrosion product (rust). The rust will form between the anode and the cathode[1].

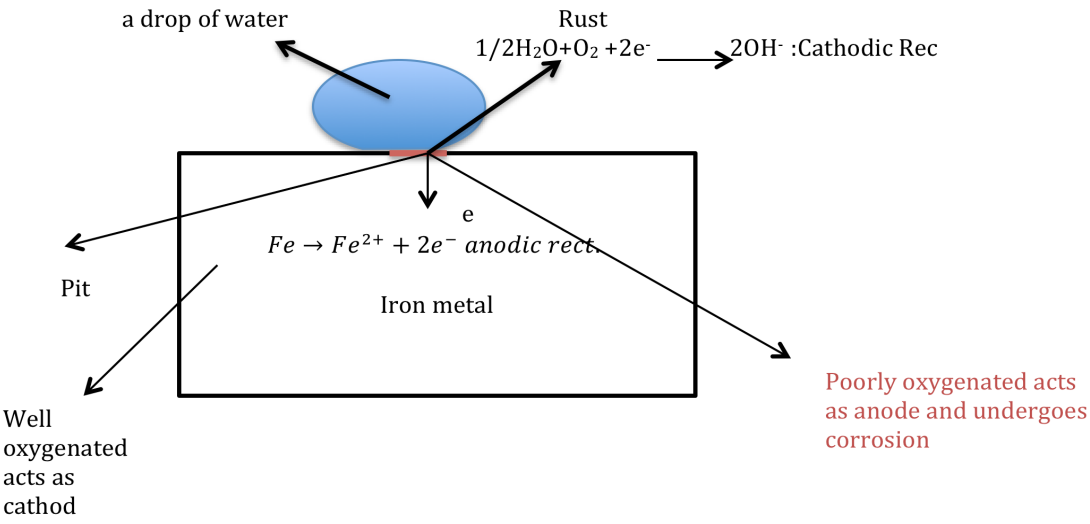

Figure 1-11 The rust formation on the surface of iron expose to water

1.8.4 Microbial induced corrosion (MIC):

Figure 1-12 Microbial induced corrosion on the pipelines metal surface

MIC is an electrochemical process that initiates and accelerates corrosion by microorganisms[35]. This type of corrosion plays a significant role in crude oil pipeline degradation, for example in the US, over 75% of the corrosion in crude oil pipeline is induced by sulfur-reduced bacteria (SRB). Also, 50% of underground pipelines fail because of the metabolic activities of microbes[36]. MIC occurs in many types of pipelines such as

seawater, sewer, and freshwater. Also, it can be found in industries such as crude oil production and marine industries. MIC is very harmful to many materials and it has been addressed as the primary failure cause to underground pipelines. As it was mentioned above, this type of corrosion is caused by bacteria. There are many types of these bacteria such as sulfur-reducing bacteria (SRB), sulfur-oxidizing bacteria, aerobic bacteria, and nonaerobic bacteria. The internal corrosion occurs because the bacteria form an acidic biofilm that traps the electrolytes and acid.

The bacteria move out of the bulk to the metallic surface to live, divide and form a big consortium on the surface known as a biofilm[35]. The biofilm consists of many colonies of microorganisms that adhere to the metal and create a different environment than the surrounding. This environment will produce highly active corrosion area because of the high electrical potential difference between the microorganism area and the surrounding metal. The biofilm formation will create different chemical concentrations of the metal surface due to the passive effect of the biofilm on oxygen and nutrient diffusion to the metal surface[35]. Also, the microbes and extracellular polymeric substances (EPS) in the biofilm will lead to formation of a pH gradient on the metal surface which will in-turn induce crevice and pitting corrosion[37]. The formation of a biofilm goes through five stages, which start immediately after a metal is exposed to an aqueous environment. The first stage of biofilm formation called, "conditioning film," when the electrostatic arrangement of many types of portions and organic components combine with water's chemistry. Then, the bacteria move from the bulk and attached to the surface. At this stage, the bacteria is known as "sessile bacteria," which is different from their state before the attachment which is called "planktonic"[35]. Later, these sessile bacteria start to

cultivate and form more biofilms on the metal surface. At the fourth stage of the biofilm formation, the bacteria start to consume the entire available nutrient in the media to grow. The biofilm at this stage became thick and act as a net to trap the organic nutrients. The oxygen and the pH will be different on the metal surface; this could lead to pitting corrosion on the surface with high biofilm thickness. The stages of biofilm formation are described below[35]:

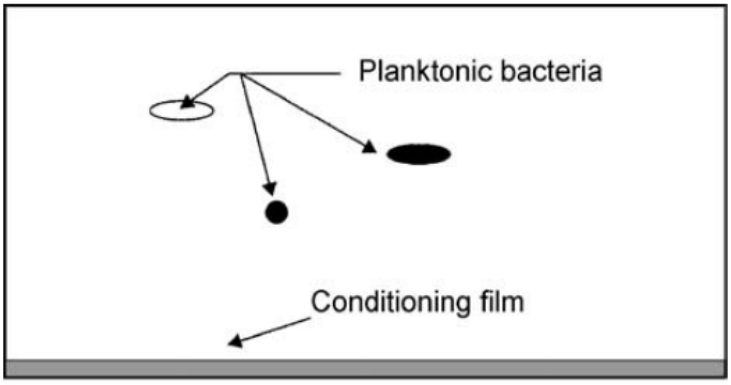

Stage 1: Conditioning film accumulates on submerged surface.

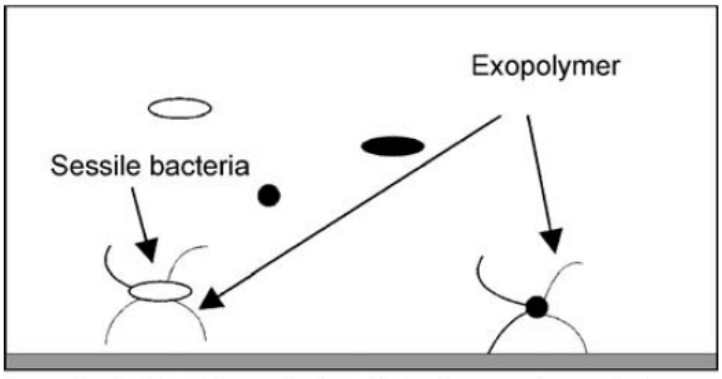

Stage 2: Planktonic bacteria from the bulk water form colonies on the surface and become sessile by excreting exopolysaccharidic substances (EPS) that anchors the cells to the surface.

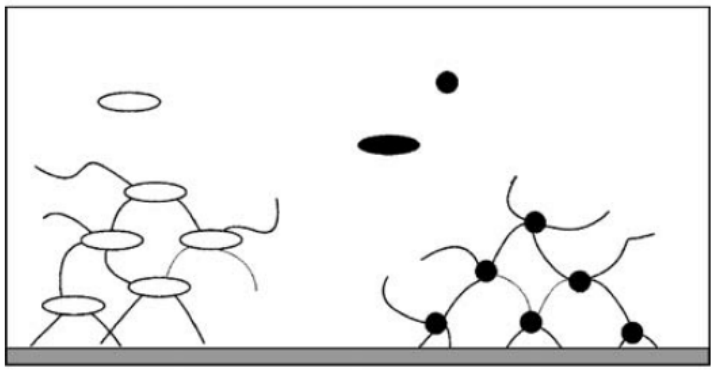

Stage 3: Different species of sessile bacteria replicate on the metal surface.

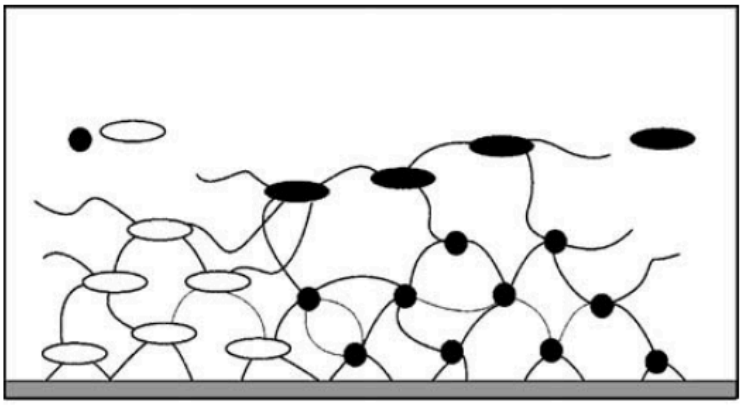

Stage 4: Micro-colonies of different species continue to grow and eventually establish close relationship with each other on the surface. The biofilm increases in thickness and the electrochemical conditions beneath the biofilm begin to vary in comparison with the bulk of the environment.

1.8.5 Erosion corrosion

Erosion corrosion can be defined as an increase in the rate of degradation or attack on metal because of a rapid movement between a corrosive solution and metal surface[1]. The high flow will remove the protective surface film on the metal, which leads to an increase of the corrosion rate. A pit or burr can change the laminar flow, causing turbulence that leads to erosion corrosion. Consequently, a turbulent flow can lead to the

removal of small pieces of metal and their dissolution as ions or solid corrosion products. This causes the metal to thin and eventually fail[1].

Figure 1-13 Erosion corrosion inside pipeline

Erosion corrosion would appear as pits, grooves, and gullies. Erosion corrosion is common in crude oil pipelines, where it can be found in bends, elbows, and tees[1]. This type of corrosion can be found in crude oil pipeline, water pipes, and natural gas pipelines.

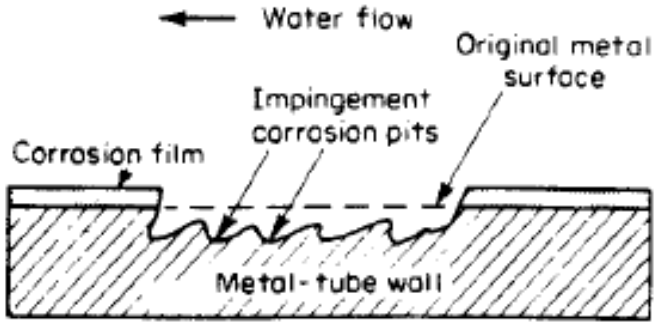

Figure 1-14 Erosion corrosion of condenser tube wall[1] (Figure was copied from "Corrosion Engineering- Fontana, Mars" book)

1.8.6 Stress corrosion

Stress corrosion refers to localized corrosion which produces cracks in a metal because of concurrent tensile stress and localized corrosion[1]. The tensile stress can be initiated by the forces exerted on the metal through changing temperatures or other factors[4]. Stress corrosion can also occur when a metal is exposed to aggressive ions such as chloride, or very corrosive dissolved gas such as CO_2 and H_2S[1,4]. Stress corrosion generally originates at the defect spot in a metal surface such as the segregation zone in grain boundaries or hard spots from the heat treatment[4].

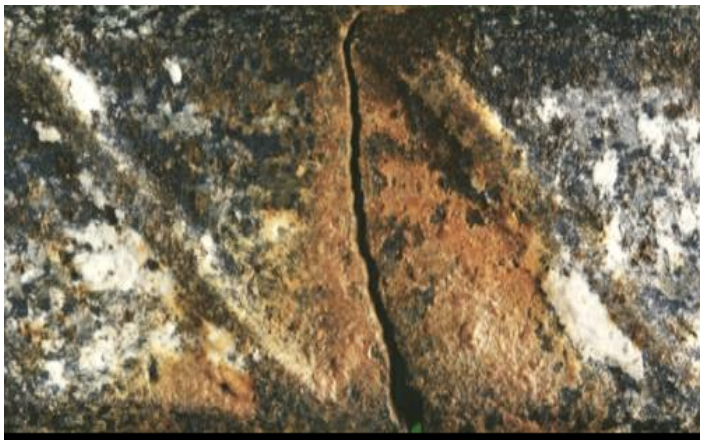

Figure 1-15 Stress corrosion inside a pipeline

1.8.7 Galvanic corrosion

Galvanic corrosion occurs when a noble metal is in contact with non-noble metal in the presence of corrosive or conductive solutions[4]. Corrosion of the noble metal (high

resistance to corrosion) is decreased, while the other metal (less resistance to corrosion) is increased. The noble metal becomes the cathode, whereas the other metal becomes the anode[1]. The driving force in this type of corrosion is the potential between the two metals[1]. The best example for galvanic corrosion is a dry cell battery. In a dry cell battery, the carbon acts as the noble metal and the zinc is the less resistance to corrosion.

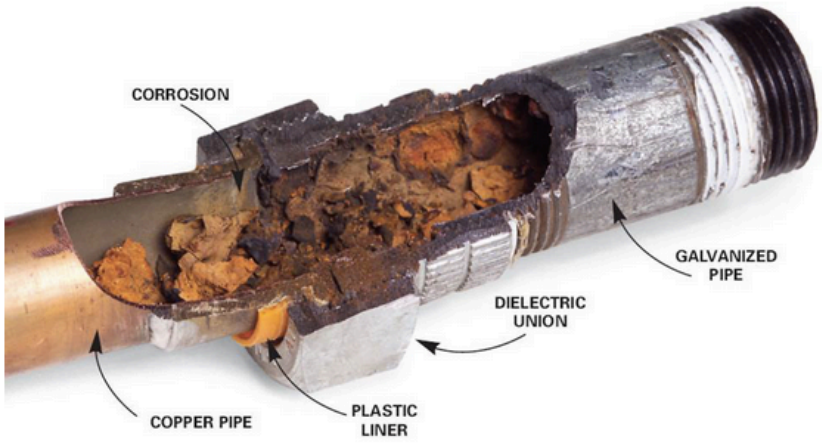

Figure 1-16 Galvanic corrosion inside pipelines

1.9 Corrosion in Different Environments

1.9.1 Atmospheric corrosion

Atmospheric corrosion is a uniform and general corrosion that occurs on a metal surface in the atmospheric environment[4]. Atmospheric corrosion depends on climate factors such as temperature, humidity, and frequency of wet and dry cycles. In addition, the presence of chloride and SO_2 in the atmospheric can accelerate the corrosion of the metal[12]. It has been documented that atmospheric corrosion for most metal occurs in the environment with 50-70% relative humidity[20]. Atmospheric corrosion can be classified according to the surrounding environment, specifically into four types[4]:

i. Urban: polluted environmental with smoke and soot. SO_x and NO_x are can sometimes be considered as contaminants in this environment[25].
ii. Rural: dry environment with little or no pollution. The corrosive agents in this type are oxygen, carbon dioxide, and moisture[25].
iii. Marian: is the area with high humidity and high concentration of chloride. This environment is considered to lead to the most aggressive rates of corrosion.
iv. Industrial: high pollution environment with industrial precipitate such as sulfur dioxide, chlorides, phosphates and nitrates[25].

From the environmental conditions for each type, it is clear that the Marian is the most aggressive atmospheric corrosion. Beside the environmental pollutants, the climate condition plays a significant role in atmospheric corrosion. Rain in atmospheric corrosion plays a dual role, such that it can increase the corrosion rate by increasing the water

concentration on the metal surface as well as carry away the protective corrosion layers. Additionally, the rain can impede the corrosion rate by washing away pollutants.

1.9.2 Fresh water corrosion

Freshwater sources include the water in lakes, rivers, rain, brooks, and groundwater. The dissolved oxygen is the most important factor in the freshwater corrosion[1]. Freshwater contains Ca^{2+} and Mg^{1+} as salts. If these salt concentrations are high, the water is called "hard water", while in the absence of these salts, the water is called "soft water"[4]. Since hard water contains $CaCO_3$ as a precipitate at high concentration of salts, it acts as a barrier to impede the oxygen diffusion through its layers. Consequently, the corrosion rate decreases and eventually will stop because corrosion rate depends on the supply of oxygen[4]. On the other hand, in soft water, the corrosion rate will increase due to lack of the protective layer formation. Corrosion seen in boilers or heat exchangers are examples of freshwater corrosion.

1.9.3 Corrosion in soil

Corrosion in soil commonly occurs on the external surface of metal piping for water, sewage, gas or oil. Soil corrosion depends on the soil aeration, water, pH, soil resistivity to corrosion, the concentration of soluble salts and microbiological activity[4]. The most common corrosion forms in soil corrosion are pitting, galvanic, erosion and MIC. Soil with high concretion of salts, low resistivity to corrosion, and high acidity is the most corrosive soil[38]. It has been identified that MIC is the main cause of the failure of underground pipelines.

1.9.4 Corrosion in concrete

Concrete corrosion has commonly occurred in bridges and buildings in marine areas. Since the tensile strength in the concrete is low, reinforcing the concrete with steel can improve the tensile strength and the toughness of the material[25]. The most common reinforcing steel is the bare carbon steel. Because of the porous nature of concrete, highly alkaline solutions such as NaOH, KOH and $Ca(OH)_2$ with pH 12.6-13.8 are added to the cement mixture[25]. This alkalinity provides high resistance to embedded steel corrosion by forming passive layers[4]. However, the presence of aggressive substances such as chloride, carbon dioxide, and moisture could break this passivation[39]. The most typical mechanism in concrete corrosion is known as "carbonation." Where carbon dioxide from the air reacts with $Ca(OH)_2$ in cement mixture as in the equation below[25]:

$$\mathbf{CO_2 + Ca(OH)_2 \rightarrow CaCO_3 + H_2O} \qquad \textbf{Equation 1-32}$$

As results, the pH will be reduced to 8 in some areas of the concrete. Consequently, the passive film will break and corrosion will initiate[25].

1.9.5 Corrosion in seawater

Seawater has been associated extensively with applications such as cooling, ships, power plants and crude oil injection. Although seawater has a pH of 8.1-8.3, it is still considered one of the most aggressive corrosion environments. This is due to the high concentration of chloride ions in this environment. There are many additional factors affecting the corrosion rates in seawater such as oxygen, flow rate, temperature and

biological organisms[1]. During seawater corrosion, the corrosion layers will accumulate on metals surfaces. These layers will act as an inhibitor by impeding oxygen diffusion. In splash zones, where the velocities of seawater against metal surfaces are high compared with other zones, the corrosion layers on the surface of the metal is thin, which allows oxygen to diffuse easily into the metal. Consequently, the corrosion rate of the metal in the splash zones is higher than in other zones[4].

1.10 Carbon steel

Carbon steels are used as the preferred metal alloy for both offshore and onshore crude oil piping systems due to their low cost and availability compared to other corrosion resistant alloys[40]. However, carbon steel has one of the highest rates of corrosion relative to other alloys. The main components of carbon steel are iron and up to 2 wt. % carbon, among other elements such as manganese, copper, and phosphorous. Comparably, stainless steel has a high resistance to corrosion due to the high concatenation of chromium up to 11%. Chromium reacts with oxygen to form chromium oxide which acts as an inhibitor to corrosion[41,42]. Therefore, stainless steel is used only for potable water pipelines and food pipelines. In oil and gas pipelines, the cost of using stainless steel in pipelines can be economically prohibitive. Many studies have discussed the corrosion of carbon steel in crude oil, however, the corrosion of crude oil in the presence of seawater is still poorly understood due to the limited amount of experimental data and research[40,43–46].

2 Corrosion in crude oil pipelines

The main objective of this study is to elucidate the mechanism of corrosion inside crude oil pipelines. Pipelines play a significant role in the oil industry because of their significance in the transportation of oil and natural gas from the wells to the refineries and treatment plants across thousands of miles. Thus, pipeline safety is important to ensure a safe operating environment and continuous oil production. For many decades, corrosion has been the most significant cause of failure in crude oil pipelines[47]. Therefore, great efforts have been made to understand the mechanisms of corrosion in crude oil pipelines. Crude oil pipeline corrosion is a complicated process. Internal corrosion can be influenced by the presence of CO_2, H_2S, and water inside the pipeline. Additionally, the impact of the conditions of operation in the pipeline such as ambient temperature and flow rate can change the corrosion rate significantly.

There are many studies on the corrosion of the carbon steel caused by the presence of CO_2, H_2S, and microbes. However, the literature lacks studies on the effect presence of the seawater in the crude oil. In crude oil pipeline corrosion studies, the investigations have concentrated on the effect of CO_2 on the corrosion of crude oil pipelines[13,48,49,50]. Other studies investigated the operational conditions such as temperature, velocity and the time. Peng and Zhang studied the effect of temperature, CO_2, velocity and time on the corrosion rate of carbon steel in the produced water from subsea pipelines[11]. In their study, the corrosion rate increased with increasing P_{CO2}, velocity and exposure time. However, the corrosion rate increases with increasing temperature until 65˚C and starts decreasing at higher temperatures[11]. Although this study

shows the effects of operational conditions on the corrosion rate of carbon steel in crude oil pipelines, it did not provide a clear explanation of the results.

In order to control the corrosion in pipelines, it is important to understand the underlying corrosion mechanisms. In crude oil pipelines, there are two types of corrosion:

2.1 External corrosion:

External corrosion is an aggressive type of corrosion that is the cause of 40% of the accidents in pipelines during the period (2013-2017), 8 % of these incidents occurred in crude oil pipelines[51]. External corrosion occurs when the external surface of the pipelines reacts with the surrounding corrosive environment. External corrosion in pipelines is generally controlled through a combination of coatings and cathodic protection (CP) that work as a barrier between the pipeline surface and the corrosive environment. External corrosion can form from the MIC, galvanic action and erosion corrosion.

2.2 Internal corrosion

There are many factors that can impact the internal corrosion rate such as acidic gases (CO_2, H_2S), water chemistry, temperature, flow velocity, the chemical compositions of the metal, and microorganisms. Figure 2-1 shows the parameters that affect the internal corrosion of crude oil pipelines. According to the Alberta Energy Regulator report, internal corrosion is responsible for over 50% of the crude oil pipelines failure[52]. There are several different mechanisms by which pipeline failure by corrosion can occur; sour corrosion, sweet corrosion, microbial corrosion and water corrosion. When designing a system, it is often the case that the corrosion is assumed to be uniform. This assumption means that the penetration rate can be calculated; therefore a corrosion

allowance would give the pipeline lifetime required for the operation. Unfortunately, most corrosion tends to be highly localized, leading to pinpoint penetration rather than uniform thinning. This assumption of uniform corrosion rates leads to two equally disastrous results: either the pipeline fails prematurely due to pinpoint leakage, or a perfectly preserved pipeline is dug up and replaced. To understand the corrosion in pipelines, we need to identify the mechanism of corrosion and how to mitigate it accurately.

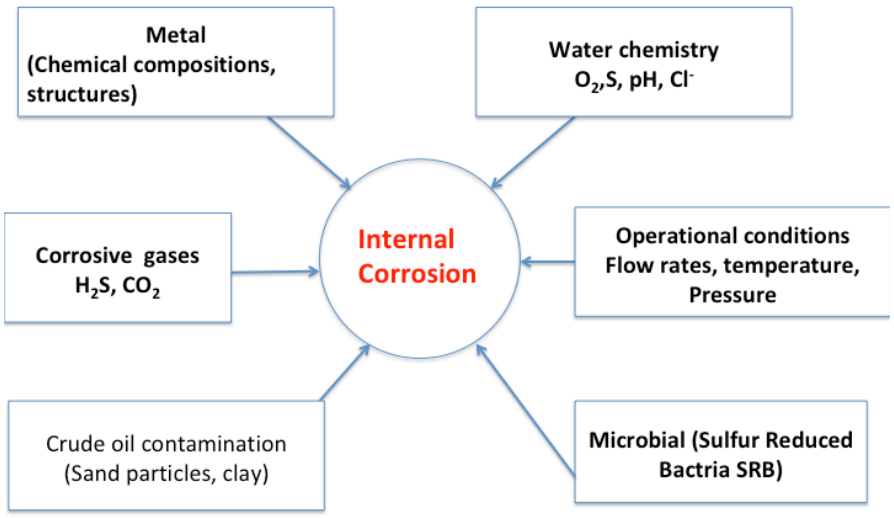

Figure 2-1 The parameters that influence the internal corrosion in crude oil pipelines

2.3 Sweet Corrosion

Carbon dioxide is present in crude oil pipelines as a co-product or is injected to enhance oil recovery[53]. CO_2 corrosion or "sweet corrosion" is one of the major sources of corrosion in the crude oil industry. CO_2 corrosion has been studied extensively[45,48,49,54]. The mechanism of CO_2 corrosion is well documented and is already incorporated in prediction models[55,56]**.** In a piping system, CO_2 is present in the gas phase. Dry CO_2 is not corrosive; however, dissolved CO_2 in an aqueous solution has a significant effect on promoting the electrochemical reaction between the carbon steel and the contacting aqueous solution[48]. Dissolved CO_2 in the water forms a weak acid (carbonic acid) through the following chemical reactions, which provides another source of H^+ to the normally cathodic reaction as shown in Equation 2-1[48]. In general acidic corrosion, the reduction of H^+ (cathodic reaction) dominates. However, in sweet corrosion, an additional cathodic reaction occurs based on the reduction of H_2CO_3 which ultimately increases the corrosion rate[1,57,47].

$$\mathbf{CO_2 + H_2O \leftrightarrow H_2CO_3} \qquad \textbf{Equation 2-1}$$

$$\mathbf{H_2CO_3 \rightarrow H^+ + HCO_3^-} \qquad \textbf{Equation 2-2}$$

$$\mathbf{HCO_3^- \leftrightarrow H^+ + CO_3^-} \qquad \textbf{Equation 2-3}$$

The anodic reaction of carbon steel in case of CO_2 corrosion shown in Equation 2-4:

$$\mathbf{Fe \rightarrow Fe^{2+} + 2e^-} \qquad \textbf{Equation 2-4}$$

The total reaction as in equation below:

$$\mathbf{Fe + H_2CO_3 \rightarrow FeCO_3 + H_2} \qquad \textbf{Equation 2-5}$$

2.4 Sour Corrosion

Hydrogen sulfide (H_2S) is found in gas and oil production as a result of mineral dissolution or as a by-product of petroleum forming process[25]. It is very well known that H_2S is very corrosive to carbon steel. The H_2S corrosion (sour corrosion) mechanism still is not well defined despite a significant amount of effort[58–60]. During the electrochemical reactions that occur during corrosion, H_2S is usually generated by SRB and ultimately converted to SO_4^{2-}. H_2S can play a dual role in corrosion by increasing or decreasing the corrosion rate of the metal depending on the process conditions. When the H_2S concentration is low, the pH is between 3- and 5, and the pipeline experiences a long immersion time, H_2S can form a protective layer of FeS that works as a corrosion inhibitor[61]. On the other hand, at high concentration of H_2S, it has been reported that the sour corrosion induces pinholes in crude oil pipelines[62]. This study demonstrates the presence of pinholes that are composed of significant amounts of greigite (Fe_3S_4) and mackinawite (FeS)[62]. There is a large body of literature on SRB-induced fatigue and cracking in pipelines[62–65]. Specifically, Vosikovsky observed that the crack growth was enhanced by increasing the concentration of H_2S in the crude oil[58]. Similar to CO_2 corrosion, H_2S is dissolved in water and forms a weak acid as in equation below:

$$\mathbf{H_2S\,(g) \rightarrow\ H_2S(aq) \rightarrow H^+ + HS^-(aq)} \qquad \textbf{Equation 2-6}$$

$$\mathbf{HS^-(aq) \leftrightarrow H^+(aq) + S^{2-}(aq)} \qquad \textbf{Equation 2-7}$$

The cathodic reaction in H_2S corrosion as follows:

$$2H_2S \rightarrow 2H + 2HS^- \quad \text{Equation 2-8}$$

$$Fe^{2+} + S^{2-} \rightarrow FeS \quad \text{Equation 2-9}$$

2.5 Selected studies on the crude oil corrosion

There are a very limited amount of studies discussing the effect of the seawater on crude oil pipelines. A unique study by Efird et al. showed that the percentage of brine in crude oil has mixed results on the corrosion rate of stainless steel depending on the type of oil[66]. In his study, Efird et al. measured the corrosion rate of stainless steel immersed in crude oil and brine mixture at 85˚C. The results showed the corrosion rates under same conditions and brine percentage vary based on the type of crude oil[66].
On the other hand, crude oil acts as corrosion inhibitor. A detailed study by Ayello et al. shed the light on the group of chemicals in crude oil that produce the observed corrosion inhibition[67]. In this study, the effects of almost every single oil component on the corrosion rate were examined. In particular, this study showed that naphthenic acids and long-chain organic acids in crude oil can form a hydrophobic film on the steel surface that acts as a corrosion inhibitor[67].

2.6 Produced water

The "produced water" is water, which originated in the underground oil deposits for thousands of years and was brought to the surface along with the oil[68]. The produced water contains organic and inorganic components as well as seawater. The chemistry of

produced water varies depending on the location of the oilfield and the type of crude oil, which is in the same well as the produced water. The major components of produced water from the oil fields are: dispersed oil, dissolved and soluble organic components, produced solid such as clay sands etc., scales such as calcium carbonate, bacteria and dissolved gases such as carbon dioxide and hydrogen sulfide[68]. Produced water is the main factor in the corrosion of carbon steel pipelines.

As mentioned above, seawater is one of the components in produced water. Seawater is injected during the drilling process to maintain the pressure inside the oil well. It is estimated that the seawater percentage, "water cut," in the extracted crude oil could reach up to 30% in the pipelines. In addition to decreasing the quality of the crude oil, this high percentage will expedite pipeline failure due to the increase in the corrosion rate inside the pipeline. Therefore, the separation of seawater from the crude oil becomes the major focus of many oil production companies. However, water-oil separation is very difficult. After the separation, the water must be cleaned before being released into the environment. As the production wells age, the water cut increases. When the water treatment plant is operating at 100% capacity the system cannot handle any higher water cut. Sometimes this means that the amount of oil produced is reduced due to the water plant capacity. Alternatively the investment in a larger water plant is required. The lowest cost approach however, is to allow more water into the transport pipeline, which lead to increase the corrosion rate inside the pipelines.

2.7 The phase transformation in iron corrosion products

Iron oxide, hydroxide, and oxide-hydroxide are the phases of iron oxides. The phases of the corrosion products depend on the temperature, the pH, the corrosive medium, and the oxygen concentration. These phases have a major impact on the corrosion rates of iron and steel. Some phases act as a protective layer that could impede the corrosion process. Others can expedite the corrosion process by working as cathode sites such as lepidocrocite. Therefore, identifying the corrosion forms as a function of time under various conditions is crucial for understanding the corrosion mechanism. These phases are mostly crystalline[69]. The crystal sizes vary according to the formation of the corrosion conditions. Under certain conditions, each phase can transform to another phase. There are two types of transformations, topotactic or reconstructive. Topotactic transformations occur when there are three dimensions between the initial phase and the final one. The internal atomic structure rearranges in a single crystal of the initial phase and transforms into a single crystal of another phase[69]. On the other hand, in the reconstructive transformation, there is no structural relationship between the initial and the final phases. Transformation occurs when the initial phase breaks down completely and the new phase precipitates[53].

The following forms of iron oxide are the common forms of iron oxide in crude oil pipelines:

1 Lepidocrocite (γ-FeOOH)

This form is the oxide hydroxide that is commonly formed from the oxidation of Fe^{2+}[69]. It has an orange color. The crystal structure of lepidocrocite is

an orthorhombic unit cell as shown in Figure 2-2. The structure consists of arrays of cubic closed packed (ccp) anions (O^{2-}/OH^-) stacked in one direction with Fe^{2+} ions occupying the octahedral interstices[69]. γ-FeOOH is unstable thermodynamically with $\Delta G_{f,298}$= -480.1 (kJ/mol), therefore, it can easily transfer to different form based on the conditions. Lepidocrocite is mostly considered as the first from of the transformation of the iron oxides and iron oxides hydroxide. γ-FeOOH is generally detected in the outermost of the corrosion layers while magnetite is detected in the inner layers[70,71].

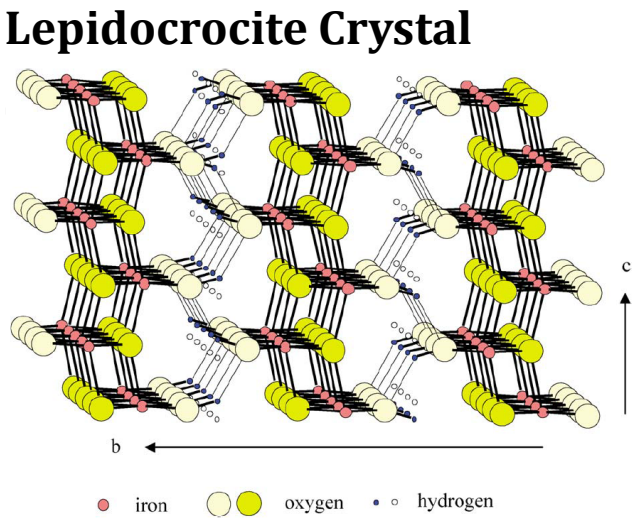

Figure 2-2 The crystal structure of lepidocrocite[72]

2 Goethite (α-FeOOH)

Goethite is another form of oxide hydroxide with yellow-brown color. It has an orthorhombic unit cell. The structure of goethite can be described as consisting of hexagonal closed packed (hcp) arrays of anions (O^{2-}/OH^-) stacked in one direction with Fe^{2+} ions occupying half the octahedral interstices within a layer as shown in Figure 2-3 [69]. Goethite is considered a stable form of iron oxide with $\Delta G_{f,298}$= -488.6 (kJ/mol)[69].

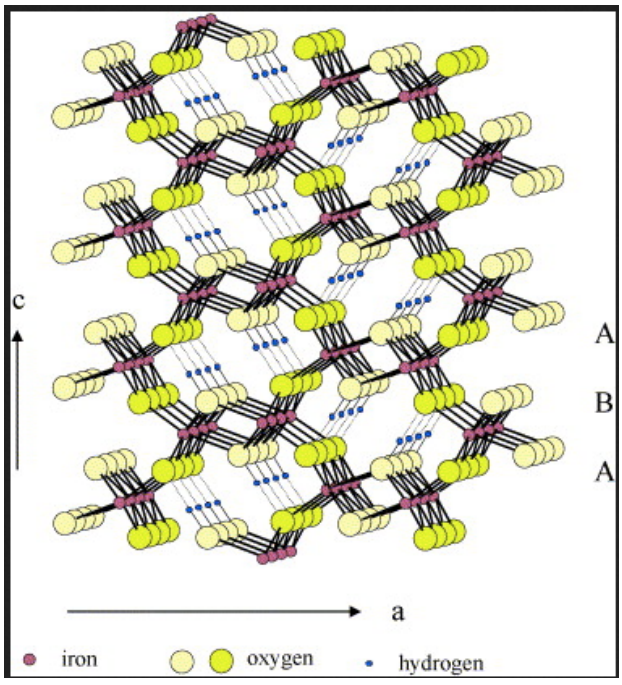

Figure 2-3 The crystal structure of goethite[72].

3 Hematite (α-Fe_2O_3)

Hematite was the first form of iron oxide discovered. Hematite is named based on its blood red color, where "haima" (Greek word) refers to blood.[69] As shown in Figure 2-4, the rhombohedra crystal structure of hematite consists of hcp arrays of oxygen ions stacked along [001] direction with Fe^{II} ions filled two third of the sites. The iron ions form six-fold rings[69]. Hematite is the most stable form of iron oxide with $\Delta G_{f,298}$= -742.2 (kJ/mol)[72].

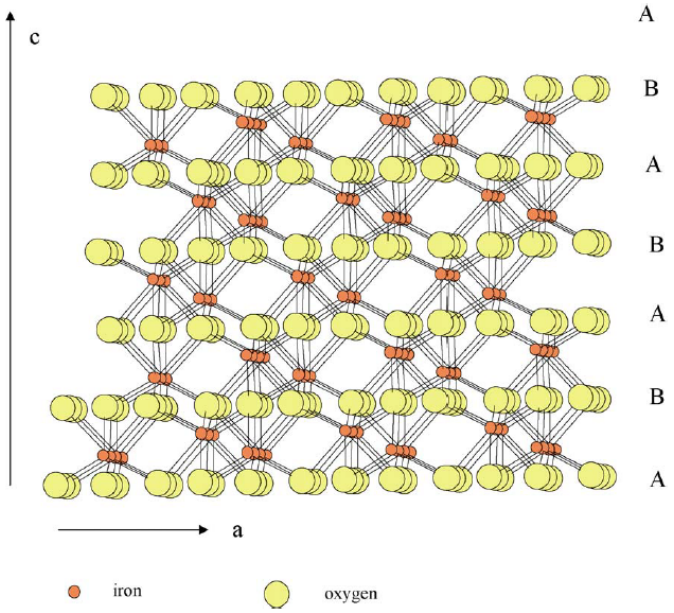

Figure 2-4 The crystal structure of hematite[72].

4 Magnetite (Fe_3O_4)

Magnetite is iron oxide with a black color that contains both Fe^{2+} and Fe^{3+} [69]. The crystal structure of magnetite is an inverse spinel with face-centered cubic unit cell as shown in Figure 2-5[72]. Magnetite was observed on the surface of carbon steel in many

different conditions and atmospheres. It can also be observed in the inner surface of corrosion products on carbon steel that was exposed to a marine atmosphere[70].

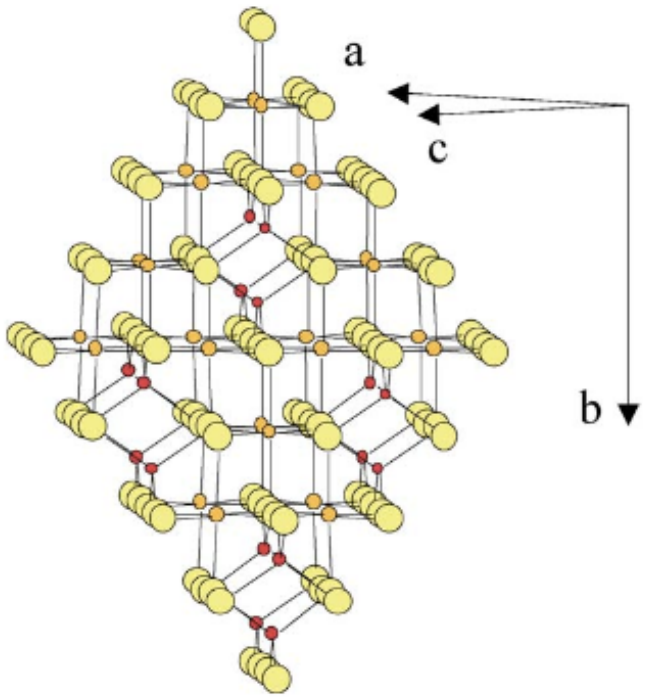

Figure 2-5 The crystal structure of magnetite and maghemite[72]

5 Green rust

Green rust consists of group of iron oxides that contain layers of $Fe^{2+}OH$ octahedral with Cl^- or SO_4^{2-} bonding between the layers[69]. Fe^{3+} is replaced by Fe^{2+} to maintain neutrality. Green rust has two types; green rust II and I. The green rust I has a rhombohedral structure while green rust II has a hexagonal structure. Green rust is usually formed as an intermediate compound in the rusting of iron at pH around neutrality[73,74].The formation of green rust can be a precipitation of aerial of ferrous

hydroxide ($FeOH^+$) in the presence of Cl^- or SO_4^{2-} or solid state transformation of $FeOH^+$ in aerial oxidation[73].

6 Ferric hydroxide $Fe(OH)_3$

Ferric hydroxide is also called ferrihydrite (FH). This form of iron hydroxide is amorphous[75]. Due to its high porosity, it has very high content of water. Therefore, ferric hydroxide resembles as swollen gel[73,76]. FH transforms to other iron oxides forms based on the solution pH, the concentration of Fe^{2+}/Fe^{3+} and the tmperatures[77,78]. Although, ferric hydroxide transforms to hematite at 60˚C and pH 7, however, Schwertmann found that ferric hydroxide did not transform to hematite at 70˚C and pH 6 even after two weeks[77]. However, after adding KOH to the solution at 70˚C, ferric hydroxide transformed to goethite[77]. It was reported that ferric hydroxide transformed rapidly to goethite at 0.05 Fe^{2+}/Fe^{3+}[78]. However, at Fe^{2+}/Fe^{3+} equal to 0.1, this transformation is suppressed, and then FH transformed into spinal iron oxide[78].

The iron oxide form	*Formula*	*ΔG (kJ/mol).*	*Color*	*Crystal structure*
Lepidocrocite	γ-FeOOH	-480.1	Orange	Orthorhombic (ccp anions)
Goethite	α-FeOOH	-488.6	Yellow-Brown	Orthorhombic (hcp anions)
Hematite	α-Fe_2O_3	-742.2	Red	Hexagonal (Rhombohedral)
Magnetite	Fe_3O_4	-1012.6	Black	Cubic
Green rust-SO_4		-3795	Green	Rhombohedral
Green rust-Cl		-2146		Hexagonal
Green rust-CO_3		-3590		

Table 2-1 The iron oxides forms with the crystal structure, the color and the Gibbs free energy for each form

2.7.1 Transformation of the corrosion products

During the corrosion process, the crystal structure of the corrosion layers transforms into different forms. Phase transformations depend on the temperature and pH of the solution. A study has shown that increasing the temperature changes the corrosion form on the surface of carbon steel[79]. In this study, the corrosion products of carbon steel in different electrolyte compositions at two different temperatures (20˚C-120˚C) were characterized by XRD and FTIR. The authors showed the change of the corrosion products for the same electrolyte compositions at different temperatures. Where the

corrosion products of carbon steel immersed in distilled water at 20˚C consists of a mixture of lepidocrocite and a small amount of magnetite. However, at 120˚C for the same electrolyte, a mixture of magnetite and small amount of goethite were formed on the surface of carbon steel[79].

Iron oxide phase transformation is very common during atmospheric corrosion. This is especially true when the wet/dry cycle acts as the driving force in this transformation.[80] During the wet/dry cycle, the corrosion products usually consist of lepidocrocite, which is partially reduced to Fe.OH.OH as an intermediate component at pH 6 [81]. Later, the intermediate and lepidocrocite are reduced to magnetite. This transformation has been explained in a crystallographic view[81]. As mentioned above, lepidocrocite has structure layers where the O^{2-} is arranged in ccp with Fe^{3+} occupying the octahedral holes. During the dehydration step, Fe^{2+} will move to the lepidocrocite lattice and occupy the tetrahedral and the octahedral holes. Also, H^{+} will move out of lepidocrocite lattice. Eventually, this change of structure will lead to magnetite formation.

Another type of transformation is lepidocrocite transformation to goethite in a semi-rural atmosphere. In the presence of SO_2, dissolution and conversion of γ-FeOOH to amorphous ferric oxyhydroxide ($FeO_x(OH)_{3-2x}$) with pH ~ 4.[82] This transformation can be catalyzed by the presence of Cu, P and Cr elements in the metal. This amorphous ferric oxyhydroxide forms a protective uniform layer against the atmospheric corrosion[82].

T. Misawa stated that green rust could be transformed to magnetite by a solid-state transformation in slow aerial oxidation or transform to lepidocrocite by rapid oxidation[73]. The formation of magnetite from green rust required oxygen removal and a

rearrangement of the iron and oxygen in the crystal lattice, therefore, this transformation takes a long time to occur[73].

Goethite transforms to hematite without intermediate at high temperature (533K), while lepidocrocite can transform to maghemite at 473-553 K, then to hematite at higher temperatures[69].

2.8 The factors affecting the corrosion rate in crude oil pipelines

As mentioned previously, the main factor in the corrosion of carbon steel pipelines is the presence of produced water. The major components of produced water from the oil fields include dispersed oil, dissolved and soluble organic components, produced solids such as clay sands, scales such as calcium carbonate, seawater, bacteria and dissolved gases such as carbon dioxide and hydrogen sulfide[68]. Unlike in the presence of seawater, many studies have investigated the individual effect of each of these solutes in produced water[40,43,45,58,66,83–85].

In addition of the produced water, there are operational factors that affect the corrosion process inside crude oil pipelines:

- **Oxygen concentration**: Oxygen reduction is typically the cathodic reaction of crude oil corrosion; therefore, the corrosion rate depends on the oxygen concentration in the crude oil. As the corrosion layers are formed, the diffusion of oxygen through these layers decreases[4]. As a result, it is expected that the corrosion process will be impeded, and eventually will stop[4]. However, in crude oil pipelines, the flow is

relatively high, and therefore, most of the corrosion layers from the metal surface are stripped from the pipeline surface leading to a decrease in the thickness of these corrosion layers. Hence, the diffusion of oxygen is allowed to penetrate into deeper areas of corrosion thereby enhancing the corrosion rate. So, in general, the corrosion rates during oil transportation inside the pipelines could increase or decrease depending on the oxygen concentration.

- **Temperature**: The temperature has also been shown to have a significant impact on the rate of the crude oil pipeline corrosion. Similar to many reactions, the corrosion rate of carbon steel in crude oil increases with increasing temperature[86]. It should be mentioned that, while the oxygen diffusion coefficient increases with increasing the temperature, the oxygen solubility decreases as well. These combined effects of temperature on the corrosion rates on the carbon steel have been investigated.

- **Flow rate**: It is very well documented in the literature that the increase of the flow rate enhances the erosion corrosion[47]. The high flow rate removes the protective corrosion layers, inhibitors, and protective precipitates from the surface of the carbon steel. Consequently, the erosion corrosion causes the surface to be exposed to the surroundings leading to electrochemically–induced corrosion reactions. Therefore, it is expected that, in the absence of the erosion corrosion, whereby the flow rate is low or stagnant, the corrosion rate decreases and eventually stops.

- **Water concentration**: In the water/crude oil mixtures, the mechanism of the water concentration on the corrosion rate is poorly understood, and there are very limited publications on this subject[66]. Hence, my work involves studying this important issue in the corrosion of crude oil pipelines.

- **The crystal structures of the corrosion layers:** During the corrosion process, the crystal structure of iron oxide transforms to different forms. Phase transformation depends on the temperature and pH of the solution, where a higher rate of transformation occurs at higher temperatures[87,88].The transformation of lepidocrocite (γ-FeOOH) to maghemite and then to hematite occurs when the metal is heated in a dry environment without the presence of oxygen at high temperature[69]. However, this transformation is also observed during the atmospheric corrosion at ambient conditions. In atmospheric corrosion, the transformation starts with carbon steel oxidizing to form ferrihydrite phase as an intermediate phase[89]. Ferrihydrite is not a stable phase, and will transform to lepidocrocite or goethite depending on the local environmental conditions of the site of corrosion[12,90]. Goethite is thermodynamically stable, which decreases the corrosion rate[80]. Therefore, it is expected that the corrosion rate increases or decreases depending on the crystal structure of the corrosion layers. The diffusion of oxygen thorough the corrosion layers depends on the crystal of the corrosion product. As shown in Figure 2-2, and Figure 2-4, oxygen can easily diffuse through lepidocrocite, while it is difficult to diffuse in hematite, which has a low concentration of structural defects.

2.9 The Effect and Economic Impact of Corrosion

The cost of the damage of corrosion-induced pipeline failure can economically be significant. For example, in the United States alone, the average annual corrosion-related costs for the gas-liquid pipelines amount to about $1.37 billion per year, according to National Association of Corrosion Engineering (NACE)[60]. These costs cover the works and materials used to monitor, replace, and maintain these pipelines.

The cost of corrosion has increased significantly between 1978- 2016. In 1978, National Association of Corrosion Engineering (NACE) released a study on the economic effect of corrosion in the United States. The study showed that the cost of corrosion in the United States for the year 1975 was $70 billion[92]. However, the cost of corrosion in 2016 according to NACE is $2.5 trillion[93]. In the advanced industrial countries such as the United States, Japan, Germany and United Kingdom, the annual corrosion cost is greater than the combined cost of all natural disasters[94]. Finally, 15% of the crude oil incidents (spills, etc.) have been caused by internal corrosion over the past few years[94].

3 Experimental Methods and Materials

To evaluate the effect of seawater in the crude oil on the corrosion of carbon steel in the pipelines, a number of analytical and characteristic methods were utilized. The description of these methods is explicated in this chapter. A discussion of the materials used in this study, and the instrumentation used to investigate the changes in the chemical compositions of corrosion products, which formed under various conditions can be found below

3.1 Materials

As mentioned earlier, mild carbon steel is a common pipeline material used in oil and gas production. Therefore in this work, mild carbon steel is used in all experiments with chemical composition shown in Table 3-3-1. The surface morphology and the cross-sectional image for the carbon steel coupon before use are illustrated in Figure 3-3-1. Carbon steel coupons with different dimensions for each experimental setup are obtained from the Metal Sample Company. Natural seawater was collected from Petco INC without further modifications. Table 3-3-2 shows various concentrations of elements in the seawater. These elements will exist in various ionic forms in the seawater environment.

Element	C	Cu	Mn	Si	P	S	Cr	Ni	Mo	Fe
Wt.%	0.16	0.16	0.755	0.17	0.013	0.02	0.048	0.078	0.014	Balanced

Table 3-3-1 The chemical compositions of the carbon steel

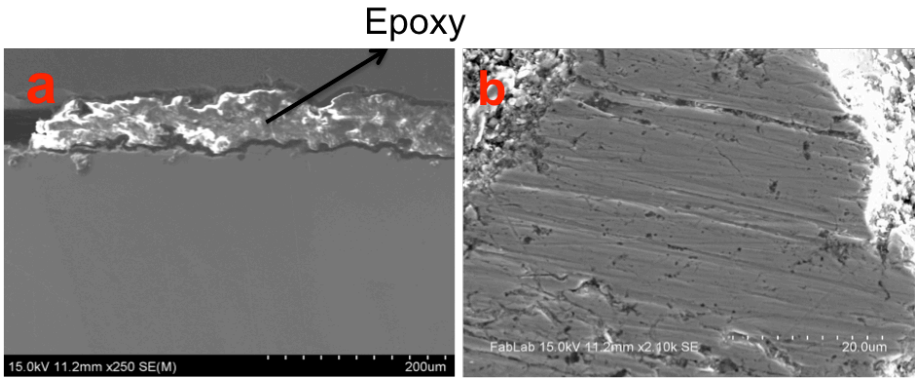

Figure 3-3-1 SEM images for the carbon steel coupons before immersion (a) surface image (b) cross sectional

Ions of Following Elements	Concentration (ppb)
Cl	**1.91×10^7**
Na	**1.08×10^7**
Mg	**1.33×10^6**
Ca	**4.22×10^5**
Li	**170**
U	**3 - 3.3**
Fe	**1 – 2**
V	**1.5**
Pb	**0.03**

Table 3-3-2 Various concentrations of elements in the seawater

3.2 Experimental setup

The experimental tests were performed using the following three experimental designs:

1. As illustrated in Figure 3-3-2, a Pyrex glass bottle with a 250 ml volume was placed on a magnetic hot plate starrier. To keep the temperature constant, a

temperature bath was used. The coupon is a flat strip with dimensions 7.3 X 2.3 X 0.23 cm. After the carbon steel coupons were immersed in the corrosive media, the bottles were covered by parafilm under the bottle lid to create a closed system.

Figure 3-3-2 Experimental setup of a Pyrex bottle

2 Flow loop: A pipeline loop has been constructed as shown in Figure 3-3-3. The closed loop was constructed to measure the corrosion rate of carbon steel under flow conditions typical of crude oil pipelines. The loop can record flow rates up to 200 gallons per minute with a velocity of approx. 2.7 meters/second. The system is designed to circulate natural fresh water, high salinity seawater, and viscous oils. The flow system can monitor, record, and control system parameters over extended test

durations. Flow rate is continuously monitored with an FTB-700 Turbine flow meter and Omega DPF-75A rate display. System temperature is controlled with a dual thermostat temperature control system which is comprised of two (2) 1/4" thermal probes located on each side of the sample test section, a 20A heating circuit, and a new 3Ton cooling loop circuit that has been integrated from the reservoir. The Clepco heating unit circuit works in tandem with a 230V Pentair In-Line Air-cooled Chiller unit circuit. A cooling system is outfitted with a 30gpm pump and allows for precise control of environment temperature of accuracy within ±0.5°Cof thermostat set point value. The Pentair chiller system circuit operates a 1HP chiller with Nominal BTU 12,000 capacity and fully compensates for system heat transfer by pump energy. The combination of these two systems working together allow for a wide test range including temperature settings below 20°C. pH and dissolved oxygen sensors have been installed to the reservoir for monitoring and recording real-time test environment data. These sensors and all temperature monitoring components are equipped with digital monitors and analog output to a LabJack U3 data acquisition device for recording and post-experiment analysis. Three carbon steel coupons with different sizes were used for each temperature. The coupons are flat strip with dimensions 7.3 X 2.3 X 0.23 cm.

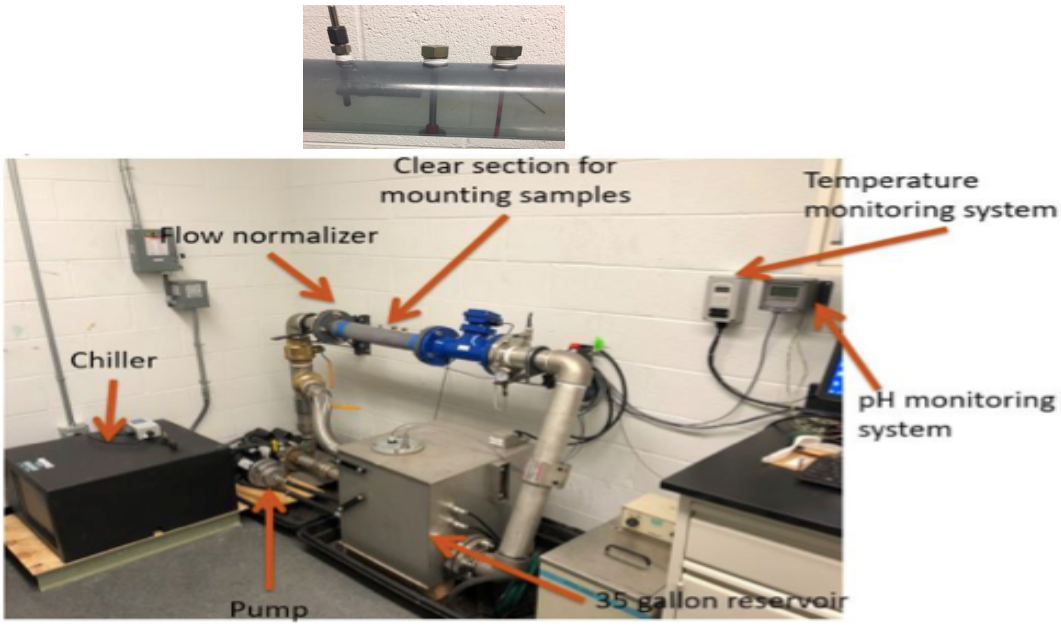

Figure 3-3-3 Flow loop with high flow rate up to 192 gal/min

3. Corrosion cell: The electrochemical measurements have been conducted using a corrosion cell. The cell as shown in Figure 3-3-4 consists of three electrodes, working electrode (carbon steel), reference electrode (Ag/AgCl) and counter electrode (graphite). Linear polarization resistance (LPR) and Tafel plot extrapolation have been performed to measure the kinetics of the carbon steel corrosion in seawater. The electrochemical measurements were performed using Gamry Potentiostat with Echem Analyst software.

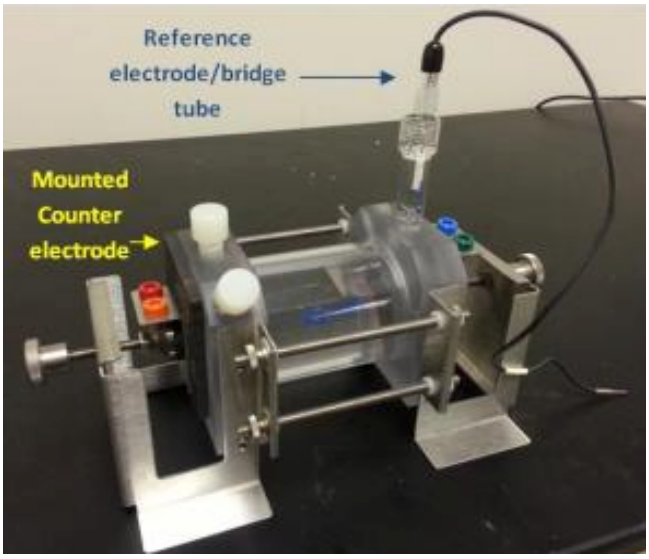

Figure 3-3-4 The corrosion cell set up with carbon steel as working electrode, graphite as a counter electrode and Ag/AgCl as a reference electrode

3.3 The Elucidation of the corrosion mechanism in the crude oil

The strategy of elucidation the corrosion mechanism was achieved using the following:

i. Determining the corrosion rate gravimetrically and electrochemically

ii. Examining the surface morphology of the corroded carbon steel surface.

iii. Examining the elemental compositions of the corrosion products on the carbon steel surface.

iv. Identifying the iron oxides forms of the corrosion products.

v. Identifying the crystal structures of the corrosion products.

3.2.1 Determination of the corrosion rates:

3.2.1.1 Gravimetric method:

The classic method of determining the corrosion rate is in terms of mass loss per unit time. The coupons were polished with SiC papers with P800 grit prior to their immersion in the corrosive medium. Then, they were rinsed with acetone followed with deionized water. The coupons were weighed before the exposure to the corrosive medium. After a certain time, the coupons are taken out and cleaned according to ASTM G1-03.[95] Corrosion products on the coupons surfaces were removed chemically by immersion in a solution (500 ml HCl + 500 ml distilled water + 3.5 g hexamethylenetetramine as acid inhibitor) at 25 ˚C. After removal of corrosion products, the coupons were ultrasonically cleaned with distilled water up to 1000 ml. Then electrolytic cleaning was conducted on the coupons using graphite as an anode in a solution of 75 g sodium hydroxide, 75 g sodium carbonate, 25 g sodium sulfate and distilled water up to 1000 ml at 25 ˚C. The coupons were then weighed to determine their mass loss. The mass difference is used in the following equation[95]:

$$\textbf{Corrosion rate (mpy)} = \frac{\mathbf{3.45 * 10^6 * \Delta m}}{\mathbf{d * t * A}} \qquad \textbf{Equation 3-3-1}$$

Where: mpy = mils per year, Δm = Mass difference (g), d = metal density (g/cm^3), t = time for exposure (hr.), and A = cross sectional area of exposure (cm^2).

All experiments were repeated with three duplicate specimens to confirm reproducibility of the results. Corrosion rates are reported as the mean with error bars representing the standard error of the mean (SEM) from three measurements.

3.2.1.2 Tafel Plot

Tafel plot is used to understand the behavior of the anodic and cathodic reactions. An overpotential is the additional potential that is needed to drive a reaction at a certain rate[19]. The current (i) is related exponentially to the overpotential (η) based on Tafel equation as follows[19]:

$$\boldsymbol{\eta = \beta \log \frac{i}{i_o}} \qquad \textbf{Equation 3-3-2}$$

Where i_o = exchange current density β = Tafel constant $= \frac{\beta_a \beta_c}{2.303\beta_a + \beta_c}$

β_a= The anodic Tafel constant in volt/dec

β_c = The cathodic Tafel constant in volts/decade

This method involves the determination of Tafel constants. The specimen is polarized anodically (positive potential) and catholically (negative potential) from the corrosion potential E_{corr}. The slopes of these lines are Tafel constants. I_{corr} can be obtained from the Tafel plot by extrapolating the linear part of the curve as shown in Figure 3-3-5[19].

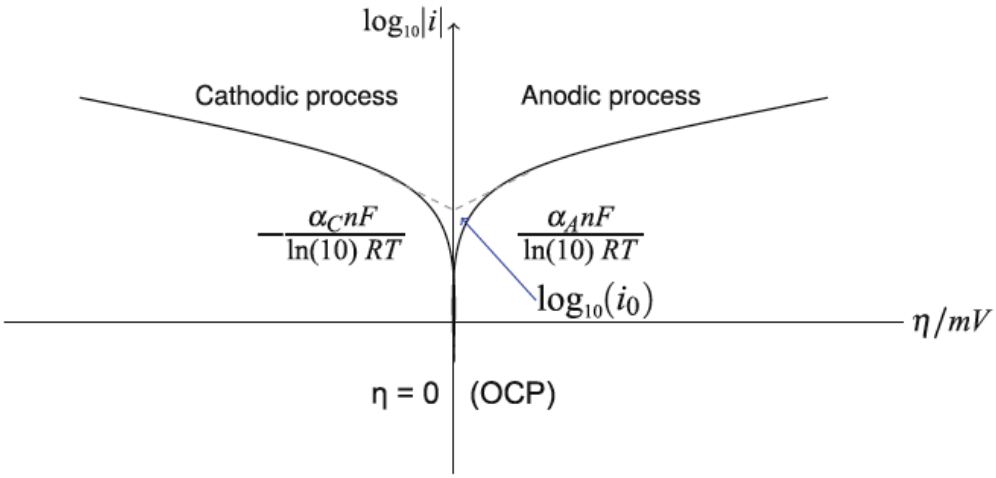

Figure 3-3-5 Typical Tafel plot[19]

3.2.1.3 Linear Polarization Resistance (LPR)

Linear polarization resistance is a well-known, common method in corrosion studies. Polarization means that the potential electrode shifts away from the potential equilibrium[96]. Polarization causes current flow due to the electrochemical reaction, the resistance to this current flow is called polarization resistance (R_p), where is linear part in the curve near the overpotential. The plot will be a straight line with slope equal to the polarization resistance (R_p). Then, R_p will be used to determine the corrosion current density i_{corr} in the Stren-Geary equation as shown below[97]:

$$\mathbf{R_p} = \frac{\mathbf{\Delta E}}{\mathbf{\Delta i}} \qquad \text{Equation 3-3-3}$$

$$\mathbf{i_{corr}} = \frac{\mathbf{1}}{\mathbf{2.303}} \frac{\mathbf{\beta_a \beta_c}}{\mathbf{(\beta_a + \beta_c)}} \frac{\mathbf{1}}{\mathbf{R_P}} \qquad \text{Equation 3-3-4}$$

Then, i_{corr} will then be used to calculate the corrosion rate as following:

$$\mathbf{Corr.\,rate\ (mpy)} = \frac{\mathbf{0.3}\ \boldsymbol{I_{corr}(E.W)}}{\boldsymbol{d}} \qquad \text{Equation 3-3-5}$$

Where: I_{corr} = current density ($\mu A/cm^2$), E.W = the equivalent weight of the corroding species (g), and d = density of the corroded species (g/cm^2).

It should be mentioned that Tafel constants in Equation 3-3-4 are obtained from the Tafel plot. Therefore, LPR is always calculated after Tafel plot measurements. The LPR measurement was conducted with a Gamry Potentiostat at a scan rate of 10 mV/min starting from a potential of -250 to 250 mV versus an open circuit potential (OCP). The carbon steel coupons were left at OCP for 300 s. Prior to the electrochemical measurements, the coupons were degreased with acetone, followed with a DI water rinse.

3.2.2 Sample Characterization Techniques

Studying the corrosion products requires characterization of both the composition (elemental content, phase identity) and the morphology (shape and distribution of the grains of the various phases). The morphology is characterized using a microscopy technique. In general, sample preparation procedures have to be carefully applied in order to obtain reliable and informative results. The composition is characterized using spectroscopic methods**.** The following techniques were employed to characterize the mechanism of carbon steel corrosion in crude oil pipelines:

3.2.2.1 Examining the surface morphology of the corroded carbon steel surface

The surface morphology and the cross-section analyses of the corroded carbon steel are performed using scanning electron microscopy and energy dispersive X-ray spectroscopy (SEM-EDS). Mapping of O and Fe are carried out to investigate the distribution of these elements on the surface of the carbon steel. The average of many

spots on the corroded coupon with 75 μm width is measured. Moreover, pits and cracks can be observed by SEM-EDS, which can be used in EIS data interpretation. A Hitachi S-3400 variable pressure SEM equipped with an EDS detector are used. Prior to SEM analysis, the corroded coupons are put in a desiccator for 24 hours to dry.

3.2.2.1.1 Coupons preparation for cross sectional

The corroded carbon steel coupons were cut and mounted with epoxy on silicon plates. A slow speed diamond saw was used to cut all these coupons. The surface was polished with silicon carbide paper. Precautions were made to protect the corrosion layers from destruction during the polishing. The cross sectional analysis was carried out using Hitachi SU-70 (SEM-EDS).

3.2.2.2 Examining the elemental compositions of the corrosion products on the carbon steel surface.

X-ray Photoelectron Spectroscopy (XPS) is a technique that provides the elemental compositions of the corroded metal surface. X-ray photoelectron spectroscopy (XPS) was performed using a Kratos Axis 165 X-ray photoelectron spectrometer operating in hybrid mode using monochromated aluminum Kα X rays (1486.7 eV) at 240 W. Powder samples were mounted on a sample holder using double sided copper adhesive tape from 3M. Charge neutralization was used to minimize sample charging and the pressure of the system was maintained at $5x10^{-8}$ or lower throughout the measurement. Pass energies of 160 eV and 40 eV were used for survey and high-resolution spectra respectively. Data Analysis was done using CASAXPS, oxygen 1s

spectra were fitted to three peaks corresponding to O^{2-}, OH and H_2O with line shapes generated from a 70% Gaussian, 30% Lorentzian product function after application of a Shirley background. The OH and H_2O peaks were constrained to have equal full-width at half maximum and the H_2O peak was further constrained to be separated from the O2- peak by 3.2 eV. All spectra were calibrated to the corresponding adventitious hydrocarbon peak at 284.8 eV. Elemental composition was quantified using CASA XPS from peak areas adjusted by relative sensitivity factors from the Kratos Vision library and transmission functions from the instrument. Prior to the analysis, the samples (corrosion powder) were prepared by washing with DI water for multiple times to wash all seawater salts. After each wash, the samples were filtered using 12 cm filter. At the end of washing, the samples were put in dissector to dry.

3.2.2.3 Identifying the iron oxides forms of the corrosion products

Raman spectroscopy was performed on samples using a Horiba Jobin Yvon Raman microscope (LabRam Aramis Model). The specimens were excited with a Ventus 532 nm diode-pumped solid-state laser from Laser Quantum. A 50X objective with a numerical aperture of 0.75 lens was used resulting in a laser spotlight of ~865 nm on the sample surface. The corrosion products were found to be sensitive to decomposition under the laser so a D3 neutral density filter was used resulting in approximately 240μA power at the sample surface.

In addition, Fourier transform infrared spectroscopy (FTIR) has been employed to identify the iron oxide forms in the corrosion layers. A Nicolet Nexus 670 Fourier Transform Infrared Spectrometer (FTIR) equipped with a liquid nitrogen cooled mercury

cadmium telluride (MCT) detector has been used. Background spectra were obtained prior to each different sample number and the surface of the ATR module was cleaned with organic solvent and dried prior to starting the next sample analysis. Absorption peaks were identified and quantified.

3.2.2.4 Identifying the crystal structures of the corrosion products

The crystal structures of the corrosion products were characterized by D8 advanced powder XRD diffractometer with LynxEye detector using copper tube as radiation, 40 kV and 100 mA. The XRD patterns were analyzed by the diffraction database. Needless to say, XRD cannot detect the amorphous signature in the corrosion layer. Prior to the analysis, the corrosion layers were scraped off the corroded carbon steel, and dried in desiccator for 2-3 days.

3.2.3 The difference between the gravimetric and the electrochemical measurements

While gravimetric and electrochemical measurements have both been used to measure the corrosion rates of different compounds, the corrosion rate calculated from each method could be different due to the build-up of the corrosion products on the surface of the metal samples. Zou, et al. measured the corrosion of mild carbon steel in seawater using electrochemical and gravimetric methods[98]. It was found that the electrochemical measurements coincide with weight loss at short time scales near the

beginning of the immersion period; however, it was also found that the electrochemical measurements begin to differ from the weight loss after long time periods of immersion. This discrepancy is believed to be due to the build-up of corrosion layers on the surface of carbon steel after a long immersion time. Early on in the corrosion process, before a corrosion layer has been built up, oxygen diffuses towards the metal surface where it can participate in a cathodic reaction. After the layers of corrosion reach a certain thickness, oxygen diffusion is significantly reduced. As a result, the corrosion layers that contain a large amount of β-FeOOH participated in the cathodic reaction, which lead to an overestimation of the electrochemical measurement[98]. However, Yang observed after the accumulation of corrosion products on the surface, the current density from electrochemical measurements was higher than the one from weight loss measurement[14].

4 Results and Discussion

Over the course of this work, several experimental set-ups and characterization techniques were employed to fulfill the main objective of this study. The corrosion rates of the carbon steel were determined under various conditions.

4.1 Determination the effects of the temperature on the corrosion rates with low velocity (0.15 m/s) for 14 Days

The corrosion rates of the carbon steel in seawater were determined at various conditions. During these experiments, only a single variable was chosen, all other experimental variables are kept constant. Precautions were made to avoid the erosion corrosion during the measurements of the corrosion rates and the identification of the corrosion products. Hence these experiments were carried out at a low velocity of 0.15 m/s (60 rpm) for 14 days. Figure 4-1 shows the carbon steel coupons after immersion in seawater at various temperatures. These coupons are covered with corrosion products with various colors, which indicate the change in the forms of the corrosion products. The orange color indicates the presence of lepidocrocite, whereas dark brown indicates hematite and the black color indicates magnetite[99].

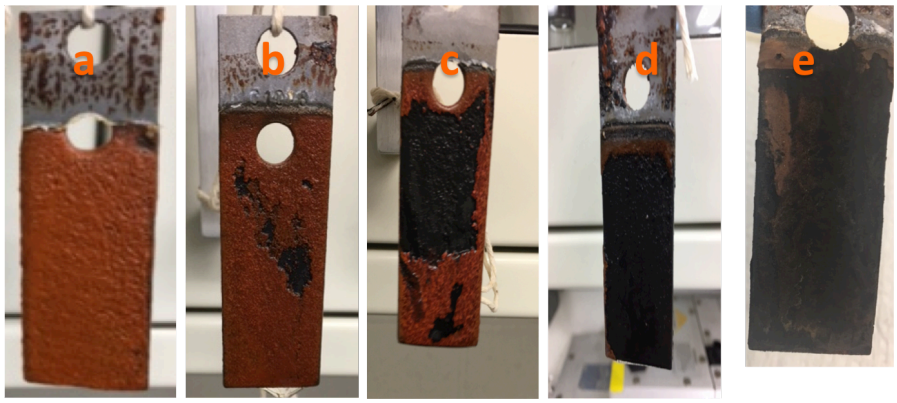

Figure 4-1 Picture of corroded carbon steel coupons after immersing in seawater for 14 days with low velocity (0.15 m/s) in the stirred beaker, at (a) 25, (b) 35, (c) 45, (d) 55 and (e) 65^0C

4.1.1 Determination of the corrosion rate

As expected, Figure 4-2 shows that the corrosion rate increases as a function of temperature of the carbon steel coupons immersed in seawater for 14 days. These results show that the temperature dependency of the corrosion rate is not constant. While the corrosion rate is 0.21 ± 0.2% mm/year at 25˚C, it increases to 0.33 ± 0.2% mm/year at 35˚C. However, no increases in the corrosion rates are observed between 35˚C and 45˚C. At temperatures higher than 45˚C, the corrosion rate increases at a constant rate of approximately 100 microns per year per 10˚C. As shown later this is due to the change in crystal structure of the corrosion layers. Moreover, it should be mentioned that these results show that the corrosion rate doubled for each increment of 30˚C. This may indicate that the diffusion of oxygen through the corrosion layers has become more the predominant process than the activation process[100]. As mentioned in the introduction, that the corrosion process includes two major components: diffusion and activation processes.

At temperatures higher than 45˚C, the corrosion rate increases at a constant rate of approximately 100 microns per year per 10˚C.

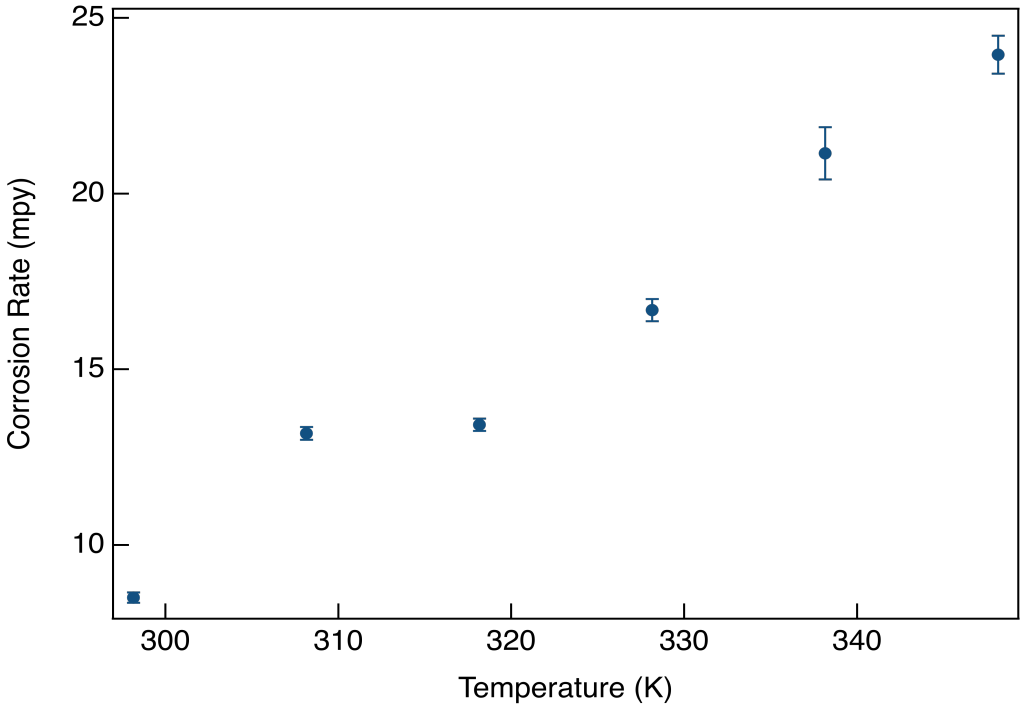

Figure 4-2 The corrosion rate of carbon steel that immersed in seawater in a stirrer beaker with low velocity (0.15 m/ s) as function of temperature for 14 days

4.1.2 Determination of the activation energy and thermodynamic parameters:

Figure 4-3 represents the overall Arrhenius plot that covers a wide range of temperature of 25˚C-75 ˚C with activation energy of 12.7 kJ/mole. This value cannot be considered as activation energy for this process, since the temperature has positive and negative effects on the corrosion rate. While the temperature increases the rate of the corrosion chemical reactions, and also increases the diffusion of oxygen through the corrosion layers, it also decreases the solubility of oxygen in the aqueous solutions leading to the decrease of corrosion rate. More importantly, as we can see in Figure 4-3

below, the temperature changes the structure of the corrosion products, which lead to the changes to the oxygen diffusion. This may indicate that the diffusion of oxygen through the corrosion layer becomes the predominant process[100]. Thus the effect of the temperature on the corrosion rate can be explained by the changes of chemical compositions of the corrosion layers. Consequently, it is clear that the identification of the chemical composition of the corrosion layers will lead to better understanding the mechanism of the corrosion as a function of temperature.

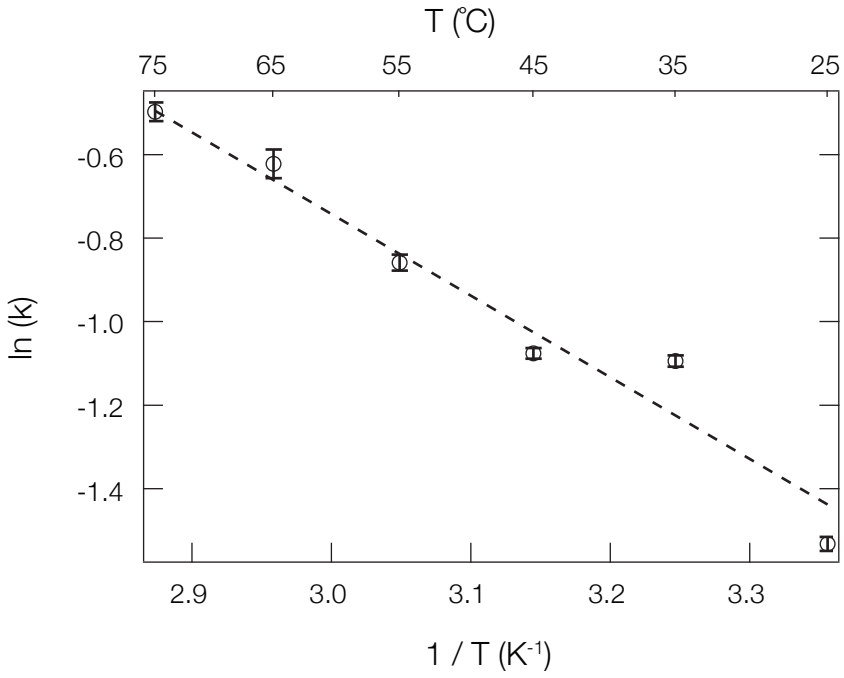

Figure 4-3 Arrhenius plot for carbon steel coupons that was immersed in seawater a stirred beaker for 14 days with low velocity (0.15 m/s) at various temperatures.

4.1.3 The identification of seawater-exposed carbon steel surface morphology using SEM-EDS

The surface morphology of the rust products formed on the surface of the mild carbon steel coupons showed significant changes at various temperatures. As shown in Figure 4-4, the iron oxide layer formed after 14 days in seawater at 25 °C resulted in the formation of a mixture of small crystalline globules (sandy crystals) and fine plates (flowery structures). The shape of such crystallites is typical for lepidocrocite (γ-FeOOH)[96–98]. At a higher temperature (45 °C), the surface morphology of the iron oxide layer formed was significantly different and not as homogeneous as the one observed at 25 °C. Several crystalline shapes can be observed, including plates, spindles, and pseudo-cubes, which could be indicative of the formation of various hematite crystals as shown in Figure 4-4. These shapes can act as seeds during the transformation of lepidocrocite to hematite as the temperature increases resulting the formation of various crystal shapes. Also, at the highest temperature of 75 °C, the morphology of the rust layer changed again exhibiting the presence of clusters of globules with a semi-cubical structure. These structures correspond to magnetite crystals and are typically formed by several aggregates of smaller nanometer-sized crystals[99,104].Another important observation is that there is a considerably higher porosity in addition to the presence of cracks. As shown in Figure 4-5, the iron oxide layers formed at 65 and 75 °C revealed the presence of irregular shape and size cracks. Therefore, these non-protective rust layers, especially below 35 ˚C, allow the diffusion of corrosive species, such as Cl^- ions, into the surface of mild carbon steel and consequently promote further oxidation. However, in the case of

the presence of magnetite at 75 °C, no cracking or spallation of the rust layer was observed, although the porosity is still high.

After cleaning the surface of the coupons thereby removing the iron oxide layers formed, pitting corrosion of the mild carbon steel surfaces was observed, as shown in Figure 4-5. Pits of various shapes, sizes, and depths were present. It is worth mentioning that a closer inspection of the clean surface of the corroded coupons revealed the presence of erosion corrosion, as well, shown in Figure 4-5. (Image on the right).

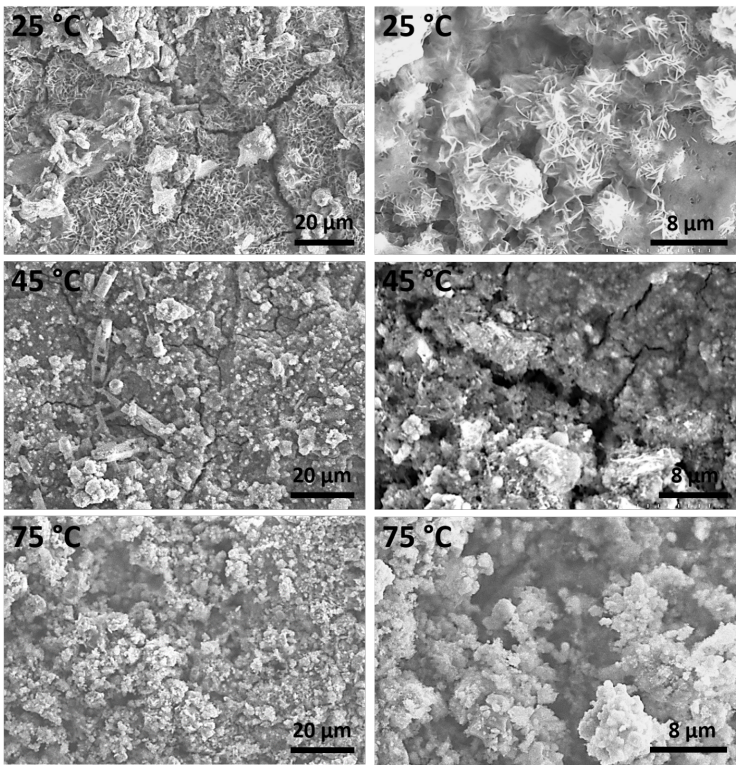

Figure 4-4 SEM micrographs showing the different morphologies of the rust layers formed on the surface of mild carbon steel coupons immersed in a stirrer beaker with seawater under low flow rate (60 rpm): lepidocrocite at 25 °C, hematite at 45 °C, and magnetite at 75 °C.

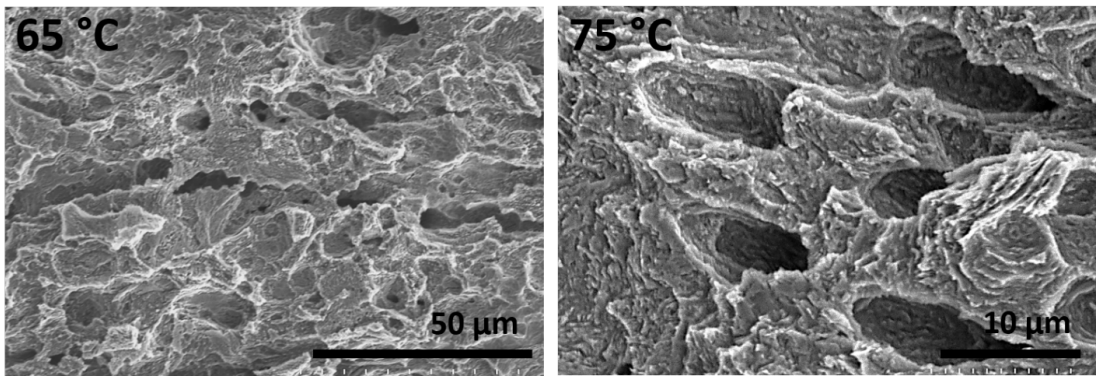

Figure 4-5 SEM micrographs of the corroded mild carbon steel surface under low flow rate (60 rpm) after the removal of rust layers

4.1.4 The identification of the corrosion products at various temperatures

Since the corrosion products of the carbon steel were present in crystalline and amorphous forms, we identified the crystalline iron oxides using XRD and other techniques such as Raman and XPS. For the other amorphous forms of iron oxides, we used only Raman and XPS.

As shown in Figure 4-6 and Table 4-1, the corrosion products have different forms of iron oxide and iron oxide hydroxide as a function of temperature. The structures of the corrosion products were characterized and quantitatively measured for a temperature range from 25 °C to 75 °C. At 25 °C and 35 °C, the XRD shows that the outer rust layer contains high (60 ± 10) % of orthorhombic structure belong to γ-iron (III) oxide hydroxide (lepidocrocite), while the inner rust layer contains low amount (40 ±10)% of cubic structure of magnetite. At 45 °C, the corrosion products consist of (55± 9.4)% of hematite and (44.8 ± 9.4)% magnetite. Moreover, at temperatures higher than 45 °C, no iron oxide hydroxide was observed. The XRD results also show that the outer rust

layer contains (74 ± 9) % hematite with rhombohedral structure, and the inner rust layer (26 ± 9) % magnetite. Hematite and magnetite were present in the corrosion products at temperature range of 45 °C – 65 °C. At 75 °C, magnetite was the only product present

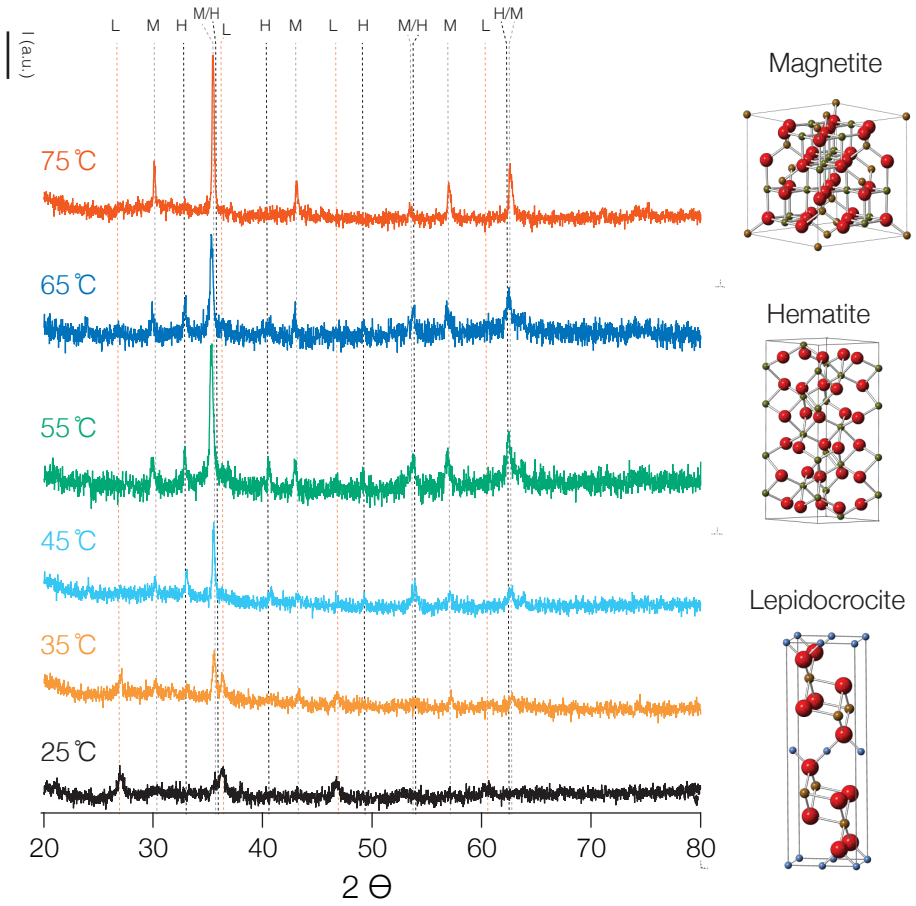

Figure 4-6 XRD pattern for the corrosion products on the surface of carbon steel immersed in seawater with low velocity of 0.15 m/s at various temperatures

Temperature	*Name*	***Formula***	***Percentage***	*Crystal structure*
25 ˚C	Lepidocrocite	γ-FeOOH	73.7 ±10	Orthorhombic (ccp anions)
	Magnetite	Fe_3O_4	26.3 ± 10	Cubic
35 ˚C	Lepidocrocite	γ-FeOOH	58.4 ± 4.5	Orthorhombic (ccp anions
	Magnetite	Fe_3O_4	41.6 ±4.5	Cubic
45 ˚C	Hematite	Fe_2O_3	55.2 ± 9.4	Hexagonal (Rhombohedral)
	Magnetite	Fe_3O_4	44.8 ± 9.4	Cubic
55˚C	Hematite	Fe_2O_3	54.7 ±7.3	Hexagonal (Rhombohedral)
	Magnetite	Fe_3O_4	45.3 ±7.3	Cubic
65 ˚C	Hematite	Fe_2O_3	55.2 ±9.4	Hexagonal (Rhombohedral)
	Magnetite	Fe_3O_4	44.8 ±9.4	Cubic
75 ˚C	Magnetite	Fe_3O_4	100 ±0	Cubic

Table 4-1 Changes observed in the crystal structure of corrosion layers on the carbon steel in seawater under low velocity of 0.15 m/s as function of temperatures with the standard error of the mean

To further characterize the iron oxide corrosion products on the surface of carbon steel, Raman spectroscopy was conducted on the rust layers produced by conditioning at 25 °C, 45 °C, and 75 °C. The Raman spectra obtained are shown in Figure 4-7 and were fitted using an unconstrained Gaussian peaks model to identify the peak positions (Table 4-2). At 25 °C, the Raman spectrum revealed a mixture of iron oxides (Fe_3O_4) and oxyhydroxides (γ-FeOOH and α-FeOOH). The peaks at 245, 297, and 393 cm^{-1} and the broad peaks around 650 cm^{-1} indicate the presence of lepidocrocite (γ-FeOOH) and

goethite (α-FeOOH) respectively.[105–111] Additionally, the broad peak at 1304 cm^{-1} is one of the important peaks of lepidocrocite, as reported by several investigators[104,105,107–111]. Lastly, the peaks at 298, 533, and 664 cm^{-1} are characteristic peaks of the iron oxide compound Fe_3O_4, known as magnetite [105–108,108–111]. The corrosion products present at 45 °C show some changes in the consistency with a strong peak at 671 cm^{-1} revealing the presence of some iron oxides, potentially magnetite and/or maghemite (γ-Fe_2O_3) and the deconvoluted peak at 717 cm^{-1} further supports the presence of maghemite [105,106,108,112]. The peaks at 399 and 489 cm^{-1} may indicate the presence of goethite, as well as maghemite [107–110,113]. Also, the presence of oxyhydroxides in the corrosion products at 45 °C is further enhanced by the strong peak at 1307 cm^{-1} which corresponds lepidocrocite [105–108,108,110,111]. Lastly, the Raman spectrum at 45 °C revealed a new sharp and strong peak at 283 cm^{-1} which could be attributed to the formation of hematite (α-Fe_2O_3) [106–111].The presence of hematite as the temperature increases is expected, since studies have shown that thermal dehydration of corrosion products such as lepidocrocite and goethite give rise to hematite through topotactic transformation[107–111,113]. At the highest temperature (75 °C) goethite is still present in the corrosion products. The Raman spectrum shows three broad peaks with maximum intensity at 327, 369, and 488 cm^{-1} which may indicate the presence of goethite, similar to the 45 °C sample. The shoulder peak at 680 cm^{-1} and the intense peak at 717 cm^{-1} are strong evidence of magnetite, while a broad peak at around 1400 cm^{-1} could be explained by the transformation of lepidocrocite (peak at 1307 cm^{-1}) into hematite, which has a characteristic peak at 1440 cm^{-1}.[105–109,109–111]

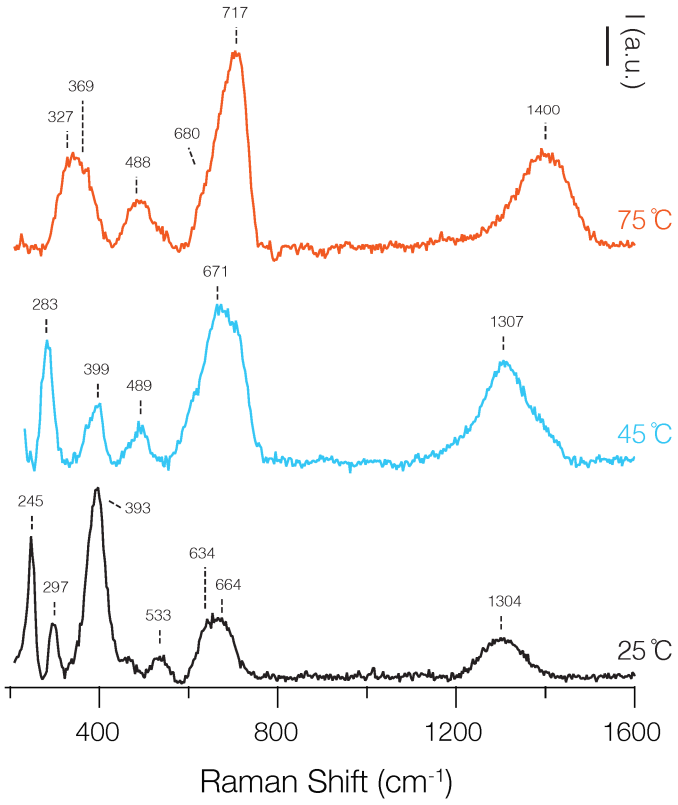

Figure 4-7 Raman spectrum of corrosion products after immersion of carbon steel coupons in seawater under low velocity of 0.15 m/s at 25˚C, 45˚C and 75 ˚C

Temp. (°C)	***Raman Peaks - Wavenumbers (cm^{-1})***												
25	245	297		354	393	459	533	634	674			1303	
45		283		376	399	489	599	671		717	1219	1307	1399
75			327	369		488	543	631	680	717	1295		1400

Table 4-2 Raman wavenumbers for each peak location in the fitted spectra of 25, 45, and 75 °C.

Furthermore, to quantify the ratio of oxidized (O^{2-}) to hydroxyl (OH^-) species at various temperatures, high-resolution XPS measurements of O 1s and Fe 2p regions are carried out. Figure 4-8 shows the high-resolution spectra of O 1s at temperatures ranging between 25 to 75 °C, and the presence of two peaks at 531.3 eV and 529.8 eV, which can

be assigned to hydroxyl species (OH^-) and oxidized species (O^{2-}) in the corrosion products, respectively [114–116]. In taking into account the XRD and Raman spectroscopy results, the XPS data suggests the presence of the following corrosion products, at all temperatures, on the surface of the samples at various ratios: lepidocrocite (γ-FeOOH), goethite (α-FeOOH), hematite (α-Fe_2O_3), magnetite (Fe_3O_4) [117]. Furthermore, at 25 °C the concentration of OH^- species appears to be higher relative to the concentration of O^{2-} species in the corrosion products formed. However, all temperatures above 25 °C showed higher concentrations of O^{2-} relative to OH^- with the ratio from (0.88 -1.13) to be the highest at 45 and 75 °C as shown in Table 4-3. This indicates that the degree of oxidation of the carbon steel surface increases with temperature, since the presence of O^{2-} increases, resulting in the formation of higher concentrations of α-Fe_2O_3, γ-Fe_2O_3, and Fe_3O_4 [114–117]. It is important to note that the O 1s spectra at 55 and 65 °C revealed the presence of a small shoulder peak at around 533 eV which can be attributed to physically adsorbed water (H_2O) [114–118]. Therefore, precautions were taken when quantitative analysis was performed to estimate the ratio of O^{2-}/OH^- at these temperatures, since the OH^- concentration could be a result of physically adsorbed H_2O, as well as FeOOH products. On the other side, the relatively high concentration of OH^- at 25 °C, without the presence of a shoulder peak at 533 eV, is primarily produced by the formation of γ-FeOOH or α-FeOOH. In the case of lepidocrocite, its concentration appears to be decreasing as temperature increases, since it is an intermediate corrosion product [114].

The results obtained by the Fe 2p XPS compliment the O 1s spectra revealing the presence of various Fe^{2+} and Fe^{3+} oxides, and maybe the presence of low concentration of hydroxides, as shown in Figure 4-9 [114–117]. The Fe 2p peak observed around 711 eV is in

accordance with the O 1s peak at about 529.8 eV validating the presence of hematite (α-Fe_2O_3) as well as magnetite (Fe_3O_4) at all temperatures [117]. Also, the binding energy of the Fe 2p peak at 719 eV further supports the presence of Fe_2O_3 corrosion products [115]. However, it is not possible to differentiate between hematite and maghemite solely from that peak.

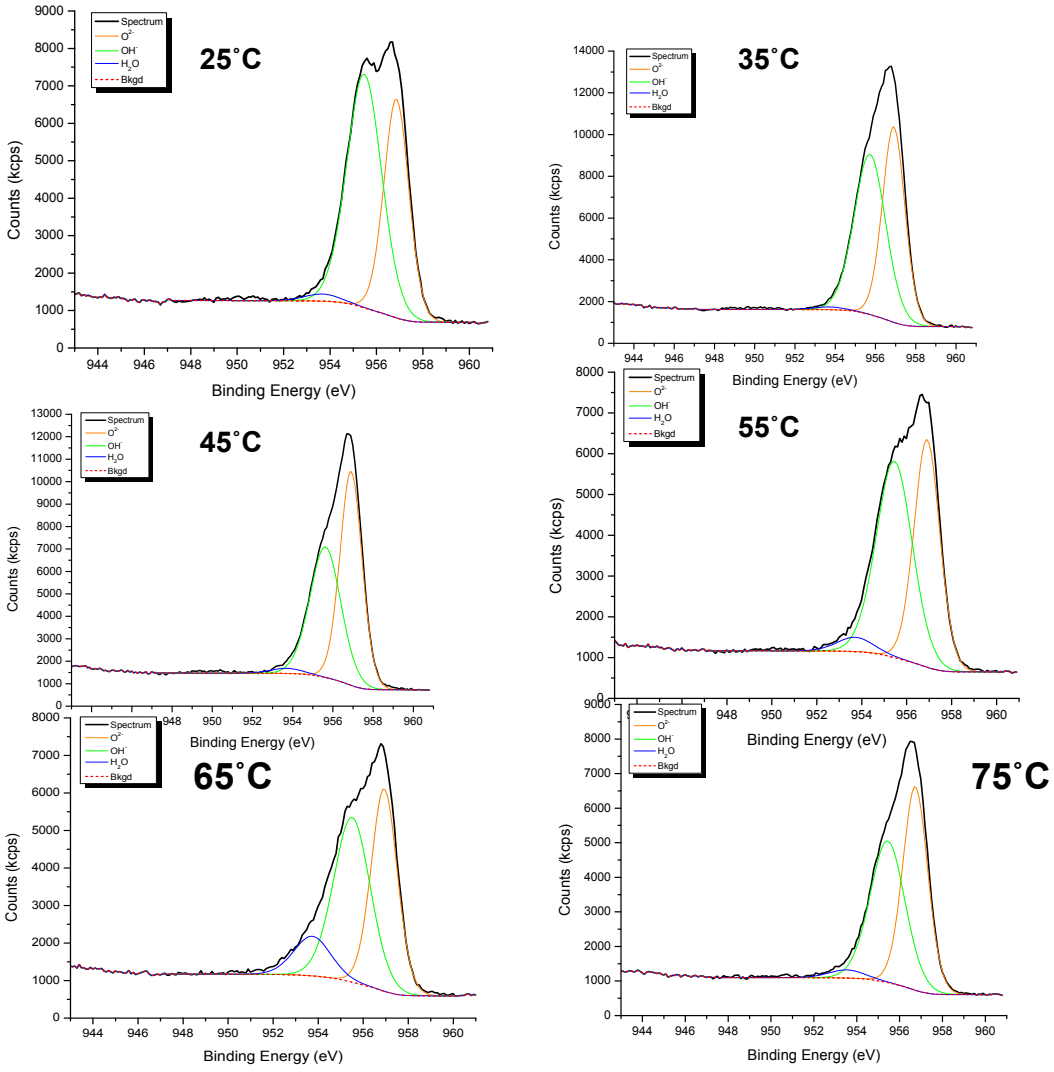

Figure 4-8 XPS spectra for O 1s region for the corrosion products on the carbon steel in seawater under low velocity of 0.15 m/s at various temperatures

Temperature (°C)	*Area Under O^{2-} (1/eV)*	*Area Under OH^- (1/eV)*	*Area Under H_2O (1/eV)*	*Ratio O^{2-} /OH^-*
25	8,054.63	12,038.63	366.77	**0.67**
35	8,218.03	9,916.42	721.37	**0.83**
45	13,456.02	15,441.27	257.27	**0.87**
55	8,061.32	9,181.38	2,210.37	**0.88**
65	13,437.37	11,491.08	453.51	**1.17**
75	8,786.39	8,551.34	494.16	**1.03**

Table 4-3 Deconvolution of O1s XPS spectrum at various temperatures and changes in the O^{2-}/OH^- ratio.

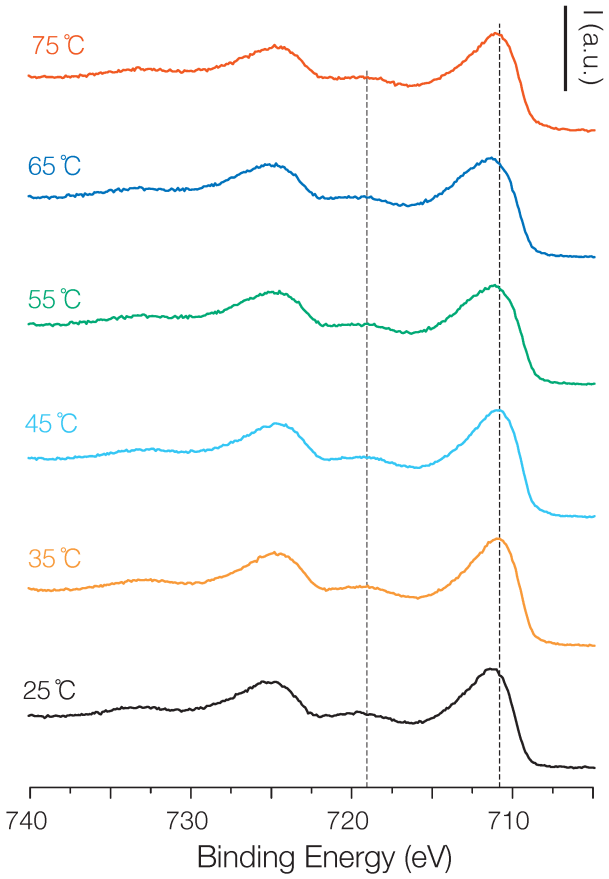

Figure 4-9 XPS spectra for Fe 2p/5 region in the corrosion products of the carbon steel under low velocity of 0.15 m/s at various temperatures

The combined results of XRD, Raman spectroscopy and XPS reveal the presence of lepidocrocite and goethite at 25 °C, and hematite is found as the main phase at 45 °C. The results of Raman agree with the XRD measurements, which show a notable presence of hematite in the corrosion products. In contrast, the existence of goethite is not seen in the observed area by XRD, even though the Raman results suggest its presence. This can be explained by the fact that goethite is in amorphous state, which has no XRD signal. Although XRD indicates that the corrosion products contain magnetite only at 75 ˚C, Raman spectroscopy results reveal the presence of magnetite and hematite.

The corrosion rate increases in multiple phases as the temperature increases. Below 35 °C the oxide formation is dominated by lepidocrocite. In the intermediate temperature range (35 °C and 45 °C), hematite is the predominant mineral form, which inhibits corrosion process. This can be explained by the fact that the oxygen diffusion through the corrosion layers can be affected by the crystal structures of the corrosion products. Hence, since the crystal and the chemical compositions of the products change as a function of temperature, one would expect the oxygen diffusion to change accordingly. Since γ-iron (III) oxide hydroxide (lepidocrocite) is thermodynamically unstable, electrochemically active and works as cathodic site, it transforms to -iron (III) oxide (hematite) at 45 °C in seawater. Furthermore, as mentioned earlier, the crystal structure of lepidocrocite is orthorhombic[80].Anion sheets are parallel to plane (0 4 1) are stacked along the direction parallel to the direction [012] as shown Figure 4-10.

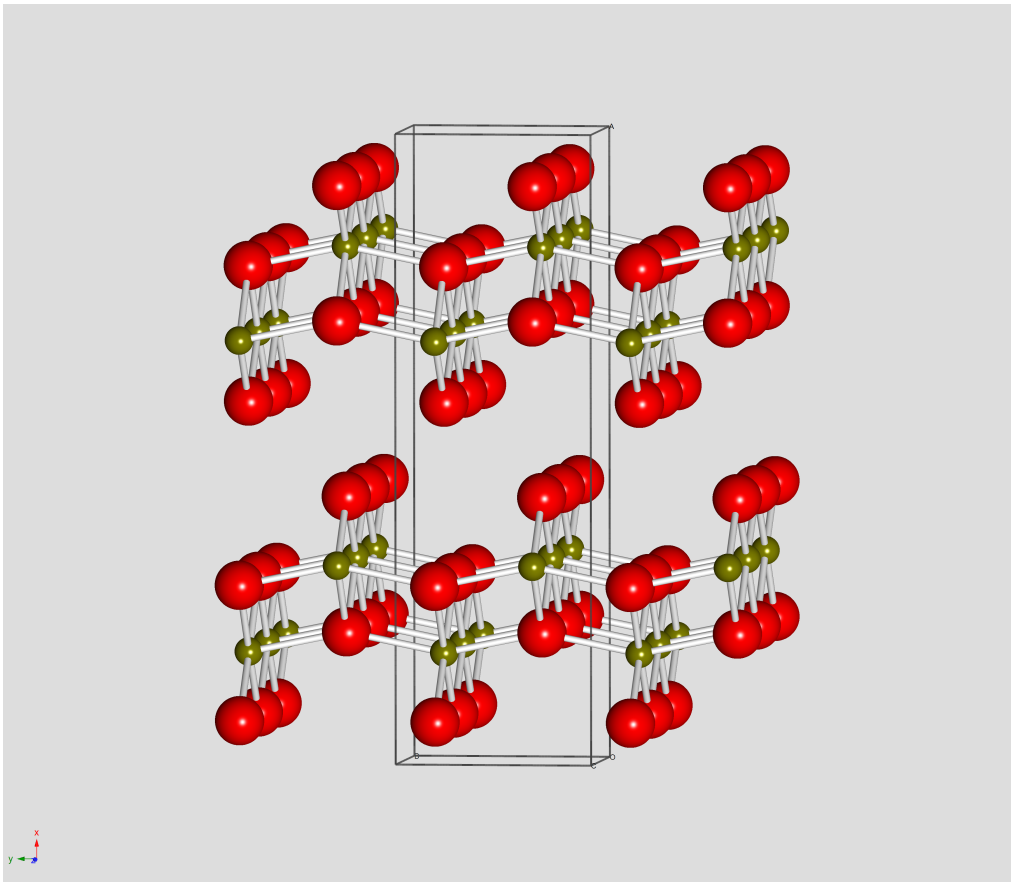

Figure 4-10 Packing of lepidocrocite unit cells

While hematite is the most thermodynamically stable form of iron oxides with standard free energy formation (ΔG_f = -742 kJ/mol) compared with lepidocrocite (ΔG_f = -480 kJ/mol) [69]. The crystal structure of hematite is isostructural with corundum [69]. The oxygen ions are in hexagonal closed-packed (hcp) arrangement that stacked along the [001] direction with Fe (III) ions occupying octahedral sites as shown in Figure 4-11 . The structure has low concentration of structural defects, which leads to decrease in the grain boundaries. Consequently, the oxygen diffusion decreases, and the corrosion is ultimately hindered. Furthermore, Raman reveals goethite presence in 45 °C, which is considered as protective layer that impedes the corrosion rate.

As the temperature increases further more to 55-65 ˚C, the corrosion products become powdery and easily removed by the agitation as shown in Figure 4-1. Consequently, the carbon steel surface is exposed to the seawater again, and the corrosion rate eventually increases between 55˚C- 75˚C.

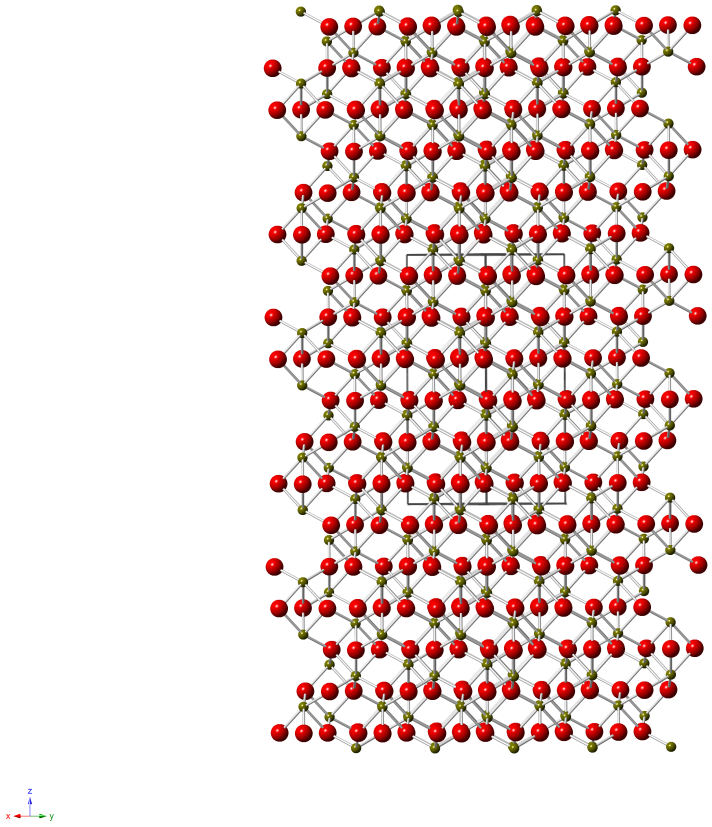

Figure 4-11 Packing of hematite unit cells

4.1.5 The absence of Iron carbonate in the corrosion products

Under our experimental conditions where the $[CO_3^{2-}]$ in seawater 0.000239 kg mol^{-1} ,the XRD results do not show the formation of the FeC_3 (cementite).

The concentration of carbonate in seawater is very low about 0.000239 kg mol^{-1}. The presence of carbonate promotes the formation of $FeCO_3$ according to the following reaction[119]:

$$Fe^{2+} + CO_3^{2-} \rightarrow FeCO_3 \qquad \textbf{Equation 4-1}$$

Many studies showed that $FeCO_3$ (siderite) is formed in solutions with high concentration of carbonate[119]. However, in our experiment we have used natural seawater with a low concentration of carbonate, as such the corrosion product of carbon steel does not consist of siderite or cementite. However, the XRD results reveal small peaks that it could be trace amount of siderite.

4.1.6 The absence of green complex or green rust

Under our experimental conditions, where seawater was used, no green rust was observed, even at the early stages of the corrosion, at temperature range of 25˚C- 75˚C, and at pH~8.3. Also our XRD results confirmed the absence of the green rust at various conditions and corrosion periods. This is in contrary to the most published results of the carbon steel corrosion under aerated conditions. It has been reported that green rust forms on the carbon steel in the aerated area as an intermediate, which then transforms either to Fe_3O_4 under slow oxidation or γ-FeOOH under rapid oxidation[73]. Also, this transformation depends mainly on the pH. Schwertmann observed the transformation of the green rust to lepidocrocite at constant pH ~7 and aerated conditions[74]. Likewise, a study shows that green rust forms from the oxidation of Fe^{2+} or $Fe(OH)_2$ oxides by oxygen in aqueous solution at pH 7[59]. While, at pH above 7, green rust transforms rapidly to magnetite[120]. In addition, many studies show that the green rust forms as predominant

mineral in environments such as reductomorphic soils, groundwater and microbial culture[121–123].

Our experiments have been performed at pH 8.3 (the pH value for natural seawater) and this pH value could explain the absence of green rust in the corrosion products and the presence of magnetite with small amount of carbon steel in seawater. The green rust could be formed in the surface of carbon steel at the first few minutes of the immersion in seawater as intermediate. This intermediate would then spontaneously transform to magnetite.

4.1.6.1 The correlation between the chemical structures of the corrosion products and the number of pits per unit area

The cross sectional analysis shows different sizes and shapes of cracks and pits on the surface of the carbon steel immersed in seawater at various temperatures. As shown in Table 4-4, the number of cracks and pits are very high at 25 and 35 ˚C compared with other temperatures. As mentioned above, the corrosion products at low temperatures are unproductive, pores that can easily flake off the surface. In addition the chloride ions have the ability to break these passive layers[21].This can lead to the diffusion of the corrosive ions, such as the chloride ion, onto the metal surface. In contrast, at high temperatures, the corrosion products adhere to the metal surface, and form a barrier for the chloride ion. Figure 4-12 shows the pits and the cracks on the surface of the carbon

steel, where the sizes and the number of pits and cracks are decrease with increasing temperature.

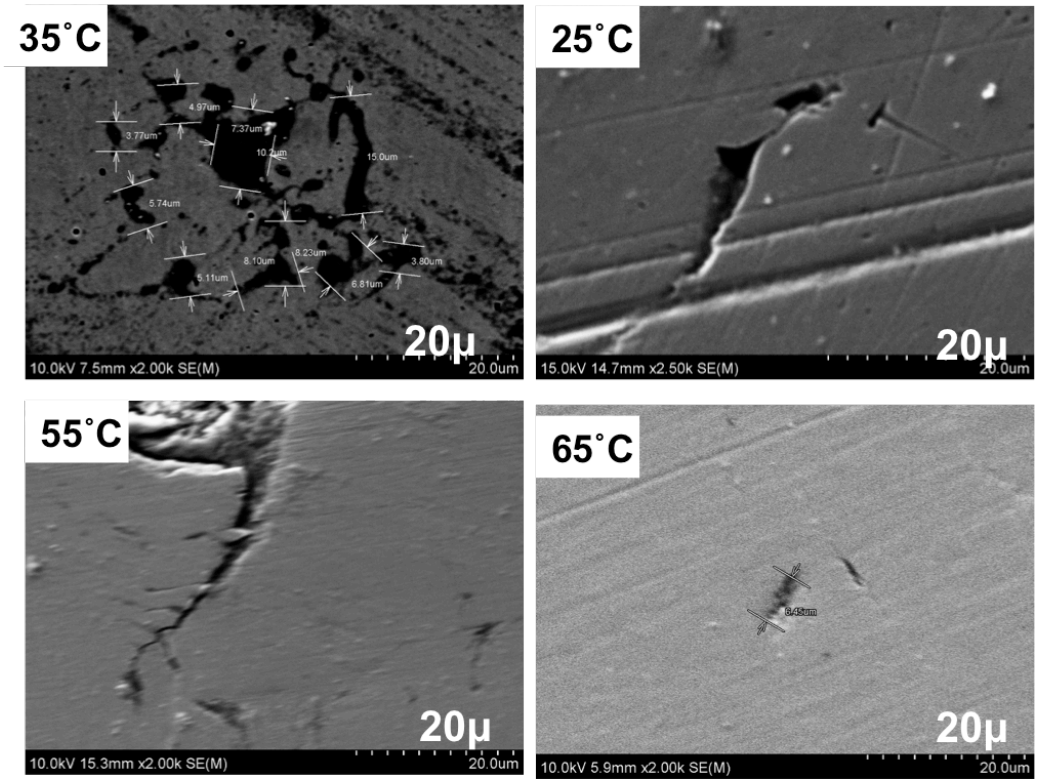

Figure 4-12 Cross sectional of carbon steel immersed in seawater under low flow rate at various temperatures

Temperature (˚C)	*No. of pits*	*Pit's length (µm)*
25	40	6.33 ± 1.3
35	19	11.47 ± 2.1
45	4	8.6 ± 1.33
55	4	10 ± 0.6
65	4	25.5 ± 14

Table 4-4 cracks measurements on carbon steel immersed in seawater with low velocity of 0.15 m/s at various temperatures

4.2 Simulation of the corrosion process in the crude oil pipelines

As mentioned in the experimental section, a stainless steel loop was constructed to simulate the conditions of actual crude oil pipelines in terms of flow rates and temperatures. The objective of these experiments is to study the seawater-induced corrosion in the carbon steel at high flow rates combined with the temperature effect. It is important to study the effect of temperature at high flow rates since the temperature changes dramatically from day to night, and from season to season in the oil fields. In order to estimate the corrosion rates at various temperatures at high flow rates, the overall activation energy was determined. Equally important is to investigate at which temperature erosion corrosion takes place. Another factor is that the crude oil in the pipeline contains seawater most of the time. The seawater is usually a major component of the produced water. In some cases, the produced water component reaches up to 30% depending on the condition of the oil field.

The experiments were performed starting with inserting the carbon steel coupons inside the loop. The loop is operated at a flow rate of 192 ± 3 gal/min (flow velocity 2.7 m/s) of seawater at various temperatures. The loop with coupons mounted in the horizontal test section is shown in Figure 3-3-3. For all experiments, the coupons were placed in the flow loop for seven days. This period of seven days was chosen to keep as much as possible the corrosion products on the coupon's surface. If the experiment were continued for more than seven days, most of the corrosion products would leach out from the coupon's surface to the liquid phase. In fact, at 75˚C for seven days in the loop at 192 gal/min, the small-size coupons would completely disappear.

4.2.1 Determination of the corrosion rates at various temperatures

The corrosion rate of the carbon steel for various temperatures at a flow rate 192 gal/min for seven days were determined gravimetrically as follows:

4.2.1.1 Gravimetric method

After placing the coupons in the flow loop for seven days, they were cleaned following the ASTM cleaning procedures[95]. The weight difference after seven days was used to determine the corrosion rate as described in Equation 3-3-1. Figure 4-13 shows that the corrosion rate of the carbon steel increases linearly with increasing temperatures from 25 ˚C to 35 ˚C. However, the student T.Test showed that there were no significant changes in the corrosion rates between 35 ˚C and 45˚C due to the transformation of the corrosion products at 45˚C. As discussed in section 4.1.1, the same results were observed where there is no change in the corrosion rates between 35˚C and 45˚C during the low rotation speed in the stirrer beaker experiments. This strongly suggests that there is no flow rate effect on the corrosion rate between 35˚C and 45˚C. This important observation will be discussed in detail in section 4.3.3. Moreover, the corrosion rate increases exponentially between 55˚C and 75˚C.This sharp increase between 45 ˚C and 75 ˚C may be related to erosion-corrosion since experiments were conducted at a flow rate of 192 gal/min. The complication of this system, at a high flow rate, stems from the fact that both cathodic and anodic reactions increase, but not necessarily at the same rate. The high flow rate enhances the transport of dissolved oxygen (and other corrosive species such as chloride ions) from the aqueous phase toward the metal surface, which enhances the

cathodic reaction. In addition, high flow rates also increase the charge transfer reaction, which leads to the domination of the anodic reaction[18]. Also, the high flow rate enhances erosion-corrosion, which ultimately removes all the contacted and adhered corrosion products away from the metal surface. Needless to say, this will increase the exposure of the metal surface to the water, and accelerate the corrosion process.

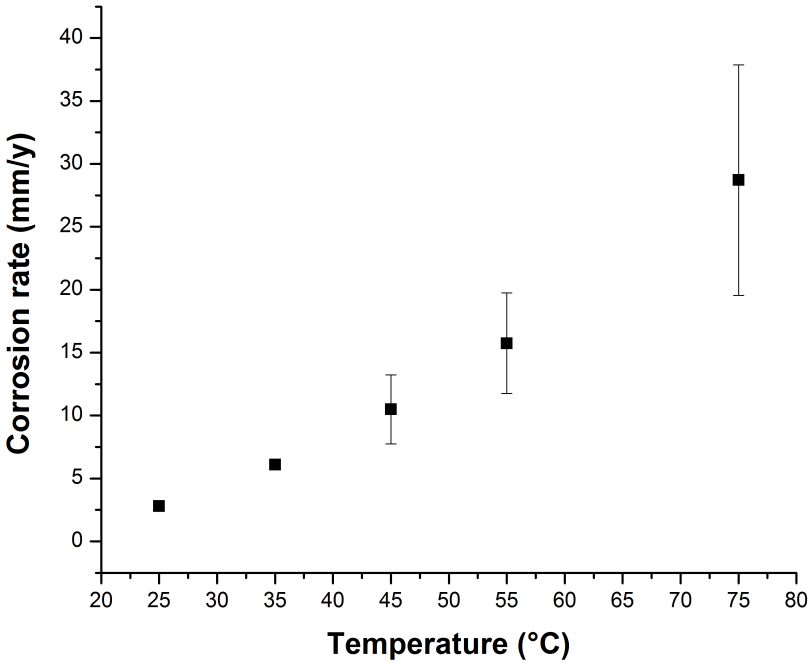

Figure 4-13 Corrosion rate of carbon steel inserted inside the flow loop with high flow rate (192 gal/min) as a function of temperature

4.2.2 The observed-overall activation energy at high flow rate

The objective of these measurements is to investigate the effect of the flow rate on the overall activation energy. The activation energy of the corrosion process was determined by mass loss rates and current density using the Arrhenius equation.

$$Ln\ Cr\ \left(\frac{mg}{cm^2.hr}\right) = A\ exp\frac{-E_a}{RT} \qquad \textbf{Equation 4-2}$$

Figure 4-15 shows that at low temperatures, the mass loss as a function of flow rate follows an Arrhenius exponential relationship, with an activation energy value of 54.8 kJ/ mole. At temperatures higher than 45 ˚C, the corrosion started to deviate from the Arrhenius function. This is because the erosion corrosion has started to predominate. It was visually confirmed that the corrosion products were eroded moving away from the surface to the water, and changing the water from colorless to a blackish color. In addition, as shown in Figure 4-14, the coupons were completely eroded at 75 °C. Obviously, the increase in temperature does not only increase the reaction rate, but also increases the oxygen diffusion throughout the corrosion layers. Hence, the increase in temperature enhances the mass transfer-induced cathodic corrosion. So, in summary, the observed activation energy is a combination of mass transfer and erosion corrosion.

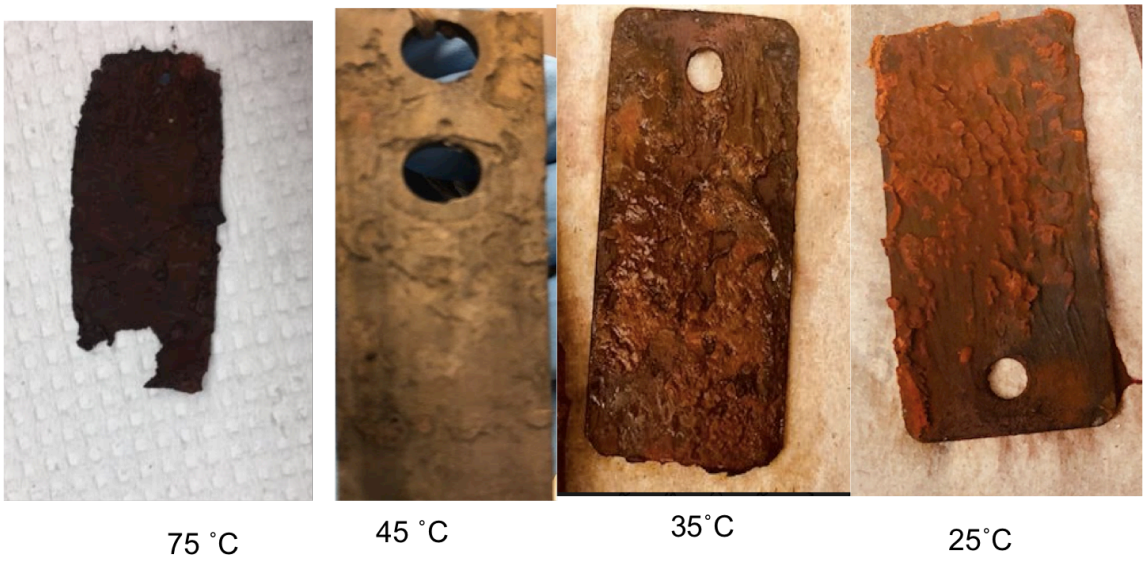

Figure 4-14 Visual examination of the carbon steel coupons after insertion in flow loop for seven days with high flow rate (192 gal/min)

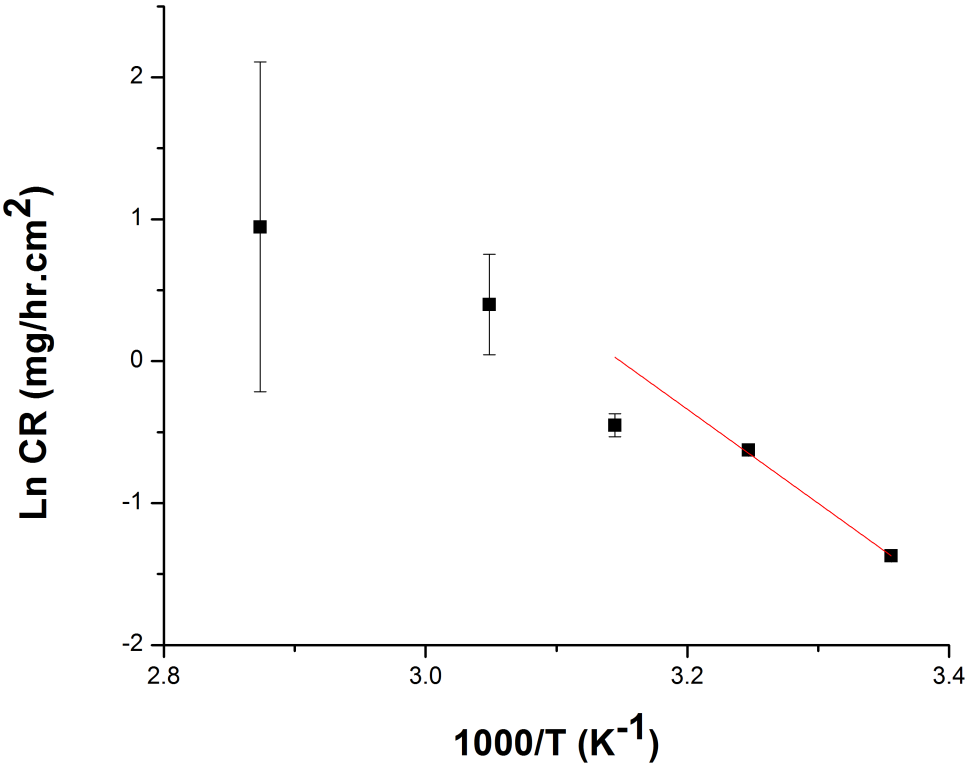

Figure 4-15 Arrhenius plot of carbon steel inside the flow loop with high flow rate of 192 gal/min

Activation energy in terms of current density:

The observed activation energy also can be determined in terms of the current density that was obtained from the linear polarization using Equation 4-3. However, this approach is not quite accurate for the following reason. During the polarization experiment, large amounts of current flows to the metal, which leads to a sudden drop in the concentration polarization, and ultimately misrepresent the polarization curve. Therefore, it is expected that considerable error would be introduced in determining the activation energy using the current density, due to the uncertainty in the i_{corr} values[124].

$$Ln\ i(\mu A/cm^2) = A \exp \frac{-E_a}{RT} \qquad \text{Equation 4-3}$$

4.2.2.1 The velocity effects on the overall activation energy

In this work, it has been shown that the overall activation energy obtained from stirred beaker-low angular velocity of 0.15 m/s (60 rpm) experiments is 12.7 kJ/mole, and the overall activation energy obtained from the loop experiments at a flow rate of 2.7 m/s (192 gal/min) is 54.8 kJ/mole. This significant difference in the observed-measured activation energy is not unusual. It has been reported that, in general, as the flow rate increases, the overall activation energy increases[125].

In order to understand the mechanism of the flow rate effect on the activation energy, one must take into account the effect of the flow rate on the corrosion rate. It is

very well known that mass controlled processes depend strongly on the aqueous phase flow rate and agitation. On the contrary, charge transfer controlled processes are usually independent of the aqueous phase flow rate and agitation. It should also be mentioned that the corrosion rate of clean metals and alloys in neutral or slightly basic solutions, such as seawater (pH ~ 8.2-8.3) is usually determined by mass transport control of the cathodic reaction. It is also crucial for this work to determine the activation energy of corrosion under similar conditions to that of the carbon steel crude oil pipelines in the fields, where the flow rate is as high as 2.7 m/s (192 gal/min).

In reviewing the overall changes of the corrosion rate dependency on the flow rate, the following factors must be taken into account:

1. The strong dependency of the diffusion-controlled processes and the diffusion boundary layer thickness on the flow rate.

Since the diffusion-controlled process is directly related to the following cathodic reaction:

$$\mathbf{O_2 + 2H_2O + e^- \rightarrow 4OH^-} \qquad \textbf{Equation 4-4}$$

It is therefore reasonable to predict that as the flow rate increases the supply of oxygen from the aqueous bulk solution to the reacting interface is enhanced, and ultimately enhances the corrosion rate. The increase in the corrosion rate as a function of flow rate will continue to increase until the anodic charge transfer control is established. After establishing the anodic-controlled reaction, the corrosion rate reaches a plateau. It is also worth mentioning that in most realistic corrosion situations, where oxygen is

involved, the cathodic reaction itself is influenced by both "mixed" charge transfer-controlled and mass transfer- controlled. Figure 4-16 shows the dependency of the corrosion rate on the electrolyte flow rate[4]. While at relatively low flow rate, the corrosion rate is diffusion-controlled, but as the flow rate increases the corrosion rate becomes activation controlled.

2. The dependency of the activation controlled on the flow rate

The reasons for the effect of the flow rate on the measured activation energy can be outlined as follows:

A: Activation polarization: The activation polarization is caused by the resistance against the reaction at the metal-aqueous phase interface. In order for the ions or molecules to convert to a new state, or to other species at the interface, they need to overcome the energy barrier of the rate-determining step. The rate determining step in this case is the charge transfer[4].

B: Concentration Polarization: This type of polarization occurs when the electrode reactions cause both mass and charge transfer at the metal-aqueous surface, and the transport of the ions and molecules in the solution to and from the interface. In this case the rate determining step is the mass transport[4].

3. The effects of the evolved erosion corrosion at high flow rate

The high flow rate induces erosion corrosion, which continuously leads to the exposure of the bare surface of the metals. It has also been shown that the corrosion rates of the steel in seawater increase as the velocity increases [4].

A significant increase in the erosion corrosion was observed only at 75 ^{o}C. Since erosion corrosion is greatly enhanced by the turbulent flow, it is imperative to determine the Reynolds number. Re is calculated for the flow loop at 25˚C and 75˚C as following:

$$\boldsymbol{Re = \frac{u_p d_p}{\upsilon}} \qquad \textbf{Equation 4-5}$$

Where u_p is the flow velocity (m/s), d_p is the pipe diameter (m), and υ is the kinematic viscosity (m^2/s) ($9.37x10^{-7}$ at 25˚C) and ($3.85\ x10^{-7}$ at 75˚C)[126].

It has been found that Re is $2x10^5$ at 25˚C and $5.3x10^5$ at 75˚C. From these Reynolds numbers, it is determined that the flow was under transition from laminar to turbulent at 25 C, however, the flow was fully turbulent at 75˚C[127]. Therefore, erosion corrosion has significant impact at 75˚C.

Figure 4-16 from reference 4, shows at a lower velocity the corrosion is diffusion controlled, however at a higher velocity the corrosion is activation controlled[4]. At a lower velocity, the cathodic reaction is under mass transfer control, and the anodic reaction is always charge transfer controlled.

$$\mathbf{M \rightarrow M^+ + e^-} \qquad \textbf{Equation 4-6}$$

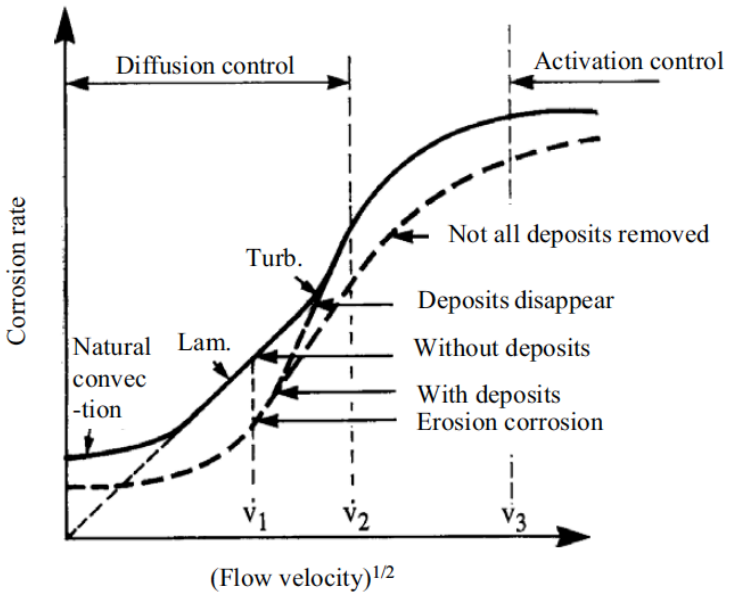

Figure 4-16 [4] The corrosion rate as function of (velocity)$^{1/2}$ (Figure was copied from "Corrosion and protection" book)

In this work, low velocity experiments were performed in a stirred beaker at 60 rpm (0.15 m/s), where agitation was used. There is no significant change in the ingredient concentration of the dissolved active species such as O_2 and Cl^{-1} as a function of the distance from the metal surface. In other words, the diffusion-boundary layer is almost non-existent. The agitation in these experiments keeps the uniformity of the dissolved species almost constant, and prevents the formation of the diffusion boundary layer in the first place. Therefore, for the cathodic reaction, where the rate-determining step is mass transport, the activation energy barrier is low. Hence, it is expected that low activation energy would be obtained. However, the loop experiments were conducted at a very high flow velocity (2.7 m/s). The formation of the diffusion boundary layer is expected to occur with a relatively high thickness [128]. This means that the mass transport

of O_2 and Cl^{-1} requires more energy. Thus, higher activation energy in the loop experiments, compared to that in the stirred beaker's experiments, is expected.

4.2.3 The use of polarization resistance and Tafel plot to further determine the role of the corrective layers at high flow rate of 192gal/min

These series of experiments were conducted to generally identify the changes in the corrosion products as a function of temperature based on the changes in βa, βc, icorr, and Rp. Despite the fact that theses experiments were conducted once due to the complexity of the procedure is still they shade the light on the trend of the changes in the βa, βc, icorr, and Rp. In other word, these experiments were not meant to get the exact values of βa, βc, icorr, and Rp, but rather the general temperature effects on their values.

The polarization curves of carbon steel coupons after were placed inside the flow loop with seawater are shown in Figure 4-17. The anodic and cathodic branches were extrapolated to the intersection at a point where the corrosion current density i_{corr} and E_{cor} were obtained. This procedure was discussed in section 3.2.1.2. The polarization curves of the corroded carbon steel showed that the corrosion potential (E_{corr}) shifted to positive values at 45 ˚C. This indicates that the formation of protective layers on the surface of the carbon steel is occurring[120,121]. The shapes of the anodic and the cathodic reactions were also changed with increasing the temperature. This change indicates that the corrosion products have an impact on the anodic and cathodic reactions rates. Nevertheless, as expected, the anodic reaction rates were higher than the cathodic, which means that the

corrosion process inside the flow loop is anodically-controlled[4].The anodic reaction is an iron dissolution as shown below:

$$Fe \rightarrow Fe^{2+} + 2e$$ **Equation 4-7 (the anodic reaction)**

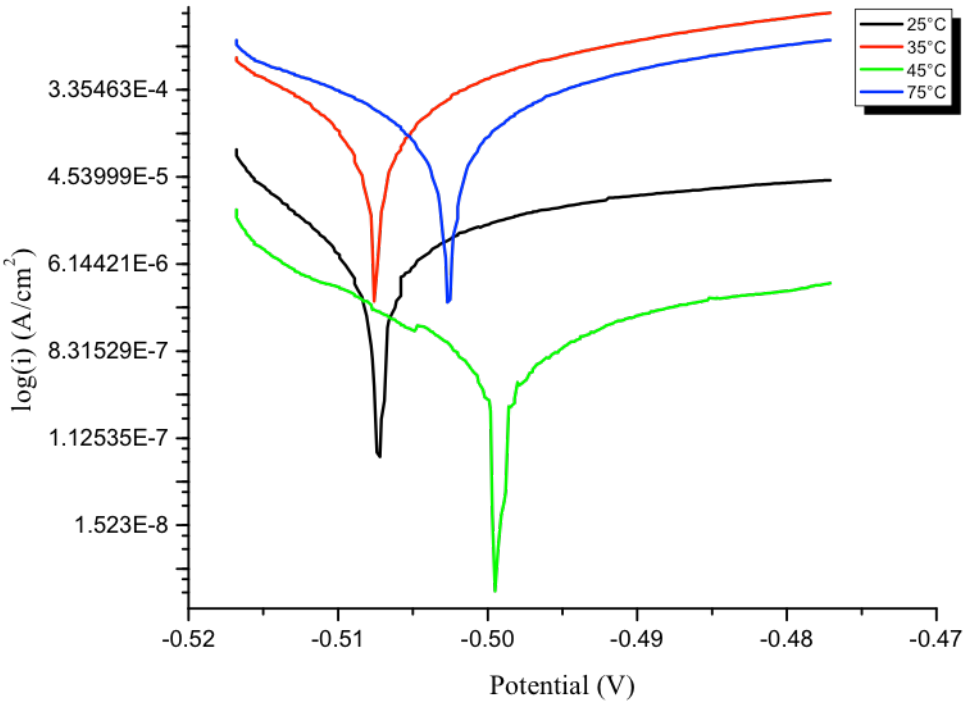

Figure 4-17 Tafel plot of corroded carbon steel inside a seawater flow loop with high flow rates (192 gal/min) at various temperatures

The results of Tafel and LPR measurements of the corroded carbon steel exposed to the seawater in the flow loop are summarized in Table 4-5. Since the purpose of these measurements is to determine the Tafel constants (β_a, β_c), corrosion current, and polarization resistance in the presence of different forms of corrosion products, no cleaning producers were conducted on the surface after removing coupons from the loop[122]. In fact, extra precautions were made to ensure that the corrosion products stayed

on the surface during the transportation from the loop to the corrosion cell. To establish base-line results, Tafel constants (β_a, β_c), corrosion current, and polarization resistance were conducted on very clean carbon steel coupons (not previously exposed to seawater). These measurements on the clean samples were carried out using the same corrosion cell with seawater as electrolyte at 25˚C.

For the coupons were exposed to seawater at 25 ˚C, β_a was found to be higher than β_c, which indicates that the corrosion is anodically controlled. While the β_a values of the corrosion product and the bare coupon at 25 ˚C, are practically the same (β_a 46.9 mV per decade, and 48.46 mV per decade, respectively), however, β_c value of (16.2 mV per decade) decreases comparing to the bare coupon (β_c= 121 mV per decade). This significant decease in the β_c strongly suggests that the formation of the corrosion product at 25 ˚C indicates that the corrosion products are cathodic- induced reaction. As it discussed in section 4.2.4, the formed corrosion layers at 25 ˚C are mainly composed of lepidocrocite (γ-FeOOH). Since no significant changes were observed in β_a between the corroded and bare coupon at 25 ˚C, this also suggested that lepidocrocite is a cathodic-induced compound.

At 35˚C, the cathodic Tafel constant increases comparing with the corroded coupon at 25˚C indicating the increase of the cathodic reaction in the presence of γ-FeOOH and Fe_2O_3. As it discussed in section 4.2.4, the corrosion products at 35˚C are lepidocrocite (γ-FeOOH) and magnetite (Fe_2O_3). This form of iron oxide hydroxide (FeOOH) preforms as cathode[132]. So, therefore, it is expected that the cathodic reaction increase. In Figure 4-17, the polarization curves at 25˚C and 35˚C have almost the same shape. At 45˚C, β_a is higher that β_c suggesting that the corrosion products at 45˚C

(hematite) has influenced on both cathodic and anodic reactions[131]. β_c (16. 9 mV per decade) decreases sharply comparing with bare coupon. This can be explained by the fact of the formation of the protective layers (hematite) can decrease the cathodic reaction. β_a also decreases at 45˚C (32.9 mV per decade) demonstrating the negative effect of the formed hematite as a protection layer. The effects of the protective layer (hematite) was also demonstrated in Figure 4-17, whereby the corrosion potential shifted to the positive values at 45˚C and higher indicating that the driving force of the corrosion in the presence of the protective layers (hematite) is decreased[133].

It is indeed very interesting that at 75˚C, no corrosion products have found on the surface due to the erosion corrosion. However, the eroded surface has impact on the electrochemical surface. By comparing the results at 75˚C to the bare coupon, it found that the anodic reaction increases, while the cathodic reaction decreases.

Table 4-5 also shows the corrosion current density (i_{corr}) at 25-75 ^{o}C, which relates to the corrosion rate as shown in the equation below:

$$\textbf{Corr. rate (mpy)} = \frac{\mathbf{0.3}\, I_{corr}(E.W)}{d} \qquad \textbf{Equation 4-8}$$

At 25˚C, i_{corr} of the corroded coupon with γ-FeOOH is lower than the bare coupon. This result can be explained by the fact that as the bare coupons are being measured in the corrosion cell, they are immersed in seawater. So, the observed corrosion current density of the base coupon is directly related to very beginning steps of the corrosion, which they are faster than when the corrosion layers have already formed like in the case of corroded samples at 25˚C. Also as noted in Table 1, i_{corr} in the presence of γ-FeOOH, at 25^{o}C, is higher than i_{corr} in the presence of other corrosion products present

at other temperature. This is another evidence demonstrating that lepidocrocite (γ-FeOOH), which is the main component of the corrosion layer, induces the cathodic reaction, and ultimately enhances the i_{corr}. Again, it can also be seen that i_{corr} decrease sharply at 45 ˚C due to the formation of protective layers (hematite) on the surface of the carbon steel. As stated earlier, at 75 ˚C, the surface of the coupons was eroded and no corrosion products were found on the surface. The current density of these coupons increased sharply to a value of i_{corr}= 477 μA/ cm^2. This value is even much higher than the bare coupon of. (i_{corr}= 39.3 μA/ cm^2). It is very clear from these results the erosion-corrosion has significant impact on the surface chemical composition and morphology.

Table 4-5 also shows that the polarization resistance (R_p) is increased sharply from 0.248 kΩ at 25 ˚C to 2.94 kΩ at 45 ˚C. It is indeed expected to observe such sharp increase, since between 35˚C and 45 ˚C, the protective, hematite, is the main corrosion product [134]. The resistance decreased precipitately at 75 ˚C with the value of 0.0186 kΩ. This value is even lower than 0.379 kΩ of the bare coupon. As noted earlier, this may be related to the fact that formation of the corrosion products on the bare coupon during the analysis, where they are immersed in the seawater, induced an increase in the resistance.

Temperature (˚C)	β_a mV/decade	β_c mV/decade	i_{corr} µA/cm^2	R_p (kΩ)
25	46.9	16.2	22.2	0.248
35	58.9	51.5	12	0.91
45	32.9	16.9	1.6	2.94
55				
75	75.7	26.9	477	0.0186
Bare clean coupon (not previously exposed to seawater)	48.46	121.3	39.3	0.379

Table 4-5 The cathodic and anodic Tafel constants, corrosion current and polarization resistance of the corroded carbon steel (exposed to seaware for 7 days in the loop with 192 gal/min). The measurements were taken at ± 200mv form the corrosion potential

4.2.4 The surface morphology of corroded carbon steel in the flow loop

4.2.4.1 Visual inspection

The color of the corrosion products changes as the temperature increases. As shown in Figure 4-14, the corrosion products were orange at 25˚C, and then changed gradually to black at 75˚C. These color changes indicate the formation of different iron oxides forms with increasing temperature. The orange color indicates the presence of lepidocrocite. At 45 ˚C, the coupons were covered with orange-yellow corrosion products, which imply the presence of goethite. Ultimately, the coupons were covered with black layers due to the formation of magnetite.

4.2.4.2 The surface morphology of the corrosion products

The morphologies of the corrosion products on the surface of carbon steel were examined using SEM-EDS. As the temperature increases, the morphology of the corroded carbon steel evolved as shown in Figure 4-18. The corrosion products at 25˚C and 35 ˚C are

porous and powdery looking, while at 45˚C and 75 ˚ the corrosion products are compact and adhere to the surface. Moreover, SEM revealed the presence of cracks on the surface at 75˚C. The protectiveness of these corrosion products toward corrosion depends on the adherence or porosity, where the most adherent layer acts as a barrier to impede the corrosion[135].Under high magnification, Figure 4-19 shows that fine plates (flowery structure) and crystalline globule (sandy crystal) structures dominate at 25 ˚C, which are the typical lepidocrocite (γ-FeOOH) structures[32,101,135]. A similar morphology to the one at 25 ˚C is observed on the surface of carbon steel at 35˚C with the exception of the presence of pseudo-cubic morphology. This type of morphology is related to magnetite[104,136]. On the other hand, the corrosion morphology at 45˚C was a mixture of different shapes, consisting of cotton ball shapes, plates, spindles, and pseudo-cubes. This variety of shapes suggests the formation of goethite (cotton ball), hematite (spindle) and magnetite (pseudo-cubes)[32,101,104,105]. The surface morphology at 75˚C has dark spots and clusters of globules with a semi-cubical structure. These structures are related to the presence of magnetite[32,101].

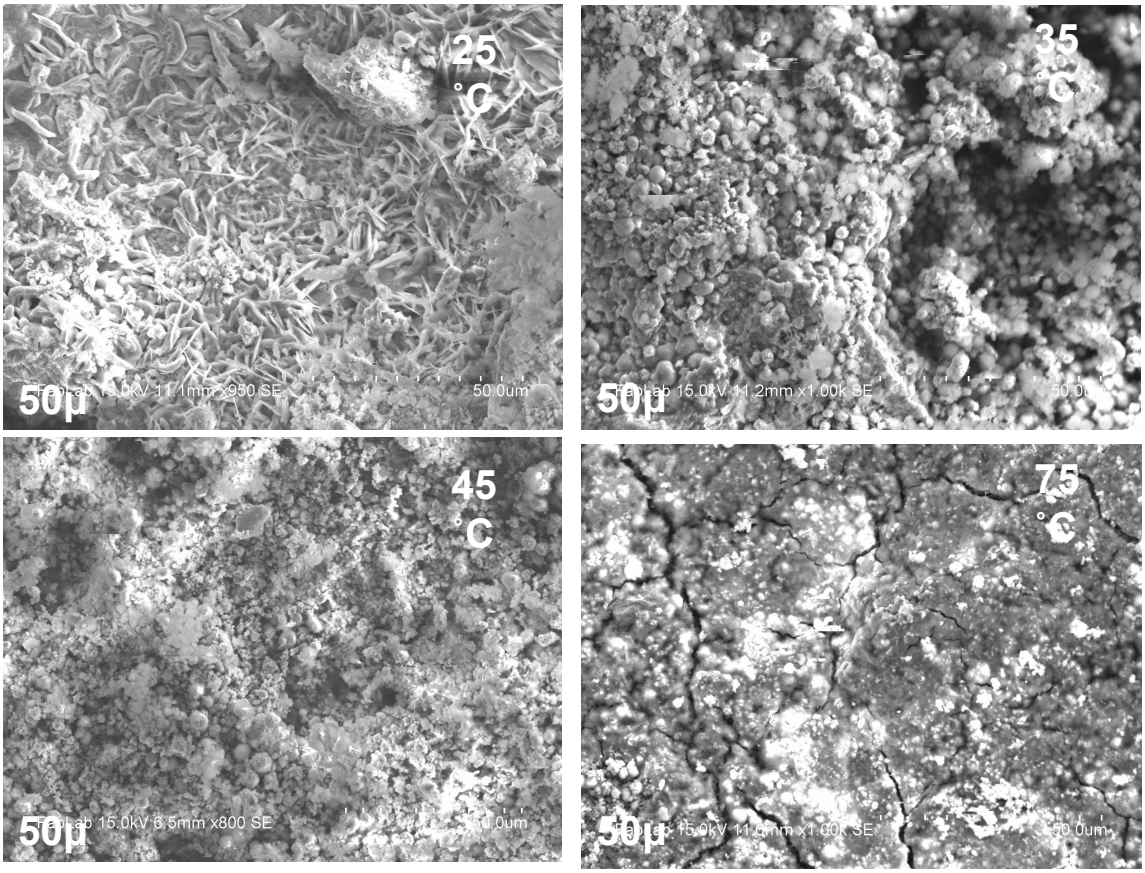

Figure 4-18 Surface morphologies with low magnification images of the carbon steel inserted inside the flow loop with high flow rate (192 gal/min) at various temperatures

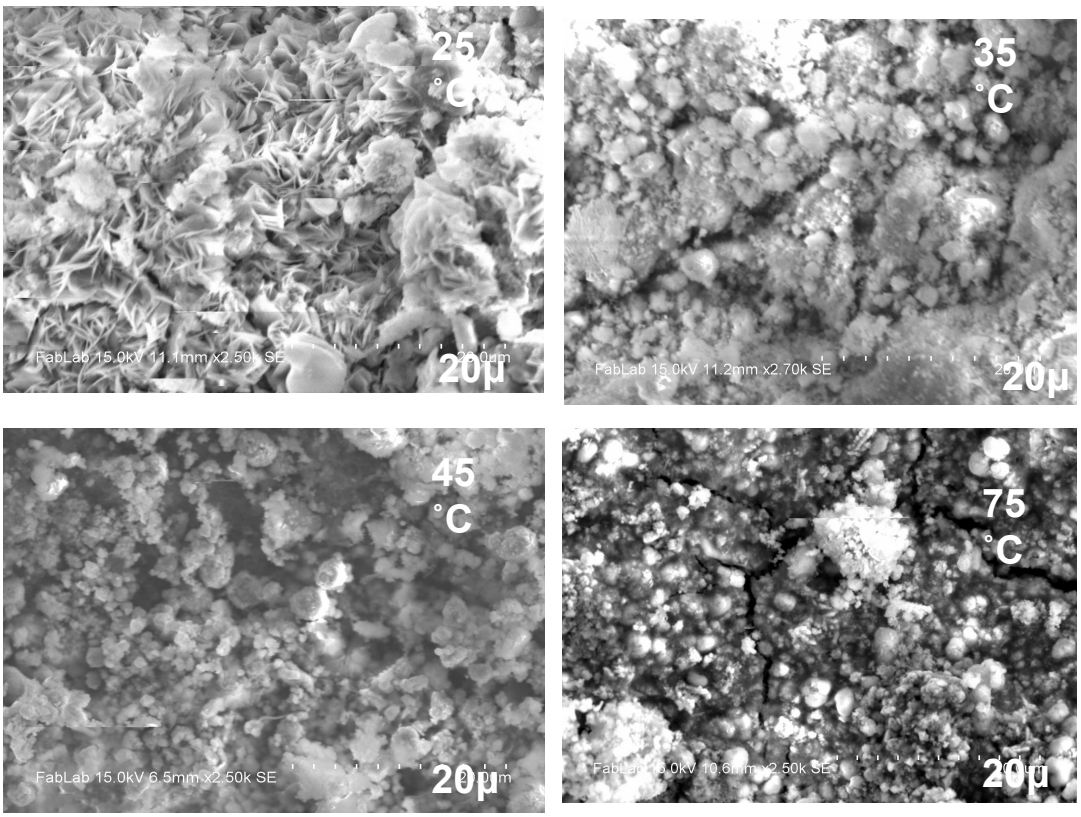

Figure 4-19 The surface morphology with high magnification images of the corrosion product on the carbon steel inserted inside a flow loop with high flow rate (192 gal/min) at various temperatures

4.2.5 Characterization of Corrosion Products Using XRD

To study the crystal structure of corrosion products on the surface of carbon steel, XRD analyses were performed. The XRD patterns revealed the change of crystal structures with increasing temperature. As shown in Figure 4-20, the main constituent at 25 ˚C is lepidocrocite (γ-FeOOH) with orthorhombic structures. At 35˚C, the corrosion product structures are 58.4 ± 4.5 orthorhombic (lepidocrocite) and 41.6 ±4.5 cubic.(magnetite). However, the corrosion products at 45 ˚C are mainly composed of

69.5 ± 4.1 hexagonal goethite (α-FeOOH), 17.4 ± 2.5 rhombohedral hematite (α-Fe_2O_3) and 13.1± 1.57 cubic magnetite (Fe_3O_4). Finally, XRD reveals that the corrosion products at 75 ˚C are 100% magnetite.

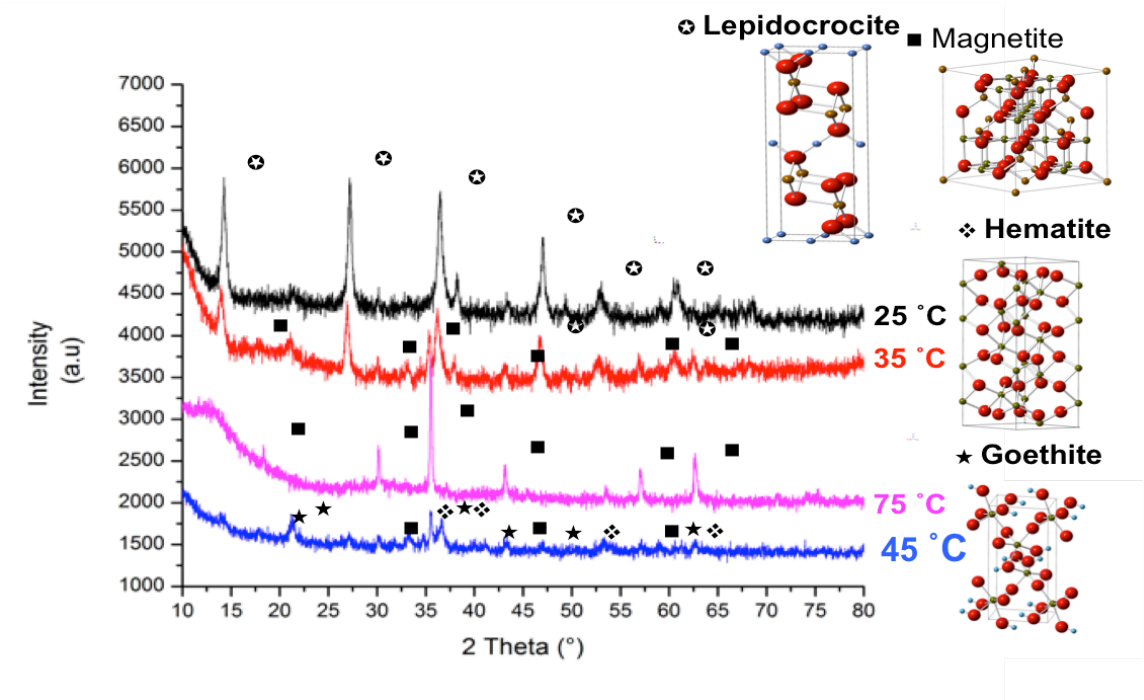

Figure 4-20 XRD patterns of the corrosion products on the surface of the carbon steel in the flow loop with high flow rate (192 gal/min)

Temperature	*Name*	***Formula***	***Percentage***
25 ˚C	Lepidocrocite	γ-FeOOH	100 ±0
35 ˚C	Lepidocrocite	γ-FeO (OH)	58.4 ± 4.5
	Magnetite	Fe_3O_4	41.6 ±4.5
45 ˚C	Hematite	α-Fe_2O_3	17.4 ± 2.5
	Magnetite	Fe_3O_4	13.1 ± 1.57
	Goethite	α-FeOOH	69.5 ± 4.1
75 ˚C	Magnetite	Fe_3O_4	100 ±0

Table 4-6 XRD characterization results for corrosion products forms on the surface of carbon steel inserted inside the flow loop with high flow rate of (192 gal/min)

The corrosion rate of the carbon steel inside the flow loop with high velocity exhibits the same behavior as the low velocity experiments (stirred beaker), where the corrosion rate increases in multiphase as the temperature increases. The corrosion rate increases from 25˚C to 35 ˚C linearly, while it shows no significant differences between 35˚C and 45 ˚C. This can be explained by the formation of the protective layers at 45˚C (goethite and hematite) as shown by SEM and XRD analyses. The corrosion products at 25˚C and 35˚C are composed of lepidocrocite, which is porous, unstable and powdery. As mentioned earlier, and as shown in Figure 4-10, the orthorhombic crystal structure of lepidocrocite allow oxygen to diffuse effortlessly. The corrosion products at 45˚C consist of goethite and hematite. These corrosion forms are considered the most protective layers and act as inhibitors to impede the corrosion process. The crystal structures of these two forms are rhombohedral and hexagonal closed packed as shown in Figure 4-11 and Figure 4-21, respectively.

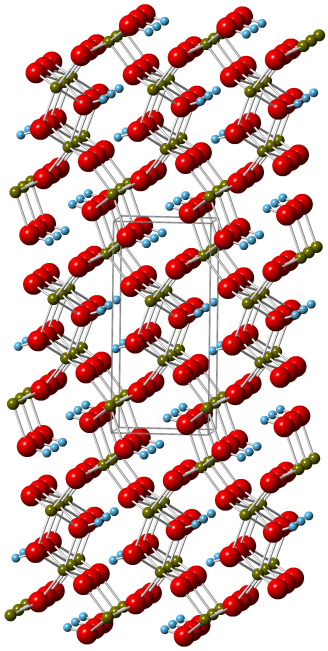

Figure 4-21 packing of goethite unit cells

Moreover, at 75˚C, the carbon steel had significant mass loss in the flow loop with high flow rate due to erosion corrosion. The high flow (turbulent) scraped off the corrosion products of from the metal surface, which resulted in an increase of metal dissolution.

4.3 Corrosion products transformation on the surface of carbon steel at 45 ˚C

As previously shown in Sections 4.1 and 4.2 that at 45˚C and after 7 and 14 days, the corrosion products were found to be hematite and goethite. The formation of these products impedes significantly the corrosion rates. Despite the presence of lepidocrocite as a major product at 25 and 35 ˚C, it was not found at 45˚C after 7 and 14 days. These results raised the following important questions:

1. Does lepidocrocite transform to hematite and goethite at 45˚C as a function of time and temperature?
2. Does the absence of lepidocrocite at 45˚C, after 7 and 14 days, mean it has separated from the metal surface and has moved into the liquid phase?
3. Are hematite and goethite formed directly from the bare metal surface without going through lepidocrocite?

In order to answer these questions partially or completely, a detailed product characterization was conducted and monitored on the corrosion products at 45 ˚C as a function of time. Specifically, carbon steel coupons were immersed in seawater at 45 ˚C for 1, 2, 4, 7, and 10 days. After each time period, the coupons were taken out and dried in a desiccator for 24 hours. Then the corrosion products were scraped off and characterized by XRD and FTIR. Subsequently, the corrosion rates were determined gravimetrically. The results are summarized in the table below:

Time of exposure	The color of the corrosion products	pH	Notes
1 day	Orange	8	The corrosion products were powdery, and easy to remove
2 days	Orange	7	The corrosion product uniformly covered the surface of the coupon
4 days	Orange on the outer surface and black on inner surface if the corrosion layers	6	The corrosion products adhered to the surface of the coupon
8 days	Red on the outer surface and black on the inner surface of the corrosion layers	6	The corrosion products adhered to the surface of the coupon
10 days	Red on the outer surface and black on the inner surface of the corrosion layers	6	The corrosion products adhered to the surface of the coupon

Table 4-7 Summarized-observed results for the corrosion of carbon steel in seawater under low flow rate at 45˚C as function of time

4.3.1 Characterization of corrosion products:

The corrosion products on the surface of carbon steel that was immersed in seawater at 45 ˚C as a function of time were characterized using XRD and FTIR. The purpose of the characterization was only to identify the chemical structures of the corrosion products produced as a function of time. No attempt was made to analyze the crystal structures forms. Therefore, there was no quantitative analysis.

4.3.1.1 The corrosion forms identification

Figure 4-22 exhibits the FTIR spectrum of corrosion products of carbon steel in seawater at 45 ˚C as a function of time.

First day: The FTIR spectrum shows a broad peak at 3165 cm^{-1} which can be assigned to the OH stretching mode in the goethite structure, which is present in all time periods[137]. The three sharp peaks with the same intensity at 1470, 1333, and 1064 cm^{-1} are assigned to ferric hydroxide $Fe(OH)_3$) [75,77,82,138]. The peak at 1667 cm^{-1} is assigned to goethite[138].

Second day: The same peaks of goethite and ferric hydroxide are present. Moreover, the peak at 890 cm^{-1} represents a bond vibration present in goethite[137]. It is worth mentioning that the FTIR spectrum of the lepidocrocite exhibits absorption peaks at (3100 cm^{-}, 1150 cm^{-}, 1020 cm^{-}, and 750 cm^{-1})[98,138]. A relatively small peak at 1159 cm^{-1} was detected on the second day. This small peak may not be related to the lepidocrocite, and may be assigned to the OH stretching of the goethite[139].

Fourth day: The FTIR spectrum shows the same peaks as the second day. These peaks are related to goethite and ferric hydroxide. Furthermore, the new shoulder peak at 800 cm^{-1} and 1000 cm^{-1} are related to ferrihydrite $(Fe(OH)_3$[138].

The eighth and tenth days: the FTIR spectra show that corrosion products contain a mixture goethite and ferric hydroxide.

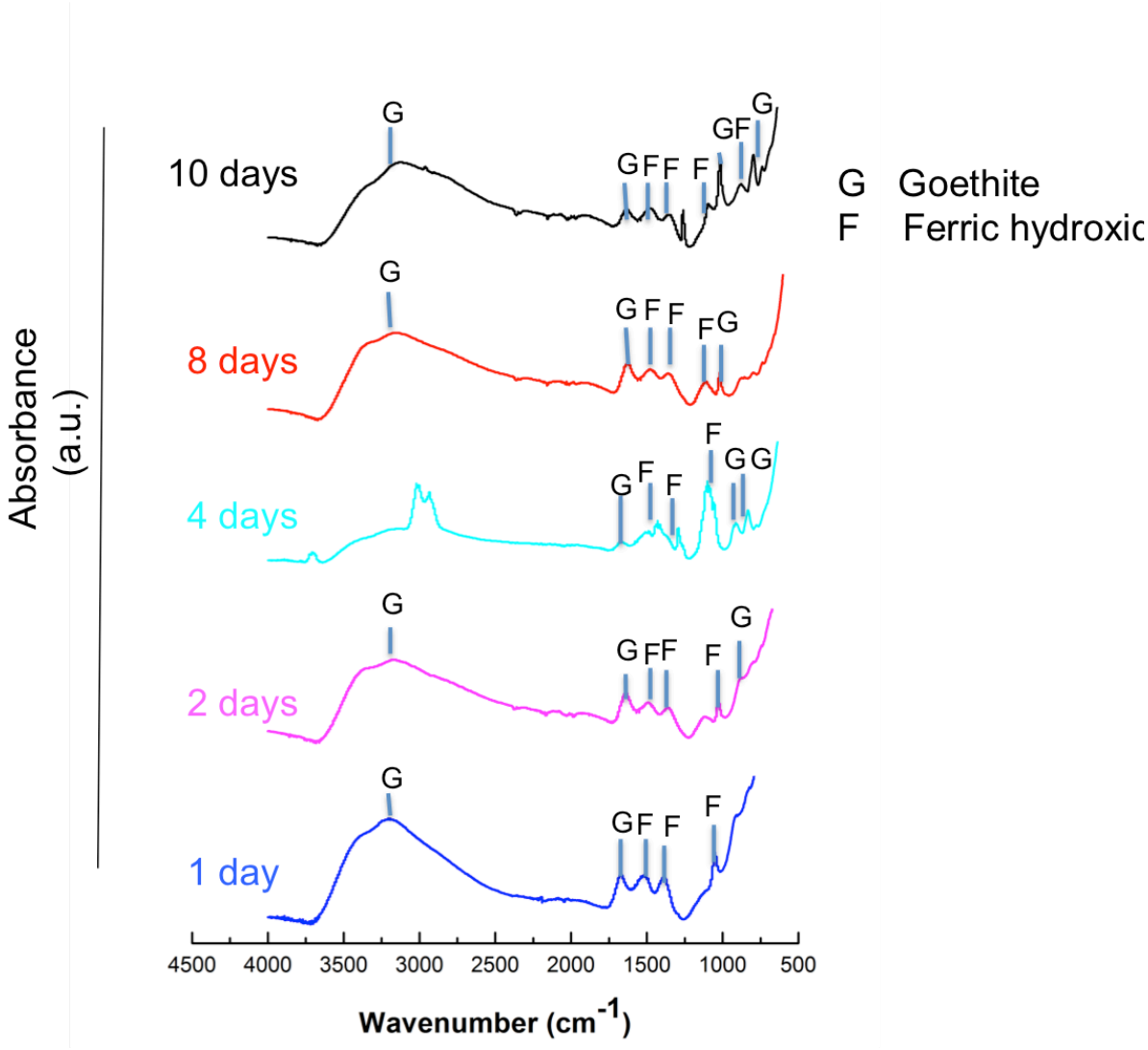

Figure 4-22 FTIR spectra of the corrosion products formed on the surface of carbon steel immersed in a stirred beaker filled with seawater at low velocity of 0.15 m/s at 45˚C

4.3.1.2 Crystal structure of the corrosion products of carbon steel

The crystal structure of the corrosion products of carbon steel in seawater as a function of time was characterized by XRD. Figure 4-23 shows the forms of corrosion products on the surface of the carbon steel.

The first day: The XRD spectrum shows only one wide peak indicating the absence the crystalline structure. This agrees fairly well with the FTIR results, which shows the presence of the amorphous ferric hydroxide (ferrihydrite, $Fe(OH)_3$).

The second day: There were no peaks detected by XRD, which implies the corrosion products on the second day are still amorphous.

The fourth day: The crystalline structure starts to form, and a rhombohedral and cubic crystal structures start to present in the corrosion layers. These structures belong to hematite and magnetite.

The eighth day and tenth day: As shown in Table 4-8 and Figure 4-20, the corrosion products contain a mixture of hematite and magnetite crystal structure.

Time (day)	Crystalline corrosion products form
1	Amorphous –No XRD peaks detected
2	Amorphous –No XRD peaks detected
4	Magnetite
	Hematite
8	Magnetite
	Hematite
10	Magnetite
	Hematite

Table 4-8 XRD results of the corrosion products on the surface carbon steel immersed in seawater at 45 ˚C as function of time

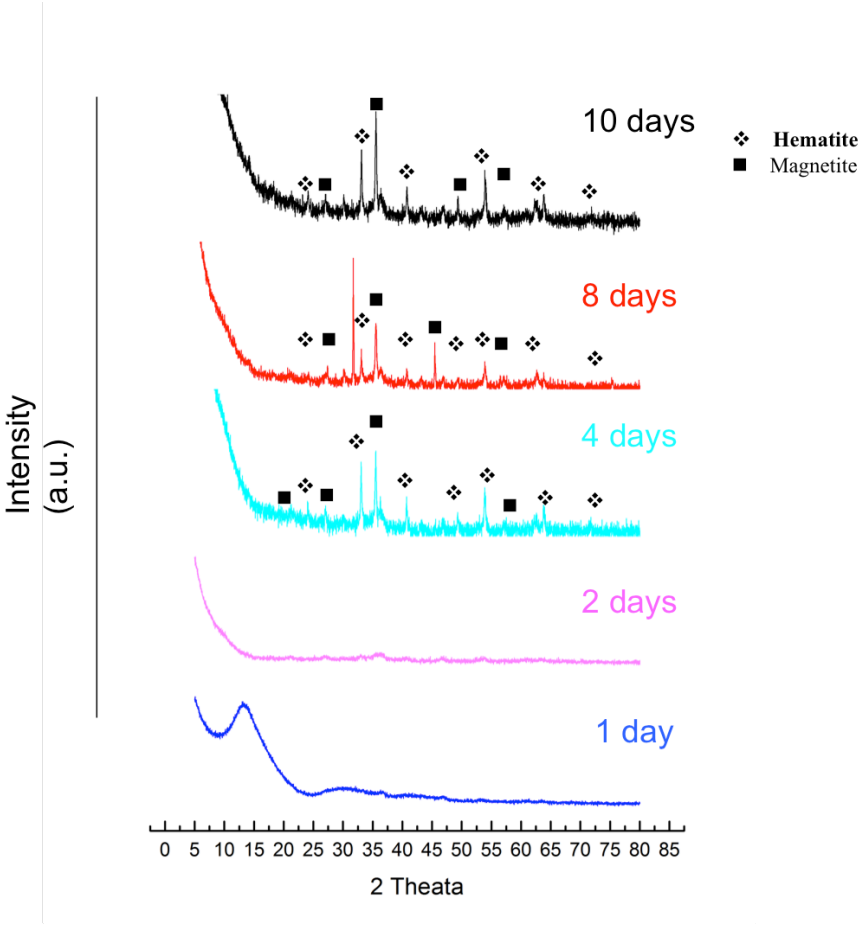

Figure 4-23 XRD pattern for the corrosion products on the surface of the carbon steel in seawater at low velocity 0.15 m/s at 45˚C

4.3.2 Corrosion rate determination of the carbon steel in seawater at 45˚C as function on time

To further investigate the direct formation of hematite and goethite from the Fe as a function of time at 45 ˚C, and since these products impede the corrosion rate, a series of measurements of the effect of the exposure time at 45 ˚C were conducted. The main purpose of these experiments was to determine the effect of the exposure time

and the form of the corrosion product on the corrosion rate as function of time. As shown in Figure 4-24, the corrosion rate decreases as a function of time at 45 ˚C. This decrease indicates the rapid buildup of ferric hydroxide ($Fe(OH)_3$) and goethite at 45 ˚C, as demonstrated by the FTIR and XRD analyses. Consequently, these corrosion products cause a decrease in the corrosion rate since ferric hydroxide ($Fe(OH)_3$) and goethite are protective layers. In addition, the corrosion rate decreases with increasing exposure time due to the formation of hematite. Hematite, as mentioned above, is considered the most protective corrosion product[73,116,140].

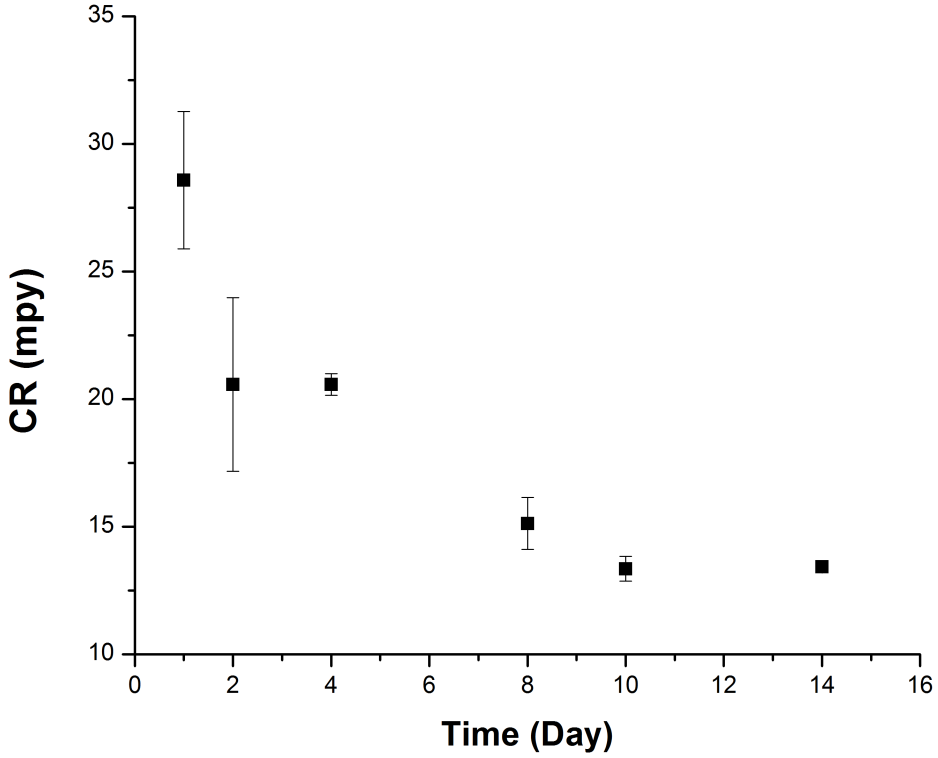

Figure 4-24 The effect of the corrosion products on the corrosion rate of carbon steel immersed in seawater at 45 ˚C in stirred beaker at 0.15 m/s as function of time

4.3.3 Conclusion

The corrosion of carbon steel in seawater at 45˚C starts with anodic and cathodic reaction as shown below:

$$Fe \rightarrow Fe^{2+} + 2e^{-} \qquad \text{Equation 4-9}$$

$$O_2 + 4e^{-} + 2H_2O \rightarrow 4OH^{-} \qquad \text{Equation 4-10}$$

$$2Fe^{2+} + 4OH^{-} \rightarrow 2Fe(OH)_2 \downarrow \qquad \text{Equation 4-11}$$

$$2Fe(OH)_2 + H_2O + \frac{1}{2}O_2 \rightarrow 2Fe(OH)_3 \qquad \text{Equation 4-12}$$

The first form of the corrosion products on the surface of the carbon steel at 45 ˚C is the amorphous ferric hydroxide (Fe $(OH)_3$). This amorphous ferric hydroxide (Fe $(OH)_3$) layer is produced rapidly through the hydrolysis reaction of ferric iron (Fe^{3+}) in the aqueous phase[76]. This hydrolysis reaction to form ferric hydroxide is complicated process, which occurs at pH ≥ 5, or in heated acidic solutions [141]. This hydrolysis proess consists of the following four steps[73,75,76,142]:

1. The formation of ferric hydroxide monomers: Fe^{3+} in aqueous solution is hydrated, and form an octahedron complex as shown in equation below[75]:

$$Fe^{3+} + 2H_2O \rightarrow Fe(H_2O)_6^{3+} \qquad \text{Equation 4-13}$$

This complex donates a proton as shown in the reaction below[75]:

$$Fe(H_2O)_6^{3+} + H_2O \leftrightarrow [Fe(H_2O)_5(OH)]^{2+} + H_3O^{+} \qquad \text{Equation 4-14}$$

The monomers form OH bridges, which give dimers by olation reaction [75]:

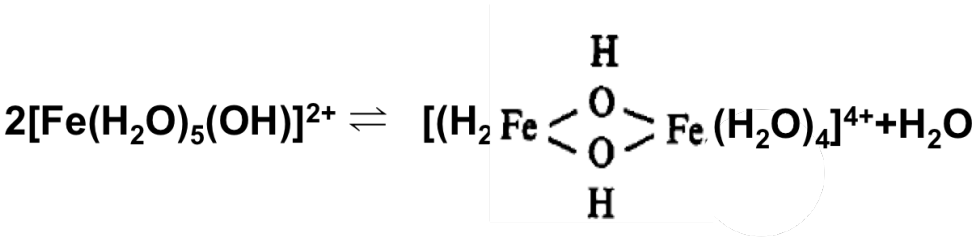

Equation 4-15

2. The rapid growth of small dimer or trimers
3. A slow formation of large polymers through the oxolation: The dimer can split of proton in oxolation reaction as shown in the reaction belwo[75]:

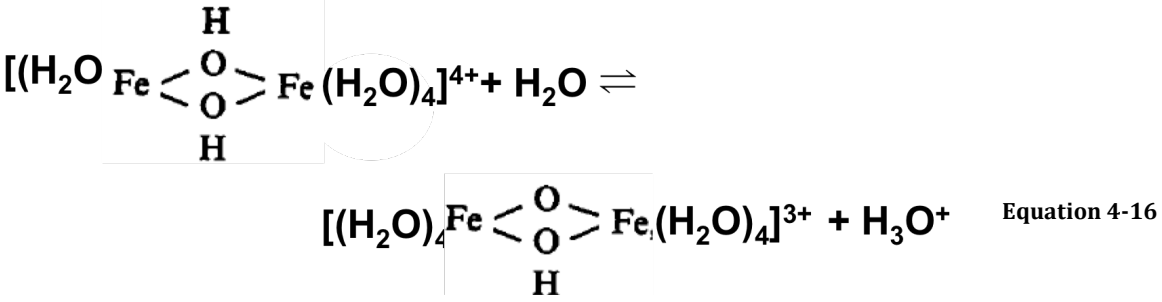

Equation 4-16

The two Fe atoms in the dinucler Fe (III) species can be bound by double ol-bridges or oxo-bridges (Fe-O-Fe). The two types of formation of an oxo-bridge between ferric species is possible through the reaction shown below:

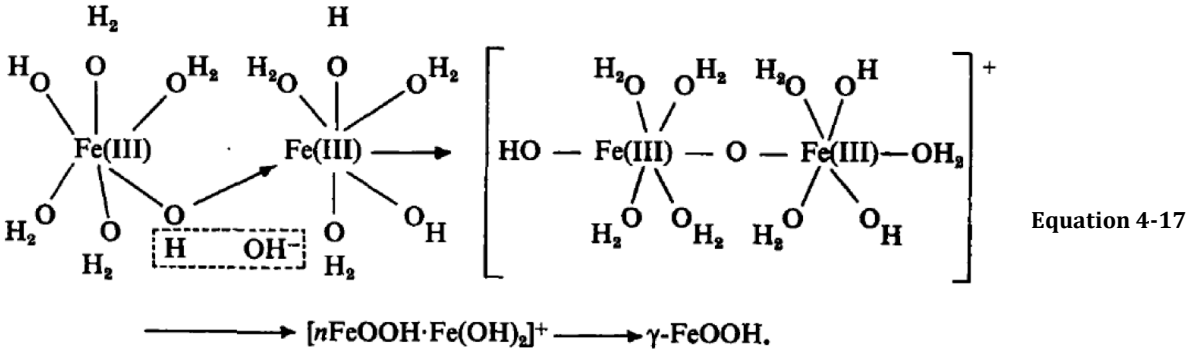

Equation 4-17

4. The precipitation of the amorphous solid.

This polymerization of the ferric hydroxide is a gel that consists of a network of ploynuclear complexes inked up by − O − and − OH bridges. It has been stated that the presence of the amorphous ferric hydroxide on the surface of carbon steel can inhibit the corrosion process, however the mechanism is not yet well understood[73,82].This polymer network of ferric hydroxides may act as a barrier to impede oxygen diffusion throughout the amorphous ferric hydroxide and onto the surface of carbon steel. It is believed that ferric hydroxide prevents oxygen diffusion through its layers, thus decreasing the corrosion rate of the carbon steel[82]. Ferric hydroxide is thermodynamically unstable and transforms to a more stable form of iron oxide-hydroxide such as goethite due to the presence of Fe^{2+} ions in the solution[76,143,144]. It was observed that ferric hydroxide transforms rapidly to goethite in high alkaline solution at 150 ˚C[145]. These reactions decreas the pH slowly due to a slow diffusion of protons from the surface towrd the inside of the crystal[75]. This explains the deacrasing of the pH of the seawater under our experminetal condtion from 8.3 to 6 as shwon in Table 4-7.

On the fourth day, the ferric hydroxide transforms to a weak crystal of hematite. Many studies showed that ferric hydroxide transforms to goethite or hematite [73,76,77,82,142]. The pH of the system is the variable that promotes one formation mechanism over the other because the pH affects the solubility of the ferric hydroxide and the speciation of the iron in the solution [142]. The formation of the hematite is found to be at pH 4-8 and the low concentrations of the Fe(III), while goethite formed at pH 4 and pH 12 at a high concentration of Fe(III)[143,146]. On the eight day, the crystal hematite dominates the corrosion products. A crystal magnetite was also found

in the corrosion products as a result of amorphous goethite transformation at pH 6. Iwasaki also observed the same transformation of amorphous goetihite to magnetite at the same pH[147].

4.4 Electrochemical measurements

The effects of temperature on the carbon steel corrosion were investigated by using the electrochemical measurements. These measurements shed the light on the first cathodic and anodic reactions that occurred on the bare carbon steel surface. These measurements were conducted before the corrosion takes place on the metal surface. The corrosion layers complicate the electrochemical measurements because it participates in the reduction reaction of the sub- reaction[98]. Additional factors that could affect the corrosion reactions are; oxygen diffusion through the corrosion layers; the charge movements between the interface (electron); and the presence of microorganism in the corrosion layers. These factors form many sub-complex reactions on the surface[98,148]. Therefore, studying the corrosion process on bare-clean coupon eliminates the effects of these factors. Also, in order to eliminate the flow rate-induced mass transfer such as O_2 and Cl^-, these measurements were conducted under stagnant conditions. Under these experimental conditions, the anodic reaction is the iron oxidation followed by dissolution, and the cathodic reaction is the oxygen reduction as shown in the reactions below:

$$\mathbf{2Fe \rightarrow 2Fe^{2+} + 4e^-} \qquad \textbf{(Anodic reaction) Equation 4-18}$$

$$\mathbf{O_2 + 2H_2O + 4e^- \rightarrow 4OH^-} \qquad \textbf{(Cathodic reaction) Equation 4-19}$$

The electrochemical measurements are fast and efficient in measuring the corrosion kinetics. Since there is a competition between the anodic and cathodic reactions, the shapes of the polarization curves indicate the predominant one under certain conditions[134].

4.4.1 The effects of temperature on the anodic and cathodic reactions

The influence of temperature on the bare carbon steel surface was studied using Tafel plots and linear polarization resistance (LPR). These electrochemical measurements were implemented with Gamry Potentiostat. The carbon steel compositions are given in Table 3-3-1. The coupons were cleaned with acetone, and then rinsed with distilled water. The carbon steel coupons were mounted as a working electrode in the corrosion cell as shown in Figure 3-3-4. The cell was filled with seawater. Then, the cell placed on the hot plate, and a thermo couple was immersed in the cell to measure the temperature until reach the desired value.

First, Tafel extrapolation experiments were conducted to measure Tafel constant, and to monitor the behavior of the anodic and cathodic reaction at various temperatures. Second, the LPR exterminates were performed to measure the corrosion rate and the polarization resistance of the solution. It is worth mentioning that activation energy cannot be determined from the electrochemical measurements due to the shift of i_{corr} value leading to increases in the error of the measurements, as explained in section 4.2.2. For each temperature, three coupons were used for the electrochemical measurements. The values of the electrochemical parameters reported as average values with standard error of the mean from the three measurements.

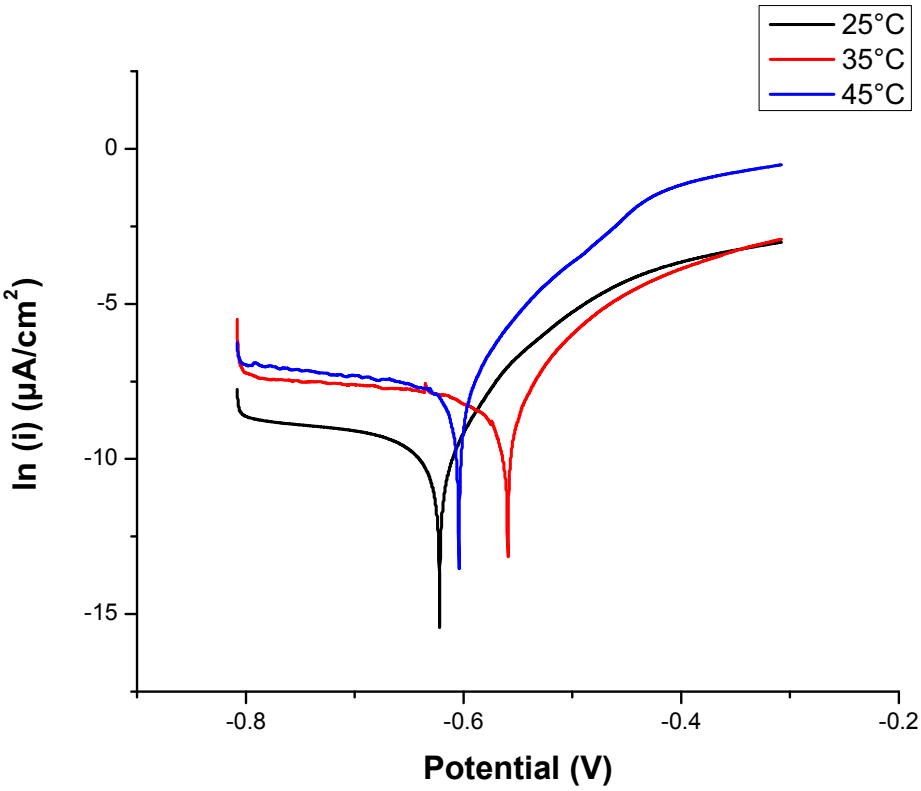

Figure 4-25 A typical Tafel plot for carbon steel in seawater at various temperatures; plots represent data collected from single experiment.

Temper. (˚C)	β_a mV/decade	β_c mV/decade	i_{corr} (μA/cm^2)	$E_{corr.}$ (mV)	CR (mpy)	R_p (Ω)
25	110±3	>120	158.33±10	-662±2	21.75±2.6	338.6±39
35	99.5 ±16	>120	608±22	-676±26	88.7±4.7	70±23
45	105±10	>120	470±53	-667±0	64±17	110±31

Table 4-9 Tafel and LPR results of carbon steel in seawater at various temperatures; the numbers are the average of three experiments set for each temperature. The cathodic Tafel constant is higher than the instrument limitation

Figure 4-25 shows the polarization curves of the carbon steel in seawater at the range of temperatures form 25˚C-45˚C. Table 4-9 shows the values of Tafel constants, the corrosion current density, the corrosion potential, the corrosion rate, and the

polarization resistance of the carbon steel corrosion in the seawater. The reported data is the average from three sets of experiments for each temperature.

With increasing temperature, the corrosion potential shifts to the negative values form (-662±2 mV) to (-676 ±26mV) between 25˚C-35˚C as shown in Figure 4-25 and Table 4-9 This shift in the corrosion potential is due to an increase of the corrosion process [131,133,134].However, at 45˚ C, E_{corr} starts to shifts to the positive value, which indicates that protective corrosion layers start to form rapidly at 45˚C.

As mentioned in the introduction, i_{corr} is related to the corrosion rate as shown in Equation 3-3-5. i_{corr} increases between 25˚C and 35˚C, then decreases at 45˚C as shown in Figure 4-26. These results are in agreement with all other experiments in this work, which demonstrate that the protective layers are produced at 45˚C. These protective layers are composed of goethite and hematite.

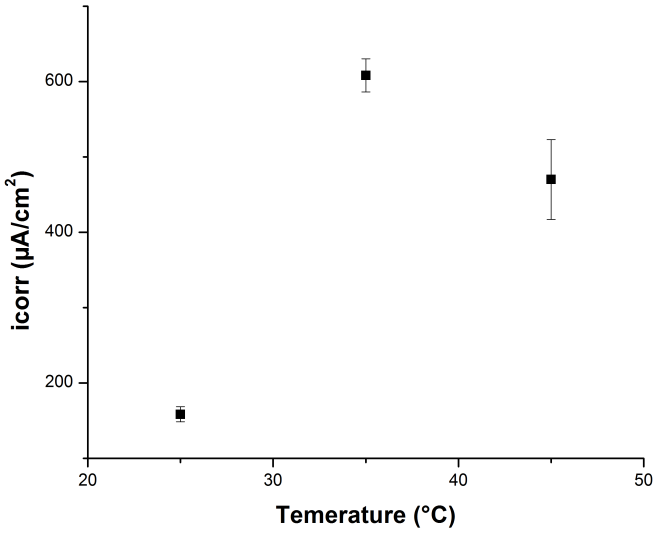

Figure 4-26 The corrosion current density for the carbon steel in seawater at various temperatures under stagnant conditions

At 25˚C-45˚C, the values of the anodic Tafel constants are considerably high implying that the corrosion is under anodic controlled reaction (charge-transfer controlled). Also, the values of β_a did not change significantly with increasing the temperature indicating that temperature does not have impact on the anodic reaction. The cathodic Tafel constants are significantly high indicating the cathodic reaction under the diffusion effects from 25˚C to 45˚C. Since both anodic and cathodic reactions are activation and diffusion controlled, it implies that the corrosion process is mixed controlled.

As shown in Figure 4-27, the corrosion rate increases between 25˚C and 35˚C, and decreases at 45˚C. This is another confirmation of the protective layers formation at 45˚C. As expected, reciprocally, the polarization resistance decreases from (338.6±39 Ω

) at 25 ˚C to (70 ±23 Ω) 35 ˚C, and increases again at 45˚C to 110±31 Ω as shown in Figure 4-27.

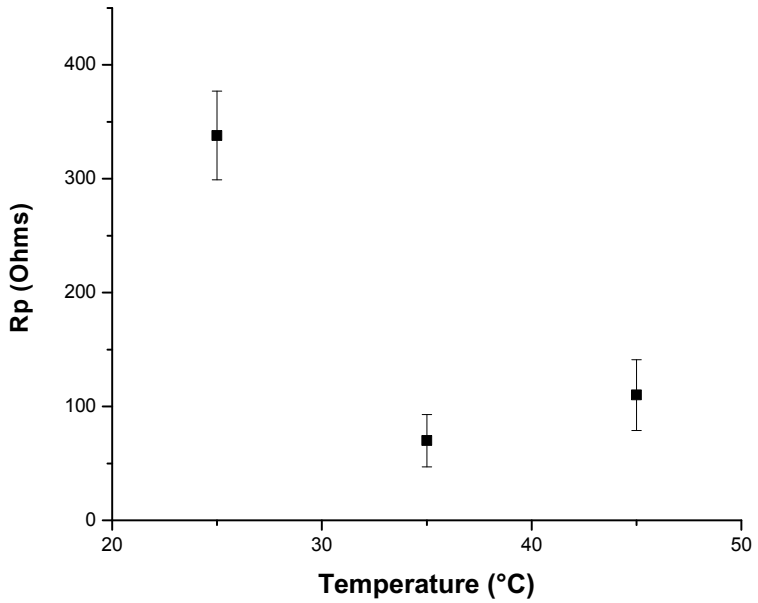

Figure 4-27 The polarization resistance of carbon steel in seawater as function of temperature

4.5 The corrosion rate of carbon steel in crude oil and seawater mixture

As mentioned above, frequently crude oil is transferred inside pipelines with a significant amount of water. This amount can reach up to 30 % of the crude oil volume. Since this work focus on the seawater-induced corrosion in the crude oil pipelines, a set of experiments were conducted to determine the corrosion rate of carbon steel in crude oil and seawater mixture. Crude oil is not corrosive; therefore, it should decrease the corrosion rate comparing with seawater. The purpose of these experiments is to study the effect of the temperature on the corrosion rate in the crude oil and seawater mixture.

These experiments conditions were exactly like the set of stirrer beaker experiments in section 4.1. The corrosion rate of carbon steel in mixture of crude oil and 30 % vol. of seawater with low velocity of 0.15 m/s (60 rpm) for 14 days had been determined gravimetrically at various temperatures. The carbon steel coupons were immersed in crude oil and seawater mixture using the experimental setup (1) as explained above.

4.5.1 Corrosion rate determination

After 14 days of immersion, a very thin film of corrosion products was formed on the surface of the carbon steel coupons at 25˚C and 35 ˚C. However, no corrosion layers were observed on the metal surface at 45˚C and 55˚C. As shown in Figure 4-29, the corrosion rate of carbon steel in a mixture of crude oil and seawater (70% crude oil + 30% seawater) decrease with increasing the temperature.

The crude oil is not corrosive, and it forms a protective layer on the surface of carbon steel. This layer impedes the corrosive ions in seawater to reach the metal surface[67]. At the first stage of pumping of the crude oil/ water mixture, it is expected to have turbulent flow. As the crude oil/ water mixture transport through the pipeline, it reaches laminar flow. Therefore, at the beginning of the pumping, it is expected that the water is emulsified to some extent in the oil phase. Later on, when the crude oil/ water mixture reaches laminar flow. Consequently phase separation occurs.

The hydrocarbons are hydrophobic. The adsorption of these hydrocarbons on the carbon steel surface will make the metal hydrophobic as well. The change of metal surface from hydrophilic to hydrophobic will prevent the water from wetting the metal surface[67,149,150]. The strong attachment of the crude oil to the metal surface is through the coordinate covalent bonds of the sulfur, nitrogen, and oxygen-containing compounds in the oil with the Fe ions on the surface of carbon steal.

In the crude oil pipelines, corrosion is a result of combined effects of many factors such as high flow rate, temperature, presence of corrosive gases such as $CO_{2,,}$ H_2S, and seawater. In this study, the effect of the presence of seawater in crude oil on the corrosion rate at various temperatures is investigated. In section 4.1, the results of the temperature effects on the corrosion rate of the carbon steel in only seawater were presented. In this section, the temperature effects on the corrosion rate of the crude oil/ seawater mixture is presented and discussed. On the contrary of only seawater experiments, as shown in Figure 4-29, as the temperature increases, the corrosion rate decrease.

Crude oil can be corrosive when decomposes into corrosive gases at temperature range 200-400 ˚C. However, under our experimental conditions, the temperature range was between 25˚C-55˚C, which is lower than the of the crude oil decomposition [151]. Thus, under these experimental conditions, no effect from the crude oil decomposed compounds should be expected.

The solubility of oxygen decreases with increasing temperature. Therefore, the corrosion rate decreases at high temperature due to the lack of oxygen.

As the temperature increases, this 70% crude oil/30% seawater becomes more homogeneous. This may increase the effectiveness of the crude oil in protecting the surface of the metal from the corrosive seawater. This homogeneity at high temperature increases the contact of the crude oil with the surface of the metal.

Figure 4-29 shows the corrosion rate decreases further more at high temperature. At high temperature, the formation of the chemical bonds between the sulfur, oxygen, and nitrogen containing compounds in the oil and the Fe ions on the carbon steel surface increases[152]. More formation of these bonds enhances the adherence of the crude oil on the surface, and leading to more passivation layer, and consequently decreases the corrosion rate. . It was reported that naphthenic acid and the nitrogen containing compounds in the crude oil show a significant effect on decreasing the corrosion rate of carbon steel in the crude oil[67]. Even after a thorough rinsing with toluene, SEM-EDS shows the presence of nitrogen, sulfur and oxygen on the surface of the carbon steel as

shown in shown in Figure 4-28.

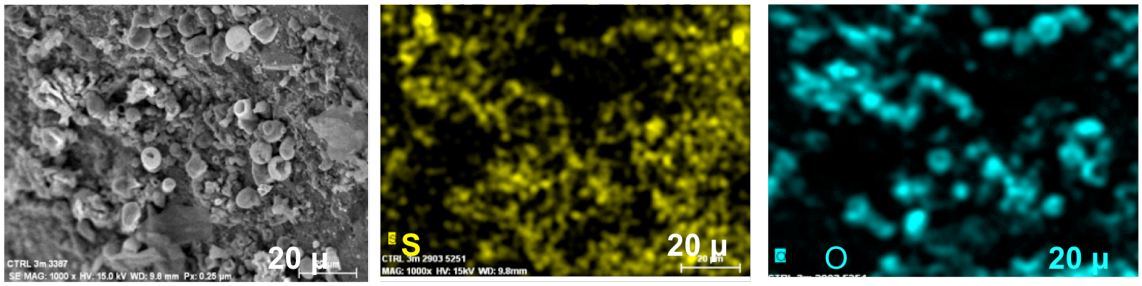

Figure 4-28 SEM -EDS image for the corroded carbon steel in 70% crude oil and 30% seawater at 45 ˚C. It shown the presence of S, O, even after washing the crude oil form the coupon

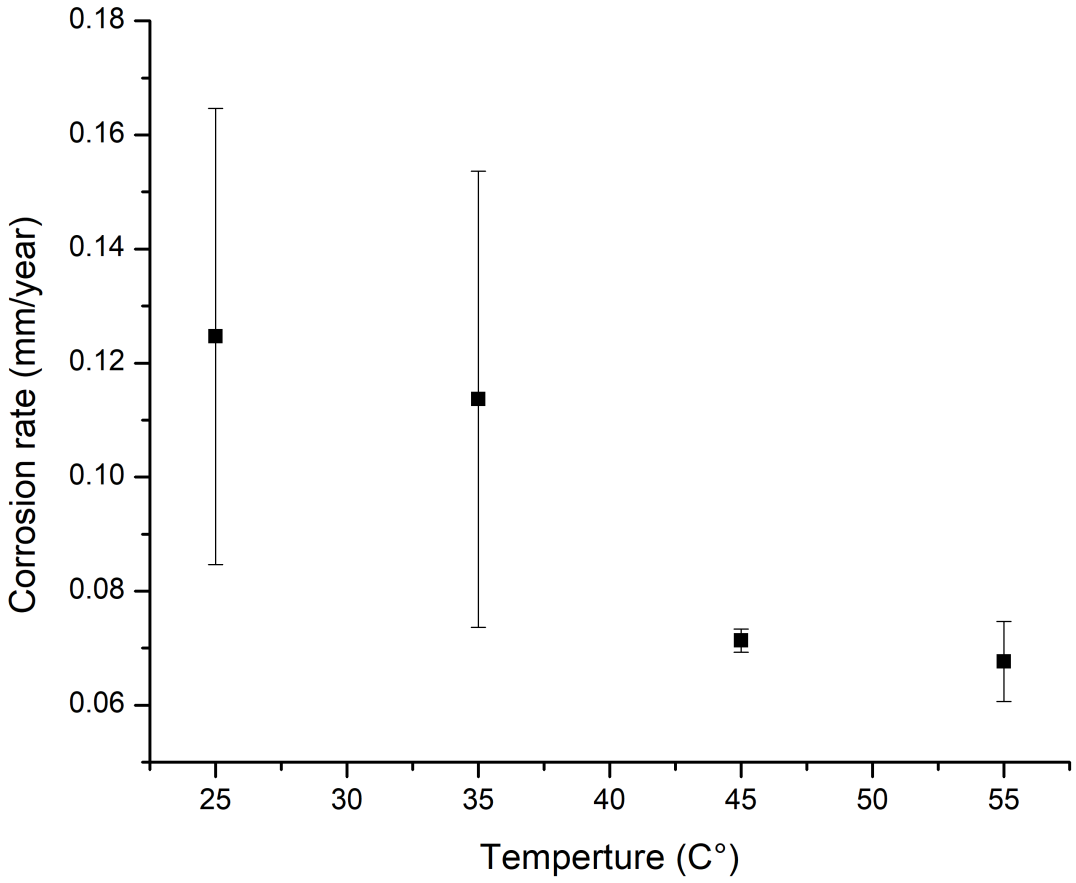

Figure 4-29 The corrosion rate of carbon steel in in stirred beaker filled with (of 70% crude oil + 30 % seawater) at velocity (0.15 m/s)

4.5.2 Pitting corrosion on the surface of carbon steel in crude oil and sweater mixture

Figure 4-30 shows that surface of carbon steel exposed to crude oil/water mixture exhibits low uniform corrosion at 25˚C and 35˚C. As the temperature increases to 45˚C and then to 55˚C, no uniform corrosion was observed on the surface of carbon steel. On the contrary, as the temperature increases, the pitting corrosion was observed. Therefore, the pitting corrosion is the dominant corrosion type in crude oil and seawater mixture.

In order to investigate the pitting corrosion on the surface of carbon steel, SEM analysis was performed after cleaning the coupons following the ASTM cleaning procedure [95]. Figure 4-31 illustrates different sizes of pits and cracks on the surface of the carbon steel. To further investigate the pitting corrosion, cross sectional analysis was conducted. The cross sectional shows that the pits length increase with increasing temperatures as shown in Table 4-10.

At the temperature increases, the passive layer, which consists of crude oil and corrosion products, undergoes thermal stress leading to breakages. These breakages are microscopic in size, and the rest of the surface remains covered with passive layer. The break-surface becomes the anode and the surrounding area becomes the cathode. Consequently, the corrosion starts to become localized leading to initiate the pits on the surface. As mentioned in the introduction, pitting corrosion is localized corrosion that is promoted by the presence of Cl^-.

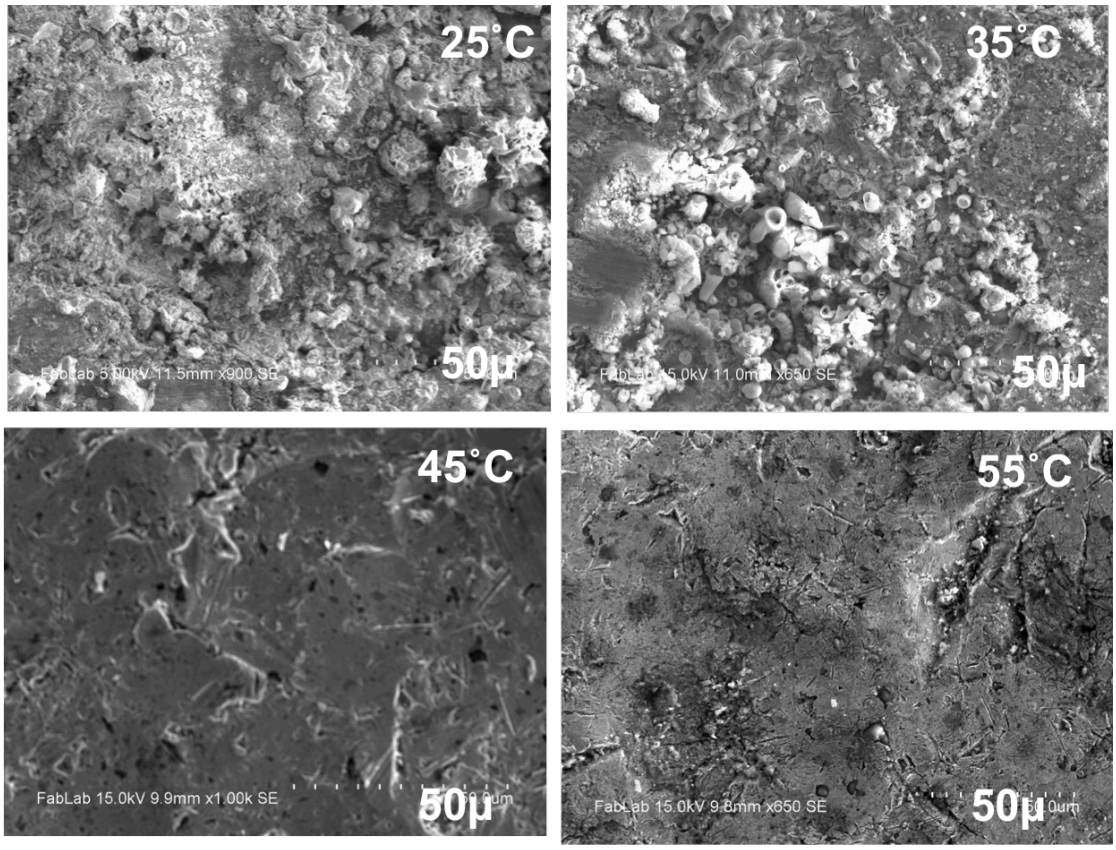

Figure 4-30 SEM images of the surface of corroded carbon steel in 70% crude oil and 30% seawater mixture at velocity 0.15 m/s at various temperatures

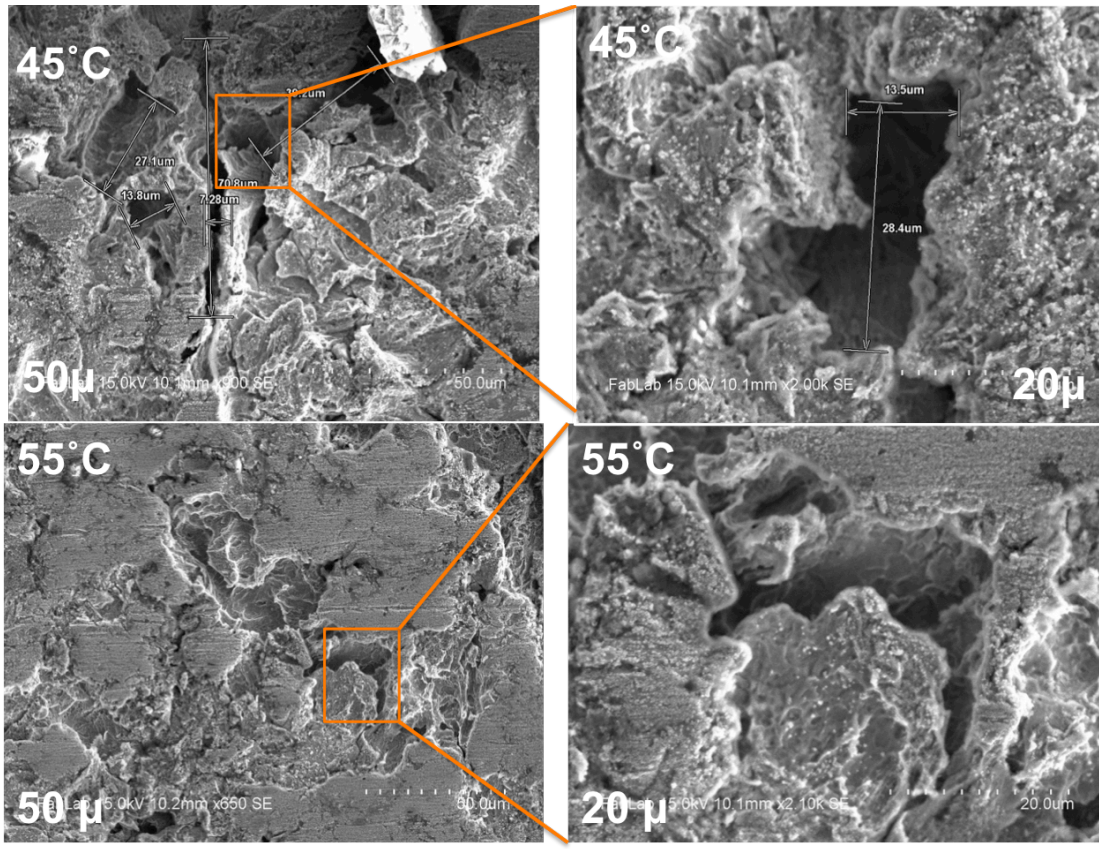

Figure 4-31 SEM images for the carbon steel surface after the cleaning from the corrosion in crude oil and seawater mixture at low velocity 0.15 m/s

Temperature (˚C)	*Pit's length (µm)*
25	8.14 ±1.36
35	7.24 ± 1.25
45	9.87 ±1.26
55	11.5 ± 1.1

Table 4-10 Pits length on the surface of carbon steel immersed in 70% vol. and 30% vol seawater mixture at various temperatures and velocity at 0.15 m/s

5 Conclusion, contribution to science, and suggestions for future work

5.1 Conclusion

One of the most important achievements of this work is the identification of the corrosion products and the mechanisms of their formation at various temperatures and flow rates in seawater and crude oil/ seawater mixture. Based on the results and discussion in Chapter 4, Figure 5-1 summarizes the main concluded mechanisms of the formation of corrosion products of carbon steel in the presence of seawater, and seawater/crude oil mixture at various temperatures and flow rates.

The outlined mechanism was achieved through the following:

A: Identification of the chemical structure of the corrosion products at various exposure times, temperatures, and flow rates.

B: Identification of the crystal structures of the corrosion products as a function of exposure time, temperature, and flow rate.

C: The effects of the corrosion products on the corrosion rate.

D: The effect of temperature on the predominancy of the anodic and cathodic reactions, as well as polarization resistance.

E: Determination of the corrosion rates at various temperatures and flow rates in seawater and seawater/crude oil mixture

F: Determination of the overall-observed activation energy of the corrosion process at low and high flow rates.

5.1.1 The positive and negative effects of temperature on the corrosion rate at a constant low angular velocity of 0.15 m/s (stirred beaker experiments)

In this work, it has been concluded that the temperature has both negative and positive effects on the corrosion rate. As expected, the overall effect of elevated temperatures negatively impacts the surface of carbon steel by increasing the corrosion rate. Also, O_2 diffusion through the corrosion layers increases with temperature further enhancing the increase of the corrosion rate. However, in this work, it has been concluded that the formation of protective corrosion products at certain temperatures impedes oxygen diffusion leading to a decrease in the corrosion rate. Throughout this work, it was demonstrated that the temperature has a significant effect on the chemical and crystal structure of corrosion products formed on the surface of carbon steel in seawater. These corrosion products consist of different forms of iron oxide and iron oxide hydroxide. The temperature has a strong effect on the crystallization process of these corrosion products. In addition, temperatures above 45 ˚C have shown to induce the dissolution of the amorphous ferric hydroxide. In order to fully understand the changes in the chemical structure and morphology of the corrosion products, they were qualitatively and quantitatively characterized using various techniques, over a range of temperatures between 25 ˚C and 75 ˚C.

The corrosion rate increases from 0.21± 0.002 mm/year at 25 ˚C to 0.33 ± 0.003 mm/year at 35 ˚C. At these temperatures, it was found that the outer rust layer contains (60 ± 10) % of γ-iron (III) oxide hydroxide (lepidocrocite) with an orthorhombic structure, while the inner rust layer contains a low (40 ± 10) % of magnetite with cubic structure. Since the orthorhombic structure of lepidocrocite is porous, O_2 can easily diffuse through it leading to an increase in the corrosion rate.

On the contrary, it was shown that corrosion rate does not increase between 35 ˚C and 45 ˚C. The corrosion rates at both 35 ˚C and 45 ˚C were found to be 0.34 ± 0.002 mm/year. At 45 °C, the corrosion layers consist of crystalline hematite and magnetite, amorphous goethite, and a gel-like structure of $Fe(OH)_3$. The crystalline portion of the corrosion products consists of (55 ± 9.4) % hematite and (44.8 ± 9.4) % magnetite. The hematite structure has hexagonal closed-packed (hcp) arrangement that stacks along [001] direction. This structure has a low concentration of structural defects and low grain boundaries. Hence, this crystal structure impedes the diffusion of oxygen, and eventually decreases the corrosion rate. The decrease in the availability of O_2 was confirmed by Tafel plot, where the anodic reaction was found to be the predominant one. Finally, the amorphous portion of goethite and the gel-like $Fe(OH)_3$ also impedes O_2 diffusion contributing to the decrease in the corrosion rate.

The results of this study also show that as the temperature increases the oxidation state of the corrosion products increases. The XPS data in section 4.1.4 discuses the effects of the temperature on the ratio of oxidized (O^{2-}) to hydroxyl (OH^-) species. At 25

°C the concentration of OH^- species appears to be higher than the concentration of O^{2-} species in the corrosion products formed. However, all temperatures above 25 °C showed higher concentration of O^{2-} species with the highest ratio value at 65 °C ($O^{-2}/OH^- = 1.17$). This indicates that the degree of oxidation of the carbon steel surface increases with temperature, since the presence of O^{2-} increases, resulting in the formation of higher concentrations of α-Fe_2O_3, and Fe_3O_4.

However, at 75 °C the ratio of (O^{-2}/OH^-) decreases to 1.03, resulting to an $[O^{2-}] \approx [OH^-]$ as shown in Table 4-3. This result may be explained by the dissolution of the corrosion products at 75 ˚C exposing the bare surface of the metal to seawater. Once the bare surface exposes to seawater the effect of the corrosion products becomes negligible. So, it is expected at this stage, that the corrosion process through the redox reactions will start for the beginning. The combined results of XRD, Raman spectroscopy and XPS revealed the presence of lepidocrocite and magnetite at 25 °C, and hematite as the main phase at 45 °C. The results of Raman agree with the XRD measurements, indicating the presence of hematite at 45 ˚C in the corrosion products. In contrast, the existence of goethite is not seen in the observed area by XRD, even though the Raman results suggest its presence at 45 ˚C. This can be explained by the fact that α-FeOOH (goethite) is in amorphous state, which has no XRD signal. Although XRD indicates that the corrosion products contain magnetite only at 75 °C, Raman spectroscopy results reveal the presence of magnetite (Fe_3O_4) and hematite (Fe_2O_3). One can conclude that as temperature increases, the diffusion of oxygen increases through the corrosion layers forming more corrosion products with higher oxidation states. However, at 45˚C, the corrosion rate did not change due to the formation of protective hematite, goethite and magnetite.

5.1.2 Answering an important question on the formation of the corrosion products as a function of time at 45 °C.

To answer this question, the following experiments were conducted:

1. Characterizing the changes of the corrosion products, at 45˚C, as a function of time was conducted. As shown in Figures 4.21 and Figure 4.22
2. Dependency of the corrosion rate on the exposure time at 45˚C.

At the first stages of the corrosion process, the corrosion products are consist of goethite and the amorphous ferric hydroxide $Fe(OH)_3$. The ferric hydroxide is formed by a rapid hydrolysis reaction of ferric iron (Fe^{3+}), which impedes the O_2 diffusion. Around the fourth day, the ferric hydroxide starts to transform into poorly crystalline hematite, which is also considered as a protective layer since decreases the O_2 diffusion. Also, around the fourth day, goethite transforms to poorly crystalline magnetite. Hematite is known to be the most stable and protective form of iron oxides. As for magnetite, its role in the corrosion process is debatable. On the 8^{th} day or so, the crystalline structures of the magnetite and hematite become distinguishable as measured by XRD. In conclusion, at around 45˚C, the formation of these protective layers counter the positive effect of this temperature.

One of the most revealing results of this work is that the corrosion rate increases in multiple phases as temperature increases. Below 35 °C the oxide formation is dominated by lepidocrocite. In the intermediate temperature range (35 °C and 45 °C),

hematite is the predominant mineral form, which inhibits corrosion limiting its rate. This can be explained by the fact that O_2 diffusion through the corrosion layers is affected by the crystal structure of the corrosion products. Hence, since the crystal and the chemical composition of the products change as a function of temperature, one would expect that O_2 diffusion change accordingly.

Hematite is the most thermodynamically stable form of iron oxide with standard free energy of formation ($\Delta G°_f$) of -742 kJ/mol. Lepidocrocite which is observed in greater abundance at low temperatures has a $\Delta G°_f$ of only -480 kJ/mol. The crystal structure of hematite is isostructural with corundum. The oxygen ions are in a hexagonal closed-packed (hcp) arrangement stacked along the [001] direction, with Fe (III) ions occupying the octahedral sites. This structure has a low concentration of structural defects, which leads to decrease in the grain boundaries. Consequently, the oxygen diffusion decreases, and the corrosion is hindered. Furthermore, Raman reveals goethite presence at 45 °C, which is considered as protective layer that also impedes the corrosion rate.

As the temperature increases further to 55 °C and 65 °C, the corrosion products become powdery and can be easily removed by the agitation. Consequently, the carbon steel surface is exposed to the seawater again, and the corrosion rate increases.

5.1.3 The effects of temperature on the anodic and cathodic reactions

The effect of the temperature on the corrosion rate was also investigated though Tafel plot measurements and the results agreed fairly well with the gravimetric method. As shown in section 4.3.1, the corrosion potential increases (positive shift) from 25 ^{o}C to 35 ^{o}C indicating the increase in the corrosion rate. At, 45 ^{o}C, there is a decrease in the corrosion potential (negative shift) demonstrating a decrease in the corrosion rate. These results consolidate the conclusion that the formation of goethite and hematite at 45 ^{o}C act as protective layers negatively affecting the corrosion rate of carbon steel. The electrochemical results in Figure 4-23 also confirm that there is an increase in i_{corr} from 25 ^{o}C to 35 ^{o}C, followed by a decrease at 45 ^{o}C.

Based on the electrochemical results, the following important conclusions were reached:

1. The corrosion is anodically controlled (charge-transfer controlled) between 25 ^{o}C and 45 ^{o}C.

2. There is no significant effect of the temperature on the anodic reaction.

3. The cathodic Tafel constant (indicative of diffusion controlled reactions) is significantly high over the temperature range of 25 ^{o}C - 45 ^{o}C.

4. Since both the anodic and cathodic reactions are activation and diffusion controlled, it is concluded that the corrosion process of this system is mixed controlled.

5.1.4 The compound effects of temperature on the corrosion rate at constant high flow rate of 192 gal/min

As discussed in the experimental and the results and discussion sections, a stainless-steel loop was constructed with a flow rate of 192 ± 2 gal/min. Similar to the low flow rate results (stirred beaker experiments), at high flow rate the corrosion rate increases in multiple phases as the temperature increases. Again, as in the low flow rate experiments; there was no significant increase in the corrosion rate between 35^{o}C and 45^{o}C. This can be explained by the formation of the protective layers of crystalline goethite and hematite. Between 45 ^{o}C and 75 ^{o}C, the corrosion rate increases sharply. It is concluded that erosion corrosion present at high flow rates and temperatures has a significant effect, and contributes to the overall increase of the corrosion rate.

5.1.5 The absence of green complex or green rust

As previously discussed in section 4.1.6, the absence of the green rust in this work, may be related to the relatively high pH = 8.3 of seawater. In this work, all experiments have been performed at pH 8.3 (the pH of natural seawater). Green rust can form on the surface of carbon steel during the first few minutes of the immersion in seawater as an intermediate, and consecutively transform into lepidocrocite in a short period of time, before we are able to detect and validate its formation.

5.2 Contribution to science

1. The importance of the relationship between corrosion rate and corrosion products on carbon steel exposed to seawater

This work demonstrated for the first time the strong correlation between the corrosion rate of carbon steel in seawater and the dynamic changes of the chemical structure and morphology of the corrosion products as a function of temperature. Most of the previous studies in the field have simplified the temperature effects of the corrosion rates as a typical Arrhenius relationship. This research provided for the first time, strong evidence that the temperature dependency of the corrosion rate is not constant. Therefore, the simple approach of typical Arrhenius behavior is not valid and can lead to serious miscalculations in the projection of the long-term stability of carbon steel pipelines in the crude oil industry. This research has proven that the decisive temperature effects reside in the changes of the corrosion products on the surface of the carbon steel. The nature of every single corrosion product, weather or not passive or active, can play a crucial role in determining the corrosion rate. This can clearly be explained by the fact that changing the nature of the corrosion products, chemically and morphologically, has a significant impact on the oxygen diffusion from the aqueous phase through the corrosion layers. This study demonstrated that the corrosion rate of carbon steel coupons increases overall as a function of temperature when immersed in seawater. However, the temperature dependency of the corrosion rate is variable. While the corrosion rate is (0.21 ± 0.2) mm/year at 25 °C, it increases to (0.33 ± 0.2) mm/year at 35 °C. However, no

statistically significant increases in the corrosion rates are observed between 35 °C and 45 °C. At temperatures higher than 45 °C, the corrosion rate increases at a constant rate of approximately 0.1 mm/ year per 10 °C. At 25 °C-35 °C, it was clearly shown that fine plates (flowery structures), non-protective layer, of lepidocrocite (γ-FeOOH) is the major component of the corrosion products. Hence, the molecular oxygen can diffuse from the aqueous phase through this porous structure, enhancing the corrosion rate. At around 45 °C, the surface morphology of the iron oxide was significantly different and less homogeneous than the one observed at 25 °C. Several crystalline shapes can be observed, including plates, spindles, and pseudo-cubes, which are identified as hematite and magnetite. Also, at around 45 °C, the amorphous goethite and the gel-like $Fe(OH)_3$ are formed. All these crystalline and amorphous corrosion products act as protective layers, because of their O_2- semi-barrier property. However, in the presence of magnetite at 75 °C, no cracking or spallation of the rust layer was observed, although the porosity is still high.

2. Temperature effect on the corrosion mechanism and the activation energy

This work provides the following novel ideas:

Assuming a single transition state, the apparent activation energy is 12.76 kJ/mole. This value cannot be considered as the activation energy for this process, since temperature has both positive and negative effects on the corrosion rate. Needles to say, as the temperature increases, the rate of the corrosion increases. However, the increase in temperature has also the following negative effects on the corrosion rate:

I. Increasing the diffusion of oxygen through the corrosion layers

II. Enhancing the erosion corrosion by increasing the dissolution process of the corrosion layers leading more corrosion rate

Additionally, there are positive effects of temperature on the corrosion rate, as follows:

I. Formation of protective layers at around 45 ˚C comprised of hematite and goethite

II. Decrease of the oxygen concentration in the liquid phase

Based on the aforementioned positive and negative effects of temperature on the corrosion rate, the measured value of activation energy shouldn't be used as an absolute value for the overall corrosion rate.

3. The relationship between the flow rate and the measured observed activation energy

This work demonstrates the importance of the flow rate on the determination of the observed measured activation energy. Specifically, this works show that the thickness of the diffusion boundary layer has a tremendous role on the overall activation energy. When this layer disappears due to vigorous agitation such as in stirred beaker experiments, the measured activation energy is relatively very low. However, at high flow rate of 192 gal/min, where the diffusion boundary layer is relatively thick, the measured activation energy is much higher than the stirred beaker experiment. These findings are very crucial to determine the more realistic activation energy of the corrosion of the crude oil pipeline, and raise a flag on the experiments carried out in the lab where stirred beakers are used. Based on these findings it is highly recommended that determining the activation energy should be carried out under the same flow rate of the pipelines.

4. The crude oil as corrosion inhibitor

Despite the fact that solubility of oxygen increases in the presence of crude oil, this work shows that the corrosion rate decreases in the presence of the crude oil. It should be mentioned that these experiments were conducted in stirred beaker. So, the vigorous agitation renders this mixture to be more homogeneous. This increase in homogeneity enhances the contact of the crude oil with the metal surface protecting it from the corrosive seawater.

There are enormous proposed probabilistic models on corrosion. Specifically, many models try the pipelines failure. The data analysis and the conclusion in this work provide crucial information for these models. In addition, these models have validated this research data.

5.3 Suggestions for future work

Based on the results and the conclusion of this PhD dissertation, the following suggested research plan and experiments would be crucial to continue elucidating the mechanism of the carbon steel corrosion under different conditions:

1) The use of polarization resistance and Tafel plot to further determine the role of the protective layers at high flow rate of 192gal/min. Since the exact values of these values βa, βc, i_{corr}, and Rp are important to determine at which temperature the anodic or cathodic reaction would be the dominant one. Throughout the performance of this work, the trend of the changes in these values was demonstrated.

2) The mechanism of the effects of the crude oil/seawater ratio on the corrosion rate at high flow rate is similar to the oil field, such as 192 gal/min. This task should be related to the changes in the thickness of the diffusion boundary layer as a function of temperature and crude oil/ seawater ratios.

3) The mechanisms of the [CO_2] concentration on the corrosion rate at high flow rate and the various crude oil/seawater ratios.
4) The mechanism and the rate of pitting formation and a function of crude oil/seawater ratios.
5) Even after a thorough cleaning with toluene, coupon of the carbon steal exposed to crude oil/ seawater mixture, show attachment of nitrogen, oxygen, and sulfur containing compounds illustrating the adsorption of the crude oil on carbon steal surface. SEM- EDS technique was used to conduct these experiments. So, it is strongly recommended to continue investigating the following:
   I. Elucidating the mechanisms of the adsorption of the nitrogen, oxygen, and sulfur containing compounds in the crude oil on the carbon steal surface
   II. The effects of the crude oil/ seawater ratios on the corrosion rates at various temperatures and the flow rates

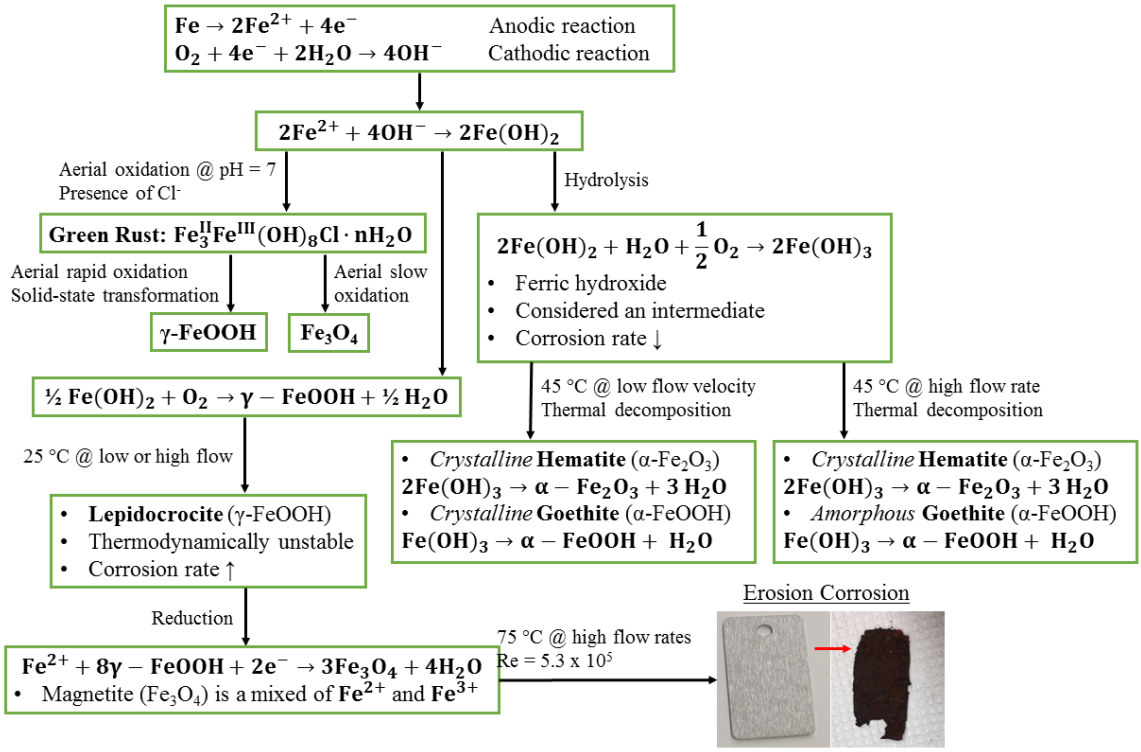

Figure 5-1 Summary of the concluded overall mechanism of carbon steel corrosion in seawater

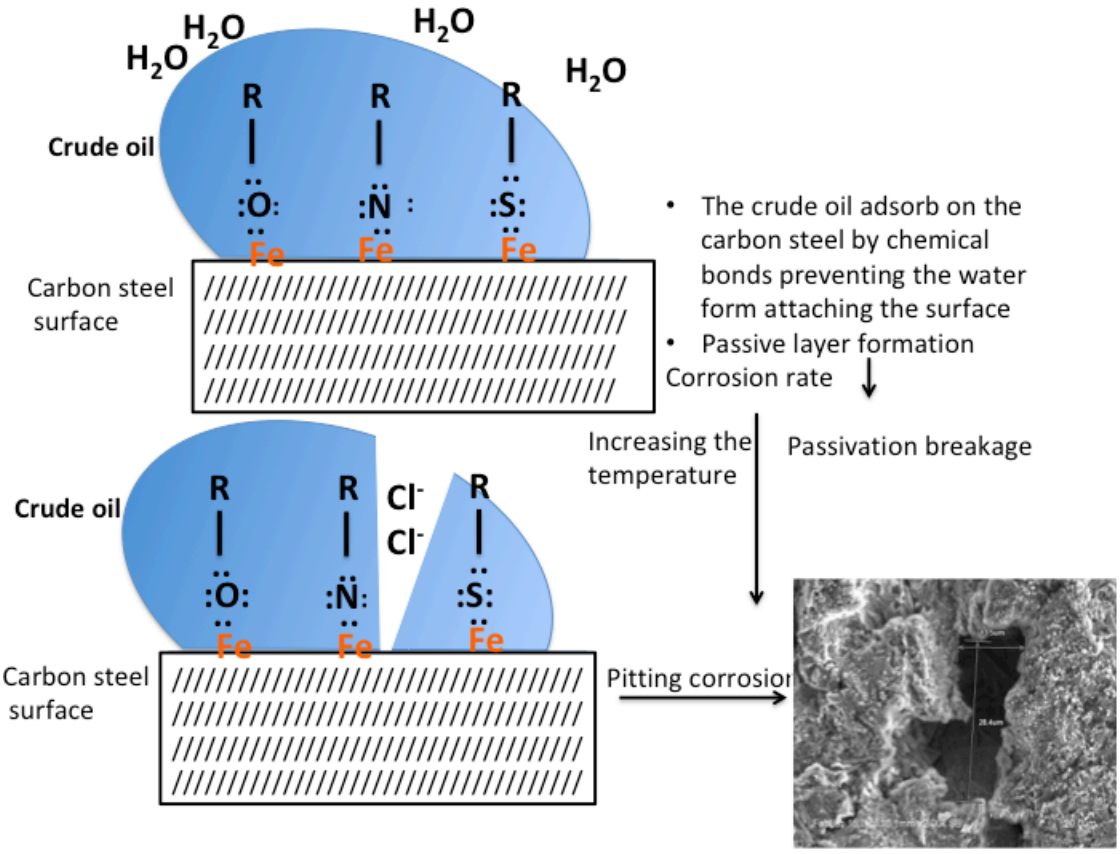

Figure 5-2 The summarized concluded mechanism of the carbon steel corrosion in crude oil and seawater mixture

Bibliography

(1) Fontana, M. *Corrosion Engineering*, Third.; 2005.
(2) Eliaz, N.; Shemesh, G.; Latanision, R. M. Hot Corrosion in Gas Turbine Components. *Engineering Failure Analysis* **2002**, *9* (1), 31–43. https://doi.org/10.1016/S1350-6307(00)00035-2.
(3) Sidhu, T. .; Agrawal, R. D.; Prakash, S. Hot Corrosion of Some Superalloys and Role of High-Velocity Oxy-Fuel Spray Coatings—a Review. *Surface and Coatings Technology* **2005**, *198* (1–3), 441–446. https://doi.org/10.1016/j.surfcoat.2004.10.056.
(4) Bardal, E. *Corrosion and Protection*; Springer Science & Business Media,., 2007.
(5) Bell, T. How Can You Calculate the Rate of Metal Corrosion? https://www.thebalance.com/corrosion-rate-calculator-2339697 (accessed Aug 5, 2018).
(6) George, K.; Wang, S.; Nesic, S. MODELING OF CO2 CORROSION OF MILD STEEL AT HIGH PRESSURES OF CO2 AND IN THE PRESENCE OF ACETIC ACID. 16.
(7) De Waard, C.; U. Lotz; Dugstad, A. Influence of Liquid Flow Velocity on CO~ 2 Corrosion: A Semi-Empirical Model. *CORROSION-NATIONAL ASSOCIATION OF CORROSION ENGINEERS ANNUAL CONFERENCE-NACE* **1995**.
(8) de Waard, C.; Smith, L.; Ltd, I.; Craig, B. D. THE INFLUENCE OF CRUDE OIL ON WELL TUBING CORROSION RATES. 10.
(9) Shi, Z.; Liu, M.; Atrens, A. Measurement of the Corrosion Rate of Magnesium Alloys Using Tafel Extrapolation. *Corrosion Science* **2010**, *52* (2), 579–588. https://doi.org/10.1016/j.corsci.2009.10.016.
(10) Alonso, C.; Andrade, C.; González, J. A. Relation between Resistivity and Corrosion Rate of Reinforcements in Carbonated Mortar Made with Several Cement Types. *Cement and Concrete Research* **1988**, *18* (5), 687–698. https://doi.org/10.1016/0008-8846(88)90091-9.
(11) Peng, S.; Zeng, Z. An Experimental Study on the Internal Corrosion of a Subsea Multiphase Pipeline. *Petroleum* **2015**, *1* (1), 75–81. https://doi.org/10.1016/j.petlm.2015.04.003.
(12) Castaño, J. G.; Botero, C. A.; Restrepo, A. H.; Agudelo, E. A.; Correa, E.; Echeverría, F. Atmospheric Corrosion of Carbon Steel in Colombia. *Corrosion Science* **2010**, *52* (1), 216–223. https://doi.org/10.1016/j.corsci.2009.09.006.
(13) Nešić, S.; Solvi, G. T.; Enerhaug, J. Comparison of the Rotating Cylinder and Pipe Flow Tests for Flow-Sensitive Carbon Dioxide Corrosion. *CORROSION* **1995**, *51* (10), 773–787. https://doi.org/10.5006/1.3293555.
(14) Yang, J.; Lu, Y.; Guo, Z.; Gu, J.; Gu, C. Corrosion Behaviour of a Quenched and Partitioned Medium Carbon Steel in 3.5 Wt.% NaCl Solution. *Corrosion Science* **2018**, *130*, 64–75. https://doi.org/10.1016/j.corsci.2017.10.027.
(15) Popova, A.; Sokolova, E.; Raicheva, S.; Christov, M. AC and DC Study of the Temperature Effect on Mild Steel Corrosion in Acid Media in the Presence of

Benzimidazole Derivatives. *Corrosion Science* **2003**, *45* (1), 33–58. https://doi.org/10.1016/S0010-938X(02)00072-0.
(16) Douadi, T.; Hamani, H.; Daoud, D.; Al-Noaimi, M.; Chafaa, S. Effect of Temperature and Hydrodynamic Conditions on Corrosion Inhibition of an Azomethine Compounds for Mild Steel in 1 M HCl Solution. *Journal of the Taiwan Institute of Chemical Engineers* **2017**, *71*, 388–404. https://doi.org/10.1016/j.jtice.2016.11.026.
(17) Ouici, H.; Tourabi, M.; Benali, O.; Selles, C.; Jama, C.; Zarrouk, A.; Bentiss, F. Adsorption and Corrosion Inhibition Properties of 5-Amino 1,3,4-Thiadiazole-2-Thiol on the Mild Steel in Hydrochloric Acid Medium: Thermodynamic, Surface and Electrochemical Studies. *Journal of Electroanalytical Chemistry* **2017**, *803*, 125–134. https://doi.org/10.1016/j.jelechem.2017.09.018.
(18) Kelly, R. G.; et al.et al. *Electrochemical Techniques in Corrosion Science and Engineering*; CRC Press, 2002.
(19) Brad, A.; Larry, F.; Ledddy, J.; Zoski, C. *Electrochemical Methods: Fundamentals and Applications*; New York, 1980; Vol. 2.
(20) Revie, R. W. *Corrosion and Corrosion Control:An Introduction to Corrosion Science and Engineering*; John Wiley & Sons, 2008.
(21) Hoar, T. P.; Jacob, W. R. Breakdown of Passivity of Stainless Steel by Halide Ions. *Nature* **1967**, *216* (5122), 1299–1301. https://doi.org/10.1038/2161299a0.
(22) Sato, N. A Theory for Breakdown of Anodic Oxide Films on Metals. *Electrochimica Acta* **1971**, *16* (10), 1683–1692. https://doi.org/10.1016/0013-4686(71)85079-X.
(23) Neši, S. A MULTIPHASE FLOW AND INTERNAL CORROSION PREDICTION MODEL FOR MILD STEEL PIPELINES. 35.
(24) Perez, N. *Electrochemistry and Corrosion Science*; Kluwer Academic Publishers: Boston, 2004; Vol. Vol. 412.
(25) Roberge, P. R. *Handbook of Corrosion Engineering*; McGraw-Hill handbooks; McGraw-Hill: New York, 2000.
(26) Fear, C.; Juarez-Robles, D.; Jeevarajan, J. A.; Mukherjee, P. P. Elucidating Copper Dissolution Phenomenon in Li-Ion Cells under Overdischarge Extremes. *J. Electrochem. Soc.* **2018**, *165* (9), A1639–A1647. https://doi.org/10.1149/2.0671809jes.
(27) Frankel, G. . Chapter 2 Fundamentals of Corrosion Kinetics. In *Active Protective Coatings: New-Generation Coatings for Metals*; Columbus, OH, USA, 2016.
(28) Pitting Corrosion https://www.nace.org/Pitting-Corrosion/ (accessed Dec 28, 2017).
(29) Galvele, J. R. Transport Processes and the Mechanism of Pitting of Metals. *J. Electrochem. Soc.* **1976**, *123* (4), 464–474. https://doi.org/10.1149/1.2132857.
(30) Chao, C. Y.; Lin, L. F.; Macdonald, D. D. A Point Defect Model for Anodic Passive Films I . Film Growth Kinetics. *J. Electrochem. Soc.* **1981**, *128* (6), 1187–1194. https://doi.org/10.1149/1.2127591.

(31) Transport Processes and the Mechanism of Pitting of Metals http://jes.ecsdl.org.proxy-um.researchport.umd.edu/content/123/4/464.short (accessed Jul 5, 2018).
(32) Dhaiveegan, P.; Elangovan, N.; Nishimura, T.; Rajendran, N. Weathering Steel in Industrial-Marine-Urban Environment: Field Study. *MATERIALS TRANSACTIONS* **2016**, *57* (2), 148–155. https://doi.org/10.2320/matertrans.M2015345.
(33) Bardal, E. *Corrosion and Protection*; Springer: London ; New York, 2004.
(34) Liu, W.; Zhou, Q.; Li, L.; Wu, Z.; Cao, F.; Gao, Z. Effect of Alloy Element on Corrosion Behavior of the Huge Crude Oil Storage Tank Steel in Seawater. *Journal of Alloys and Compounds* **2014**, *598*, 198–204. https://doi.org/10.1016/j.jallcom.2014.01.181.
(35) Javaherdashti, R. *Microbiologically Influenced Corrosion: An Engineering Insight*; Springer Science & Business Media, 2008.
(36) What is Corrosion Costing the pipeline industry? | Intelligent Pipeline Technologies http://www.ipltec.com/news/articles/what-is-corrosion-costing-the-pipeline-industry/ (accessed Dec 28, 2017).
(37) Ahammed, M.; Melchers, R. E. Reliability Estimation of Pressurised Pipelines Subject to Localised Corrosion Defects. *International Journal of Pressure Vessels and Piping* **1996**, *69* (3), 267–272. https://doi.org/10.1016/0308-0161(96)00009-9.
(38) Yan, M.; Sun, C.; Xu, J.; Dong, J.; Ke, W. Role of Fe Oxides in Corrosion of Pipeline Steel in a Red Clay Soil. *Corrosion Science* **2014**, *80*, 309–317. https://doi.org/10.1016/j.corsci.2013.11.037.
(39) Ahmad, S. Reinforcement Corrosion in Concrete Structures, Its Monitoring and Service Life Prediction––a Review. *Cement and Concrete Composites* **2003**, *25* (4–5), 459–471. https://doi.org/10.1016/S0958-9465(02)00086-0.
(40) Tawancy, H. M.; Al-Hadhrami, L. M.; Al-Yousef, F. K. Analysis of Corroded Elbow Section of Carbon Steel Piping System of an Oil–Gas Separator Vessel. *Case Studies in Engineering Failure Analysis* **2013**, *1* (1), 6–14. https://doi.org/10.1016/j.csefa.2012.11.001.
(41) Agbezuge, L. Why Carbon Steel is Essential in the Oil and Gas Industry? http://info.industrialskyworks.com/blog/why-carbon-steel-is-essential-in-the-oil-and-gas-industry (accessed Jul 4, 2018).
(42) Sugimota, K.; Seto, M.; Tanaka, S.; Hara, N. Corrosion Resistanceof Artificial Passivation Films of Fe O -Cr O -NiO Formed by Metalorganic Chemical Vapor Deposition. *J. Electrochem. Soc.* **1993**, *140* (6), 7.
(43) Ilman, M. N.; Kusmono. Analysis of Internal Corrosion in Subsea Oil Pipeline. *Case Studies in Engineering Failure Analysis* **2014**, *2* (1), 1–8. https://doi.org/10.1016/j.csefa.2013.12.003.
(44) Azevedo, C. R. F. Failure Analysis of a Crude Oil Pipeline. *Engineering Failure Analysis* **2007**, *14* (6), 978–994. https://doi.org/10.1016/j.engfailanal.2006.12.001.
(45) Lotz, U.; Van Bodegom, L.; Ouwehand, C. The Effect of Type of Oil or Gas Condensate on Carbonic Acid Corrosion. *Corrosion* **1991**, *47* (8), 635–645.

(46) Pessu, F.; Barker, R.; Neville, A. Understanding Pitting Corrosion Behaviour of X-65 Carbon Steel in CO2 Saturated Environments: The Temperature Effect. *Corrosion* **2015**. https://doi.org/10.5006/1338.
(47) Nešić, S. Key Issues Related to Modelling of Internal Corrosion of Oil and Gas Pipelines – A Review. *Corrosion Science* **2007**, *49* (12), 4308–4338. https://doi.org/10.1016/j.corsci.2007.06.006.
(48) Kermani, M. B.; Morshed, A. Carbon Dioxide Corrosion in Oil and Gas Production—A Compendium. *CORROSION* **2003**, *59* (8), 659–683. https://doi.org/10.5006/1.3277596.
(49) Waard, C. D.; Milliams, D. . Carbonic Acid Corrosion of Steel. *CORROSION* No. 1975;31(5):177-181.
(50) Wang, S.; George, K.; Nesic, S. HIGH PRESSURE CO2 CORROSION ELECTROCHEMISTRY AND THE EFFECT OF ACETIC ACID. 17.
(51) External Corrosion https://primis.phmsa.dot.gov/comm/FactSheets/FSExternalCorrosion.htm (accessed Oct 15, 2018).
(52) *Report 2013-B: Pipeline Performance in Alberta 1990-2012*; 2013; p 104.
(53) Rostami, A.; Arabloo, M.; Kamari, A.; Mohammadi, A. H. Modeling of CO 2 Solubility in Crude Oil during Carbon Dioxide Enhanced Oil Recovery Using Gene Expression Programming. *Fuel* **2017**, *210*, 768–782. https://doi.org/10.1016/j.fuel.2017.08.110.
(54) Combined Effect of CO2, H2S and Acetic Acid on Bottom of the Line Corrosion. 25.
(55) Nyborg, R. Overview of CO2 Corrosion Models for Wells and Pipelines. *CORROSION Nace International* **2002**.
(56) De Waard, C.; Lotz, U.; Milliams, D. . Predictive Model for CO2 Corrosion Engineering in Wet Natural Gas Pipelines. *CORROSION 47.12* (1991), 976–985.
(57) Nesic, S.; Postlethwaite, J.; Olsen, S. An Electrochemical Model for Prediction of Corrosion of Mild Steel in Aqueous Carbon Dioxide Solutions. *CORROSION* **1996**, *52* (4), 280–294. https://doi.org/10.5006/1.3293640.
(58) Vosikovsky, O.; Rivard, A. The Effect of Hydrogen Sulfide in Crude Oil on Fatigue Crack Growth in a Pipe Line Steel. *Corrosion* **1982**, *38* (1), 19–22.
(59) HANSEN, H. C. B.; BORGGAARD, O. K.; SL, J. Evaluation of the Free Energy of Formation of Fe(H)-Fe(II1) Hydroxide-Su~phate (Green Rust) and Its Reduction of Nitrite. 10.
(60) AlAbbas, F. M.; Williamson, C.; Bhola, S. M.; Spear, J. R.; Olson, D. L.; Mishra, B.; Kakpovbia, A. E. Microbial Corrosion in Linepipe Steel Under the Influence of a Sulfate-Reducing Consortium Isolated from an Oil Field. *Journal of Materials Engineering and Performance* **2013**, *22* (11), 3517–3529. https://doi.org/10.1007/s11665-013-0627-7.
(61) Ma, H.; Cheng, X.; Li, G.; Chen, S.; Quan, Z.; Zhao, S.; Niu, L. The In¯uence of Hydrogen Sul®de on Corrosion of Iron under Di©erent Conditions. *Corrosion Science* **2000**, 15.
(62) Al-Jaroudi, S. S.; Ul-Hamid, A.; Al-Gahtani, M. M. Failure of Crude Oil Pipeline Due to Microbiologically Induced Corrosion. *Corrosion Engineering, Science*

and Technology **2011**, *46* (4), 568–579. https://doi.org/10.1179/147842210X12695149033819.
(63) Rabus, R.; et al. Degradative Capacities and 16S RRNA-Targeted Whole-Cell Hybridization of Sulfate-Reducing Bacteria in an Anaerobic Enrichment Culture Utilizing Alkylbenzenes from Crude Oil. | Applied and Environmental Microbiology. *Applied and Environmental Microbiology 62–10* (1996), 3605–3613.
(64) Neria-González, I.; Wang, E. T.; Ramírez, F.; Romero, J. M.; Hernández-Rodríguez, C. Characterization of Bacterial Community Associated to Biofilms of Corroded Oil Pipelines from the Southeast of Mexico. *Anaerobe* **2006**, *12* (3), 122–133. https://doi.org/10.1016/j.anaerobe.2006.02.001.
(65) Skovhus, T. L.; Eckert, R. B.; Rodrigues, E. Management and Control of Microbiologically Influenced Corrosion (MIC) in the Oil and Gas Industry—Overview and a North Sea Case Study. *Journal of Biotechnology* **2017**, *256*, 31–45. https://doi.org/10.1016/j.jbiotec.2017.07.003.
(66) Efird, K. D.; Jasinski, R. J. Effect of the Crude Oil on Corrosion of Stee in Crude Oil/ Brine Production. *Corrosion* **1989**, *45* (2), 160–165.
(67) Ayello, F.; Robbins, W.; Richter, S.; Nesic, S. Crude Oil Chemistry Effects on Inhibition of Corrosion and Phase Wetting. *CORROSION/11, paper* **2011**, No. 11060.
(68) Veil, J.; Puder, M. .; Elcock, D.; Redwiek Jr, R. J. *A White Paper Describing Produced Water from Production of Crude Oil, Natural Gas and Coal Bed Methane*; 112631; Argonne National lab: IL (US), 2004.
(69) Schumacher, U.; Cornell, R. The Iron Oxides: Structure, Properties, Reactions, Occurrences and Uses http://www.wiley.com/WileyCDA/WileyTitle/productCd-3527606440.html (accessed Dec 2, 2017).
(70) de la Fuente, D.; Alcántara, J.; Chico, B.; Díaz, I.; Jiménez, J. A.; Morcillo, M. Characterisation of Rust Surfaces Formed on Mild Steel Exposed to Marine Atmospheres Using XRD and SEM/Micro-Raman Techniques. *Corrosion Science* **2016**, *110*, 253–264. https://doi.org/10.1016/j.corsci.2016.04.034.
(71) Cano, H.; Neff, D.; Morcillo, M.; Dillmann, P.; Diaz, I.; de la Fuente, D. Characterization of Corrosion Products Formed on Ni 2.4 Wt%–Cu 0.5 Wt%–Cr 0.5 Wt% Weathering Steel Exposed in Marine Atmospheres. *Corrosion Science* **2014**, *87*, 438–451. https://doi.org/10.1016/j.corsci.2014.07.011.
(72) Cudennec, Y.; Lecerf, A. Topotactic Transformations of Goethite and Lepidocrocite into Hematite and Maghemite. *Solid State Sciences* **2005**, *7* (5), 520–529. https://doi.org/10.1016/j.solidstatesciences.2005.02.002.
(73) Misawa, T.; Hashimoto, K.; Shimodaira, S. The Mechanism of Formation of Iron Oxide and Oxyhydroxides in Aqueous Solutions at Room Temperature. *Corrosion Science* **1974**, *14* (2), 131–149. https://doi.org/10.1016/S0010-938X(74)80051-X.
(74) Schwertmann, U. The Formation of Green Rust and Its Transformation to Lepidocrocite. *Clay Minerals* **1994**, *29* (1), 87–92. https://doi.org/10.1180/claymin.1994.029.1.10.

(75) van der, G.; Antonio, A. Chemical and Physical Properties of Iron (III)-Oxide Hydrate. *Centrex* **1968**.
(76) Dzombak, D. .; François, M. *Surface Complexation Modeling: Hydrous Ferric Oxide*; John Wiley & Sons, 1990.
(77) Schwertmann, U.; Fischer, W. R. Natural "Amorphous" Ferric Hydroxide. *Geoderma* **1973**, *10* (3), 237–247. https://doi.org/10.1016/0016-7061(73)90066-9.
(78) Tronc, E.; Belleville, P.; Jolivet, J. P.; Livage, J. Transformation of Ferric Hydroxide into Spinel by Iron(II) Adsorption. *Langmuir* **1992**, *8* (1), 313–319. https://doi.org/10.1021/la00037a057.
(79) Musić, S.; Gotić, M.; Popović, S. X-Ray Diffraction and Fourier Transform-Infrared Analysis of the Rust Formed by Corrosion of Steel in Aqueous Solutions. *Journal of Materials Science* **1993**, *28* (21), 5744–5752. https://doi.org/10.1007/BF00365176.
(80) Kamimura, T.; Hara, S.; Miyuki, H.; Yamashita, M.; Uchida, H. Composition and Protective Ability of Rust Layer Formed on Weathering Steel Exposed to Various Environments. *Corrosion Science* **2006**, *48* (9), 2799–2812. https://doi.org/10.1016/j.corsci.2005.10.004.
(81) Stratmann, M.; Bohnenkamp, K.; Engell, H. . An Electrochemical Study of Phase-Transitions in Rust Layers. *Corrosion Science* **1983**, *23.9*, 969–985.
(82) Misawa, T.; et al. The Mechanism of Atmospheric Rusting and the Protective Amorphous Rust on Low Alloy Steel. *Corrosion Science* **1974**, No. 14.4, 279–289.
(83) Paul, S.; Pattanayak, A.; Guchhait, S. K. Corrosion Behavior of Carbon Steel in Synthetically Produced Oil Field Seawater. *International Journal of Metals* **2014**, *2014*, 1–11. https://doi.org/10.1155/2014/628505.
(84) Wu, S. L.; Cui, Z. D.; He, F.; Bai, Z. Q.; Zhu, S. L.; Yang, X. J. Characterization of the Surface Film Formed from Carbon Dioxide Corrosion on N80 Steel. *Materials Letters* **2004**, *58* (6), 1076–1081. https://doi.org/10.1016/j.matlet.2003.08.020.
(85) Sridhar, N.; Dunn, D. S.; Anderko, A. M.; Lencka, M. M.; Schutt, H. U. Effects of Water and Gas Compositions on the Internal Corrosion of Gas Pipelines—Modeling and Experimental Studies. *CORROSION* **2001**, *57* (3), 221–235. https://doi.org/10.5006/1.3290347.
(86) Riggs, O.; Hurd, R. Temperature Coefficient of Corrosion Inhibition. *CORROSION* **1967**, *23* (8), 252–260. https://doi.org/10.5006/0010-9312-23.8.252.
(87) Navrotsky, A.; Lena, M. Size-Driven Structural and Thermodynamic Complexity in Iron Oxides. *Science* **2008**, *319* (5870), 1635–1638. https://doi.org/10.1126/science.1141134.
(88) Das, S.; Hendry, M. J.; Essilfie-Dughan, J. Transformation of Two-Line Ferrihydrite to Goethite and Hematite as a Function of PH and Temperature. *Environmental Science & Technology* **2011**, *45* (1), 268–275. https://doi.org/10.1021/es101903y.

(89) Schwertmann, U.; Friedl, J.; Stanjek, H. From Fe(III) Ions to Ferrihydrite and Then to Hematite. *Journal of Colloid and Interface Science* **1999**, *209* (1), 215–223. https://doi.org/10.1006/jcis.1998.5899.
(90) Wang, J. H.; Wei, F. I.; Chang, Y. S.; Shih, H. C. The Corrosion Mechanisms of Carbon Steel and Weathering Steel in SO2 Polluted Atmospheres. *Materials Chemistry and Physics* **1997**, *47* (1), 1–8.
(91) Gerhardus H., K.; Broners, M.; Thompson, N. Corrosion Costs and Preventive Strategies in the Uinted States. *NACE International* No. FHWA-RD-01-156.
(92) Bennett, L. H.; Kruger, J.; Parker, R. L.; Passaglia, E.; Reimann, C.; Ruff, A. W.; Yakowitz, H.; Berman, E. B. *Economic Effects of Metallic Corrosion in the United States Part I*; NBS SP 511-1; National Bureau of Standards: Gaithersburg, MD, 1978. https://doi.org/10.6028/NBS.SP.511-1.
(93) NACE. NACE study estimates global corrosion cost at $2.5 trillion annually https://inspectioneering.com/news/2016-03-08/5202/nace-study-estimates-global-cost-of-corrosion-at-25-trillion-ann (accessed Jun 6, 2018).
(94) Corrosion Control In Oil And Gas Pipelines | Pipeline & Gas Journal https://pgjonline.com/magazine/2010/march-2010-vol-237-no-3/features/corrosion-control-in-oil-and-gas-pipelines (accessed Jul 2, 2018).
(95) ASTM G1 Standard Practice for Preparing, Cleaning, and Evaluating Corrosion Test Specimens.
(96) Yuan, X.-Z.; Song, C.; Wang, H.; Zhang, J. *Electrochemical Impedance Spectroscopy in PEM Fuel Cells*; Springer London: London, 2010. https://doi.org/10.1007/978-1-84882-846-9.
(97) Jüttner, K. Electrochemical Impedance Spectroscopy (EIS) of Corrosion Processes on Inhomogeneous Surfaces. *Electrochimica Acta* **1990**, *35* (10), 1501–1508.
(98) Zou, Y.; Wang, J.; Zheng, Y. Y. Electrochemical Techniques for Determining Corrosion Rate of Rusted Steel in Seawater. *Corrosion Science* **2011**, *53* (1), 208–216. https://doi.org/10.1016/j.corsci.2010.09.011.
(99) Schwertmann, U.; Cornell, R. *Iron Oxide in the Laboratory: Preparation and Characterization*, 2nd Edition.; John Wiley & Sons, 2008.
(100) Melchers, R. E. Effect of Temperature on the Marine Immersion Corrosion of Carbon Steels. *Corrosion* **2002**, *58* (9), 768–782.
(101) de la Fuente, D.; Díaz, I.; Simancas, J.; Chico, B.; Morcillo, M. Long-Term Atmospheric Corrosion of Mild Steel. *Corrosion Science* **2011**, *53* (2), 604–617. https://doi.org/10.1016/j.corsci.2010.10.007.
(102) Hansel, C. M.; Benner, S. G.; Neiss, J.; Dohnalkova, A.; Kukkadapu, R. K.; Fendorf, S. Secondary Mineralization Pathways Induced by Dissimilatory Iron Reduction of Ferrihydrite under Advective Flow. *Geochimica et Cosmochimica Acta* **2003**, *67* (16), 2977–2992. https://doi.org/10.1016/S0016-7037(03)00276-X.
(103) Antunes, R. A.; Costa, I.; Faria, D. L. A. de. Characterization of Corrosion Products Formed on Steels in the First Months of Atmospheric Exposure. *Materials research* **2003**, *6* (3), 403–408.

(104) Dong, H.; Fredrickson, J. K.; Kennedy, D. W.; Zachara, J. M.; Kukkadapu, R. K.; Onstott, T. C. Mineral Transformation Associated with the Microbial Reduction of Magnetite. **2000**, 20.
(105) Dünnwald, J.; Otto, A. An Investigation of Phase Transitions in Rust Layers Using Raman Spectroscopy. *Corrosion Science* **1989**, *29* (9), 1167–1176. https://doi.org/10.1016/0010-938X(89)90052-8.
(106) de Faria, D. L. A.; Venâncio Silva, S.; de Oliveira, M. T. Raman Microspectroscopy of Some Iron Oxides and Oxyhydroxides. *J. Raman Spectrosc.* **1997**, *28* (11), 873–878. https://doi.org/10.1002/(SICI)1097-4555(199711)28:11<873::AID-JRS177>3.0.CO;2-B.
(107) Odziemkowski, M. S.; Schuhmacher, T. T.; Gillham, R. W.; Reardon, E. J. Mechanism of Oxide Film Formation on Iron in Simulating Groundwater Solutions: Raman Spectroscopic Studies. *Corrosion Science* **1998**, *40* (2–3), 371–389. https://doi.org/10.1016/S0010-938X(97)00141-8.
(108) Ohtsuka, T.; Kubo, K.; Sato, N. Raman Spectroscopy of Thin Corrosion Films on Iron at 100 to 150 C in Air. *CORROSION* **1986**, *42* (8), 476–481. https://doi.org/10.5006/1.3583054.
(109) Thibeau, R. J.; Brown, C. W.; Heidersbach, R. H. Raman Spectra of Possible Corrosion Products of Iron. *Applied Spectroscopy* **1978**, *32* (6), 532–535. https://doi.org/10.1366/000370278774330739.
(110) Oh, S. J.; Cook, D. C.; Townsend, H. E. Characterization of Iron Oxides Commonly Formed as Corrosion Products on Steel. *Hyperfine Interactions* **1998**, *112* (1), 59–66. https://doi.org/10.1023/A:1011076308501.
(111) Hanesch, M. Raman Spectroscopy of Iron Oxides and (Oxy)Hydroxides at Low Laser Power and Possible Applications in Environmental Magnetic Studies. *Geophysical Journal International* **2009**, *177* (3), 941–948. https://doi.org/10.1111/j.1365-246X.2009.04122.x.
(112) Thierry, D.; Persson, D.; Leygraf, C.; Boucherit, N.; Hugot-le Goff, A. Raman Spectroscopy and XPS Investigations of Anodic Corrosion Films Formed on FeMo Alloys in Alkaline Solutions. *Corrosion Science* **1991**, *32* (3), 273–284. https://doi.org/10.1016/0010-938X(91)90073-X.
(113) Faria, D. L. A. de; Silva, S. V.; Oliveira, M. T. de. Raman microspectroscopy of some iron oxides and oxyhydroxides. *Journal of Raman Spectroscopy* **1997**, *28* (11), 873–878. https://doi.org/10.1002/(SICI)1097-4555(199711)28:11<873::AID-JRS177>3.0.CO;2-B.
(114) Li, P.; Lin, J. Y.; Tan, K. L.; Lee, J. Y. Electrochemical Impedance and X-Ray Photoelectron Spectroscopic Studies of the Inhibition of Mild Steel Corrosion in Acids by Cyclohexylamine. *Electrochimica Acta* **1997**, *42* (4), 605–615. https://doi.org/10.1016/S0013-4686(96)00205-8.
(115) Lopez, D. A.; Schreiner, W. H.; de Sanchez, S. R.; Simison, S. N. The Influence of Carbon Steel Microstructure on Corrosion Layers An XPS and SEM Characterization. *Applied Surface Science* **2003**, 17.
(116) Kármán, F. H.; Felhösi, I.; Kálman, E.; Cserny, I.; Kövér, L. The Role of Oxide Layer Formation during Corrosion Inhibition of Mild Steel in Neutral Aqueous Media. *Electrochimica Acta* **1998**, *43* (1–2), 69–75. https://doi.org/10.1016/S0013-4686(97)00236-3.

(117) Temesghen, W.; Sherwood, P. Analytical Utility of Valence Band X-Ray Photoelectron Spectroscopy of Iron and Its Oxides, with Spectral Interpretation by Cluster and Band Structure Calculations. *Analytical and Bioanalytical Chemistry* **2002**, *373* (7), 601–608. https://doi.org/10.1007/s00216-002-1362-3.
(118) Borch, T.; Camper, A. K.; Biederman, J. A.; Butterfield, P. W.; Gerlach, R.; Amonette, J. E. Evaluation of Characterization Techniques for Iron Pipe Corrosion Products and Iron Oxide Thin Films. *Journal of Environmental Engineering* **2008**, *134* (10), 835–844. https://doi.org/10.1061/(ASCE)0733-9372(2008)134:10(835).
(119) Heuer, J. K.; Stubbins, J. F. An XPS Characterization of FeCO3 Films from CO2 Corrosion. *Corrosion Science* **1999**, *41* (7), 1231–1243. https://doi.org/10.1016/S0010-938X(98)00180-2.
(120) Sumoondur, A.; Shaw, S.; Ahmed, I.; Benning, L. G. Green Rust as a Precursor for Magnetite: An <I>in Situ</I> Synchrotron Based Study. *Mineralogical Magazine* **2008**, *72* (1), 201–204. https://doi.org/10.1180/minmag.2008.072.1.201.
(121) TROLARD, F. Identification of a Green Rust Mineral in a Reductomorphic Soil by M6ssbauer and Raman Spectroscopies. 5.
(122) Christiansen, B. C.; Balic-Zunic, T.; Dideriksen, K.; Stipp, S. L. S. Identification of Green Rust in Groundwater. *Environ. Sci. Technol.* **2009**, *43* (10), 3436–3441. https://doi.org/10.1021/es8011047.
(123) Zegeye, A.; Ona-Nguema, G.; Carteret, C.; Huguet, L.; Abdelmoula, M.; Jorand, F. Formation of Hydroxysulphate Green Rust 2 as a Single Iron(II-III) Mineral in Microbial Culture. *Geomicrobiology Journal* **2005**, *22* (7–8), 389–399. https://doi.org/10.1080/01490450500248960.
(124) Mansfeld, F. Fundamental Aspects of the Polarization Resistance Technique—the Early Days. *Journal of Solid State Electrochemistry* **2009**, *13* (4), 515–520. https://doi.org/10.1007/s10008-008-0652-x.
(125) Butler, G.; Stroud, E. . The Influence of Movement and Temperature on the Corrosion of Mild Steel. II. High Purity Water. *Journal of Applied Chemistry* **1965**, *15.7*, 325–338.
(126) Sharqawy, M. H.; Lienhard, J. H.; Zubair, S. M. Thermophysical Properties of Seawater: A Review of Existing Correlations and Data. *Desalination and Water Treatment* **2010**, *16* (1–3), 354–380. https://doi.org/10.5004/dwt.2010.1079.
(127) Poulson, B. Electrochemical Measurements in Flowing Solutions. *Corrosion Science* **1983**, *23.4*, 391–430.
(128) Nakayama, Y.; Boucher, R. F. *Introduction to Fluid Mechanics*; Arnold [u.a.]: London, 1999.
(129) Shi, L.; Wang, C.; Zou, C. Corrosion Failure Analysis of L485 Natural Gas Pipeline in CO2 Environment. *Engineering Failure Analysis* **2014**, *36*, 372–378. https://doi.org/10.1016/j.engfailanal.2013.11.009.
(130) Butler, G.; Ison, H. C. K. The Influence of Movement and Temperature on the Corrosion of Mild Steel. I. Water Circulation Apparatus and Tests in

Teddington Mains Water. *Journal of Applied Chemistry* **1960**, *10* (2), 80–93. https://doi.org/10.1002/jctb.5010100206.
(131) Kim, Y.-S.; Kim, J.-G. Corrosion Behavior of Pipeline Carbon Steel under Different Iron Oxide Deposits in the District Heating System. *Metals* **2017**, *7* (5), 182. https://doi.org/10.3390/met7050182.
(132) Antony, H.; Perrin, S.; Dillmann, P.; Legrand, L.; Chaussé, A. Electrochemical Study of Indoor Atmospheric Corrosion Layers Formed on Ancient Iron Artefacts. *Electrochimica Acta* **2007**, *52* (27), 7754–7759. https://doi.org/10.1016/j.electacta.2007.04.029.
(133) Zhao, W.; Zou, Y.; Matsuda, K.; Zou, Z. Characterization of the Effect of Hydrogen Sulfide on the Corrosion of X80 Pipeline Steel in Saline Solution. *Corrosion Science* **2016**, *102*, 455–468. https://doi.org/10.1016/j.corsci.2015.10.038.
(134) Yadav, D. K.; Maiti, B.; Quraishi, M. A. Electrochemical and Quantum Chemical Studies of 3,4-Dihydropyrimidin-2(1H)-Ones as Corrosion Inhibitors for Mild Steel in Hydrochloric Acid Solution. *Corrosion Science* **2010**, *52* (11), 3586–3598. https://doi.org/10.1016/j.corsci.2010.06.030.
(135) Wang, Z.; Liu, J.; Wu, L.; Han, R.; Sun, Y. Study of the Corrosion Behavior of Weathering Steels in Atmospheric Environments. *Corrosion Science* **2013**, *67*, 1–10. https://doi.org/10.1016/j.corsci.2012.09.020.
(136) Doliente, J. E.; Kim, Y.; Nam, H.; Choi, Y. Mill Scale–Derived Magnetite Particles: Effective Adsorbent for the Removal of Phosphate in Aqueous Solutions. *Journal of Environmental Engineering* **2017**, *143* (12), 04017076. https://doi.org/10.1061/(ASCE)EE.1943-7870.0001278.
(137) Gotić, M.; Musić, S. Mössbauer, FT-IR and FE SEM Investigation of Iron Oxides Precipitated from FeSO4 Solutions. *Journal of Molecular Structure* **2007**, *834–836*, 445–453. https://doi.org/10.1016/j.molstruc.2006.10.059.
(138) Raman, A.; Kuban, B.; Razvan., R. The Application of Infrared Spectroscopy to the Study of Atmospheric Rust Systems—I. Standard Spectra and Illustrative Applications to Identify Rust Phases in Natural Atmospheric Corrosion Products. *Corrosion Science* **1991**, *32.12*, 1295-1306.
(139) Weckler, B.; Lutz, H. D.; Siegen, U. Lattice Vibration Spectra. Part XCV. Infrared Spectroscopic Studies on the Iron Oxide Hydroxides Goethite (a), Akagankite (P>, Lepidocrocite ($, and Feroxyhite (6). 14.
(140) Misawa, T.; Kyuno, T.; Suëtaka, W.; Shimodaira, S. The Mechanism of Atmospheric Rusting and the Effect of Cu and P on the Rust Formation of Low Alloy Steels. *Corrosion Science* **1971**, *11* (1), 35–48. https://doi.org/10.1016/S0010-938X(71)80072-0.
(141) Tronc, E.; Belleville, P.; Jolivet, J. P.; Livage, J. Transformation of Ferric Hydroxide into Spinel by Iron(II) Adsorption. *Langmuir* **1992**, *8* (1), 313–319. https://doi.org/10.1021/la00037a057.
(142) Cornell, R.; Rudolf, G.; Walter, S. Review of the Hydrolysis of Iron (III) and the Crystallization of Amorphous Iron (III) Hydroxide Hydrate. *Journal of Chemical Technology & Biotechnology* **1989**, *46.2*, 115–134.
(143) Pedersen, H. D.; Postma, D.; Jakobsen, R.; Larsen, O. Fast Transformation of Iron Oxyhydroxides by the Catalytic Action of Aqueous Fe(II). *Geochimica et*

Cosmochimica Acta **2005**, *69* (16), 3967–3977. https://doi.org/10.1016/j.gca.2005.03.016.
(144) Rose, A. L.; Waite, T. D. Kinetics of Hydrolysis and Precipitation of Ferric Iron in Seawater. *Environmental Science & Technology* **2003**, *37* (17), 3897–3903. https://doi.org/10.1021/es034102b.
(145) Schwertmann, U.; Murad, E. Effect of PH on the Formation of Goethite and Hematite from Ferrihydrite. *Clays and Clay Minerals* **1983**, *31.4*, 277–284.
(146) Schwertmann, U.; Murad, E. Effect of PH on the Formation of Goethite and Hematite from Ferrihydrite. *Clays and Clay Minerals* **1983**, *31* (4), 277–284. https://doi.org/10.1346/CCMN.1983.0310405.
(147) Iwasaki, T.; Sato, N.; Kosaka, K.; Watano, S.; Yanagida, T.; Kawai, T. Direct Transformation from Goethite to Magnetite Nanoparticles by Mechanochemical Reduction. *Journal of Alloys and Compounds* **2011**, *509* (4), L34–L37. https://doi.org/10.1016/j.jallcom.2010.10.029.
(148) Duan, J.; Wu, S.; Zhang, X.; Huang, G.; Du, M.; Hou, B. Corrosion of Carbon Steel Influenced by Anaerobic Biofilm in Natural Seawater. *Electrochimica Acta* **2008**, *54* (1), 22–28. https://doi.org/10.1016/j.electacta.2008.04.085.
(149) Ragil, K.; Bonn, D.; Broseta, D.; Indekeu, J.; Kalaydjian, F.; Meunier, J. The Wetting Behavior of Alkanes on Water. *Journal of Petroleum Science and Engineering* **1998**, *20* (3–4), 177–183. https://doi.org/10.1016/S0920-4105(98)00018-7.
(150) Kowalewski, E.; Holt, T.; Torsaeter, O. Wettability Alterations Due to an Oil Soluble Additive. *Journal of Petroleum Science and Engineering* **2002**, *33* (1–3), 19–28. https://doi.org/10.1016/S0920-4105(01)00172-3.
(151) Turnbull, A.; Slavcheva, E.; Shone, B. Factors Controlling Naphthenic Acid Corrosion. *Corrosion; Houston* **1998**, *54* (11), 922.
(152) Papavinasam, S.; Doiron, A.; Revie, R. W. Model to Predict Internal Pitting Corrosion of Oil and Gas Pipelines. *Corrosion; Houston* **2010**, *66* (3), E1–E11.